Electronic transport at zero and high pressures

in mixed-valence perovskite manganites $A_{1-x}B_xMnO_3$ and

in alkali-doped polymerized C_{60}

by

Kasra Khazeni

B.A. (University of California at Berkeley) 1991
M.A. (University of California at Berkeley) 1993

A dissertation submitted in partial satisfaction of the requirements for the degree of

Doctor of Philosophy
in
Physics

in the
GRADUATE DIVISION
of the
UNIVERSITY of CALIFORNIA at BERKELEY

Committee in charge:

Professor Alex K. Zettl
Professor Marvin L. Cohen
Professor Raymond Jeanloz

Spring 1997

The dissertation of Kasra Khazeni is approved:

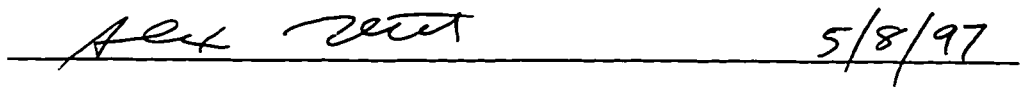

Chair Date

Date

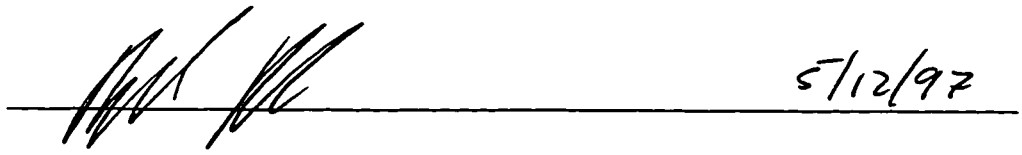

Date

University of California, Berkeley

Spring 1997

Electronic transport at zero and high pressures

in mixed-valence perovskite manganites $A_{1-x}B_xMnO_3$ and

in alkali-doped polymerized C_{60}

Kasra Khazeni

To Farida with love

and to

Soody, Amir

Rasta, and Anoush

Table of contents

List of figures

Acknowledgments

First I want to thank my advisor Professor Alex K. Zettl for giving me the opportunity to become a "Zett". His willingness to explore new frontiers and test new ideas makes his lab an ideal place to do physics, and his friendly attitude and sense of humor make the lab a fun place to work. Alex's own Ph.D thesis, which by the way is almost five hundred pages long, took him only two years. This still amazes me considering the fact that publication of only one paper requires weeks or even months of painstaking research and data acquisition. Alex, you are a great scientist and advisor.

I am very thankful to Professor Marvin L.Cohen for his guidance to new experiments and the remarkable physical intuition he contributed to interpreting our results. I want to thank Professor Raymond Jeanloz for teaching me high-pressure techniques. Raymond is the master of all sciences: physics, chemistry, geology, biology and evolution, just to name the ones I know about. He would always welcome my visits to his office pleasantly. I thank Professor Peter Yu for allowing me to use his diamond anvil pressure cell.

My all-time ally has been Professor Sumner P. Davis. Sumner and I go back about eight years ago to when I had just come to U.C. Berkeley. His fantastic teaching style in 111 lab has made him one of my favorite professors, and his great personality a very dear friend. Professor Dan Rokhsar has been an inspiration to me partly because he is half Persian and mostly because he is so smart. The first day he started his job here as a professor, someone sent him to Donna Sakima

thinking that he was an undergrad.

Now the "Zett"s. Miku is a real genius. He is one of those people who listens to your most awkward questions very carefully (although he might not look like he is) and, almost instantly, answers with unparalleled precision. Many times I have snuck a peek to see if he is trying to hide, behind that long hair of his, the CPU chip's gold pins sticking out of his skull, and, to my surprise, found nothing; it really is his own brain. No wonder Cynthia, his fiance, calls him the en-Michael-opedea. Mike, you have taught me a lot of tricks in the lab, and a great deal of non-physics stuff.

Jim Hone can do in one day what I do in ten years. Sometimes I think Werner Heisenberg came up with his uncertainty principle by watching Jim work: you can never know Jim's location and his socks dislocation simultaneously. I never forget the day we found his shoes on top of the fluorescent light on the ceiling. Jim, you are a very fun guy to be around.

Everyone knows Nasreen G. Chopra from her laughter, which overwhelms the decibel scale. She was barely seen in the lab, maybe because she worked at LBL. Yet she managed to write some fifteen papers and her thesis in two days (this is only slightly exaggerated). Nasreen, your cheerfulness made everyone in the lab happy. Phil Collins (*not* the former lead singer of the group Genesis) is remarkably patient. His project's fifth birthday is around the corner and he is still at it. Of course the project is extremely complicated and involved, but his enthusiasm for it hasn't diminished a bit. Good job Phil. To Charles Piskoti I only have one thing to say: nice shoes Charlie.

Li Lu is a living high-temperature (37°C to be exact) STM. He can attach eight wires and measure the Hall effect on a sample smaller than a neutrino! Don't ask me how. If I knew, I'd be Li Lu. If it weren't for Nancy Jia's hyper-velocity R vs. T data acquisition, I would probably not have graduated by now (at least that's what Farida thinks). Thanks Nancy.

Mikest is what I call Michael C. Martin. Besides being the largest human alive (hence Mikest), he is very helpful and kind. His web page still needs my voice for completion, but I hope he makes a lot of money with it before he asks me for my voice, so I can charge him for it. After I leave, Keith Bradley has promised to carry the torch of hi-pressure experiments in this lab. He is a genteel, a-bit-too-proper-for-this-lab, young man. Keith, if not the next Nobel prize recipient, at least you are staying with one. Jian (pronounced GN) is the Zettl lab's latest post-doc. Jian, I don't know how long you are going to be here, but I hope you would always enjoy the taste of that Chinese restaurant food you advertise about every-day. Vincent H. Crespi is the dude himself. Every time I went up to his office to talk to him, he was working on five different papers simultaneously. Professor Crespi, you are, besides a paper factory, a great theorist and a good teacher.

I have many people to thank outside of the Zettl lab. Anne Takizawa's help in all administrative chores, combined with her sweet personality, was a blessing. Armando Baeza is a marvelous machinist. The low-temperature probe he made for me is a work of art. Richard Mallozzi is unbelievable. His intelligence, manners, sense of humor, and most of all his "peace-with-himself" are what I have always admired about him. Rich, you already possess all of the qual-

ities that make a good friend, a good scientist, and a good human being. You will always be my role model. Leon Hsu never let me down with his vast knowledge of high-pressure experiments. He is always willing to help no matter how busy he is. Leon, stay that way and stay away from violence! John Rodriguez showed me how to be neat and organized. The table of contents he wrote for Professor Commins' quantum physics notes still helps me today.

Sugiharto Winoto, whose first name changed to Lukman after he came back from Harvard, is becoming a pool master (and I thought he was becoming a physicist). Lukman, you are truly a good friend. Finish up. Gene Dansker is a high-T_c SQUID wiz. In the past five years, Gene and I kept complaining about how unemployable we would be after graduation every time we saw each other in the hallways of LeConte. Little did I know that he is faking it! He was offered a top-notch job some six months before his graduation, and he accepted. Gene, you're the MAN. Tom Lee is incredible. He would always be at work: days, nights, and weekends. Tom, your dedication to work is admirable. Warren Holmes is always ready to learn new words in other languages. He knows two words in Farsi which I don't like to mention here. Warren, what are they doing at the toll plaza?

I would like to acknowledge some of the greatest Persian minds in the history of science, who tend to be ignored by most authors. Omar Khayyam for his pioneering work in astronomy and mathematics, Kharazmi (Khuwarizmi) for his invention of algebra, Zakariya Razi for his pioneering work in chemistry which led to discovery of alcohol, Abou Ali Sina (Avicenna) for his pioneering work in

the fields of medicine and surgery. Humanity will forever be indebted to these people.

Finally I would like to thank my wife Farida for all her support and encouragement. Her unique sweet personality makes my life an enjoyable experience. I thank my father for always encouraging me to think scientifically, and I thank my mother a billion times for her inconceivable patience, of which I have only inherited a little. I also want to thank my sister and my brother for believing in me.

Publications

1. Y.X. Jia, Li Lu, K. Khazeni, C.S. Lee, D. Yen, and A. Zettl, "Pr-Doping of High-Magnetoresistance Perovskite $(Nd_{1-x}Pr_x)_{2/3}Sr_{1/3}MnO_3$", Solid State Communication **94**, 917 (1995).

2. Y.X. Jia, V.H. Crespi, Li Lu, K. Khazeni, A. Zettl, and M. L. Cohen, "Magnetotransport Properties of $La_{0.6}Pb_{0.4}MnO_3$ and $Nd_{0.6}(Sr,Pb)_{0.4}MnO_3$ Single Crystals", Phys. Rev. B **52**, 9147 (1995).

3. K. Khazeni, Y.X. Jia, Li Lu, V.H. Crespi, M.L. Cohen, and A. Zettl, "Effect of Pressure on magnetoresistance of Single Crystal $Nd_{0.6}(Sr,Pb)_{0.4}MnO_3$", Phys. Rev. Lett. **76**, 295 (1995).

4. V.H. Crespi, Li Lu, Y.X. Jia, K. Khazeni, M.L. Cohen, and A. Zettl, "Thermopower of Single Crystal $Nd_{0.6}(Sr,Pb)_{0.4}MnO_3$", Phys. Rev. B **53**,14303 (1995).

5. K. Khazeni, V. H. Crespi, Y.X. Jia, Li Lu, M.L. Cohen, and A. Zettl, "Resistivity and Magnetoresistance of $Nd_{0.6}Pb_{0.4}MnO_{3-x}$ single crystal under pressure", Jour. Phys. Cond. Matter, **8**, 7725-7733 (1996).

6. J. Hone, M. S. Fuhrer, K. Khazeni, and A. Zettl, "Electrical Transport Measurements of KC_{60}", Phys. Rev. B **52**, R8700 (1995).

7. J. Hone, K. Khazeni, and A. Zettl, "Electrical Transport and Phase Transitions in Polymerized AC_{60} (A: K,Rb,Cs)", Proceedings of the WEPNM 1996, H. Kuzmany, ed. (1996).

8. K. Khazeni, J. Hone, J. Nguyen, R. Jeanloz, and A. Zettl, "Transport and structural properties of polymerized AC_{60} (A=K, Rb) under zero and high pressure conditions", Appl. Phys. A **64**, 263 (1997).

9. K. Khazeni, Vincent H. Crespi, J. Hone, Marvin L. Cohen, and A. Zettl, "Universal behavior of resisitivity in compressed polymerized AC_{60} (A=K, Rb)", submitted to Phys. Rev. Lett.

10. J. Hone, K. Khazeni, M. Muno, Vincent. H. Crespi, J. Nguyen, R. Jeanloz, Marvin, L. Cohen, and A. Zettl, "Electrical transport, thermoelectric, and structural measurements of polymerized AC_{60} (A=K, Rb) under zero and applied pressure", Proceedings of the IWEPNM 1996, H. Kuzmany, ed. (1997).

Chapter 1

Introduction to manganites

1.1 General introduction

Perovskite manganites were studied extensively in the early 1950's[1]. It was not until recently that their phenomenal magnetoresistance was appreciated[2]. An explanation for this extraordinary large magnetoresistance is the goal of ongoing intense research. It is also of interest to industry for its potential applications, such as magnetic switches, magnetic transducers, and magnetic read-heads for computers.

When appropriately doped, the manganites undergo a ferromagnetic transition at the Curie temperature T_c. The so-called Colossal Magneto-Resistance (CMR) in these materials arises from a strong correlation between the magnetic properties of the sample and the electronic transport in an applied magnetic field. The microscopic origin of CMR is still the subject of much controversy, but theoretical considerations and experimental facts hint toward a conduction mechanism based on "magnetically-induced lattice-polarons" in which a "dynamic" Jahn-Teller distortion follows the Mn^{3+} ions as electrons hop from Mn^{4+} to Mn^{3+} ions.

Early reports showed a gradual improvement in obtaining greater magnetoresistance (MR), but it was quickly realized that the magnitude of the magne-

toresistance in the manganites scales with T_c: the lower the Curie temperature, the larger the magnetoresistance. In fact there seems to be a universal trend in the magnitude of the magnetoresistance that all appropriately doped manganites follow. This universal behavior is discussed in chapter 3.

Chapter 5 focuses on the effects of hydrostatic pressure on the transport properties of single crystals of $Nd_{0.62}Pb_{0.30}MnO_{3-\delta}$. It will be shown that the low-temperature ferromagnetic phase is stabilized under pressure, i.e. the Curie temperature increases with increasing temperature. The corresponding magnetoresistance decreases with increasing T_c, which is consistent with the universal behavior of MR discussed in chapter 3.

1.2 Structure

The so-called colossal magnetoresistance (CMR) manganites crystallize in the perovskite structure of the mineral perovskite, $CaTiO_3$. Figure 1.1 shows the unit cell of perovskite ABO_3; A denotes a large ion, such as a lanthanide (La^{3+}, Pr^{3+}, Nd^{3+}, Gd^{3+}), Y^{3+}, Pb^{2+}, Cd^{2+}, or an alkali earth (Ca^{2+}, Sr^{2+}, Ba^{2+}); while B denotes a small ion such as Al^{3+}, Cr^{3+}, Mn^{3+}, Fe^{3+}, Ti^{4+}, or Mn^{4+}. The A ions occupy the corners of the cubic unit cell, the B ion is located at the center of the cube, and the oxygen ions are at the centers of the faces of the cube, forming an octahedron enclosing the B ion at its center. In the particular case of perovskite manganites, the B ions are either Mn^{3+}or Mn^{4+}. When more than one species of the A ions are present, the B ions are a mixture of Mn^{3+}or Mn^{4+}.

The structure of the mixed-valence manganites depends sensitively on the

ABO_3

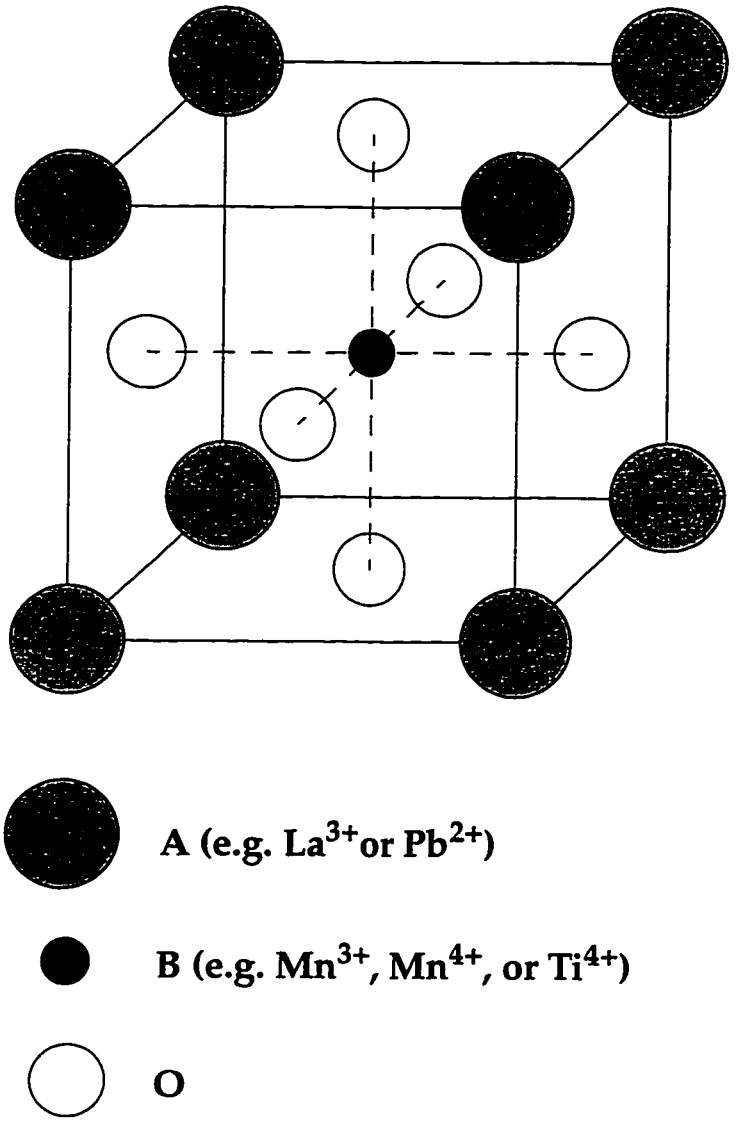

Figure 1.1. Perovskite Unit Cell

Mn^{4+} content, i.e. they change structure in response to changes in composition. When the Mn^{4+} content is ~10%, the structure is orthorhombic. At 26% Mn^{4+} concentration, the structure becomes rhombohedral, and 30% Mn^{4+} concentration results in a cubic structure[3]. $La_{1-x}Sr_xMnO_3$ undergoes a structural phase transition from orthorhombic to rhombohedral with increasing temperature, for a limited range of compositions x[4,5]. It has been shown that for a carefully tuned composition, namely x=0.17, the structural phase transition in $La_{1-x}Sr_xMnO_3$ can be driven by an external magnetic field[6].

The structure of the mixed-valence manganites can also change spontaneously. Later in this chapter, the magnetic properties of the mixed-valence manganite will be discussed. It will be shown that, in the range ~0.25<x<~0.50, these materials undergo simultaneous insulator-to-metallic and paramagnetic-to-ferromagnetic phase transitions upon cooling through the Curie temperature T_c. The lattice parameters decrease abruptly at this transition, giving rise to a large (ΔV=0.13%) abrupt decrease in the volume of the unit cell[7]. This change in volume is related to a complex interplay between the magnetic and transport properties in this family of compounds. A possible theoretical explanation for some of these unusual behaviors will be discussed in chapter 3.

It is noteworthy that some manganites, such as $YMnO_3$ and $SrMnO_3$, do not crystallize in perovskite structure; but their binary crystal forms, such as $Y_{0.4}Sr_{0.6}MnO_3$, do crystallize in the perovskite structure[1].

1.3 Historical review

Various polycrystalline samples of the manganites $LaMnO_3$ and $MeMnO_3$ (Me = large divalent ion) were prepared and studied by G. H. Jonker and J. H. Van Santen in 1950[1]. They also studied some binary systems: [$LaMnO_3$ - $CaMnO_3$], [$LaMnO_3$ - $SrMnO_3$], [$LaMnO_3$ - $BaMnO_3$], [$LaMnO_3$ - $CdMnO_3$], and [$LaMnO_3$ - $PbMnO_3$]. The samples were made by solid reaction of stoichiometric amounts of the carbonates or the oxides of the metals pre-fired at 1000 °C and fired between 1350 and 1450 °C. Since the magnetic properties of the manganites depend sensitively on the relative concentrations of the Mn^{4+} and Mn^{3+} ions, they measured their samples' manganese ion concentrations by wet-chemical titration for various firing temperatures and firing atmospheres. They concluded that the "mixed-valence" perovskite manganites become ferromagnetic within a certain range of the Mn^{4+}/Mn^{3+} concentrations, with the Curie temperatures ranging up to about 400 °C. They showed that all of the magnetic and structural parameters are functions of the Mn^{4+} concentration. For example, they plotted the Curie temperature vs. percentage of the Mn^{4+} and determined that in the range $0<x<0.5$, these compounds have a ferromagnetic ground state (notice that the concentration of the Mn^{4+} ion is the same as x in the formula unit if the stoichiometry is complete). Severe deviation from cubic structure was found for the range $0<x<0.25$. They also determined the crystal structure of their polycrystalline samples and confirmed Goldschmidt's criterion[8] for a stable perovskite structure which states that the parameter t, defined by

$$t = \frac{(r_A + r_O)}{\sqrt{2}(r_B + r_O)} \qquad \text{eq. 1. 1}$$

(where r_A , r_B , r_O denote respectively the radii of the ions in ABO_3), should approximately be equal to unity for a stable perovskite structure. A purely cubic structure is found if the parameter t is exactly equal to unity ($SrTiO_3$), otherwise the structure is slightly distorted. For large deviations from unity completely different crystal structures are found.

The pioneering work of Jonker and Van Santen on mixed-valence perovskite manganites paved the way for E. O. Wollan and W. C. Koehler's[9] neutron diffraction study on the perovskite manganite $La_{1-x}Ca_xMnO_3$ in 1955. Their neutron diffraction data were complemented by X-ray diffraction measurements of lattice distortions. They showed that the x=0 compound $LaMnO_3$ is ferromagnetically ordered in the ab-plane and anti-ferromagnetically aligned in the c direction; hence, the crystallographic unit cell is doubled in the c direction to obtain the magnetic unit cell. Notice that if the stoichiometry is complete, all of the manganese ions are in the Mn^{3+} ionic state. At the other end of the spectrum, the compound $CaMnO_3$ is anti-ferromagnetically ordered in an octahedral coordination which requires doubling of the crystallographic unit cell in all three directions to obtain the magnetic unit cell. All manganese ions are in the Mn^{4+} ionic state in $CaMnO_3$.

The first extensive theoretical study of electronic mobility in mixed-valence manganites was undertaken by P. -G. deGennes[10]. Following the "double-

exchange" theory developed by C. Zener[11] in 1951, and treating the electrons in a tight-binding approximation, deGennes showed that in the range $0<x<0.5$ in $La_{1-x}Ca_xMnO_3$, the Mn spins become canted, leading to a simultaneous occurrence of both ferromagnetism and electrical conductivity.

Single crystals are important in identifying intrinsic properties of materials. Single crystals of the mixed-valence manganites, specifically $(LaPb)MnO_3$, were first obtained in 1969 by A. H. Morrish *et al.*[12] using a flux-melt method. The flux-melt technique to grow single crystals of manganites will be discussed in detail in chapter 2. A. H. Morrish *et al.* characterized their $La_{1-x}Pb_xMnO_3$ crystals by X-ray fluorescence, wet chemical, and electron microprobe techniques. They showed that the stoichiometry is uniform throughout their crystals with $0.25<x<0.45$, the range in which spontaneous ferromagnetism and metallic resistivity occur simultaneously below the Curie temperature. After this breakthrough, a rapid series of papers was published by the same authors, in collaboration with others, on magnetization[13], ferromagnetic resonance absorption[14], electrical conductivity[15], and lattice parameter[16] measurements. These measurements showed that ferromagnetism, electronic transport, and the lattice parameters are all strongly correlated in mixed-valence perovskite manganites. In fact attempts were made to find an empirical relation between the magnetization and resistivity[15], but the relation did not hold for large ranges of resistivity. Magnetoresistance was also measured[15] and found to be negative (resistivity decreased in an applied magnetic field), with a magnitude of ~ 20% at its maximum at the Curie temperature, in a magnetic field of 1 Tesla (figure 1.2).

In 1989 R. M. Kusters *et al.*[17] measured the magnetic susceptibility and magnetoresistance of single crystals of $Nd_{0.5}Pb_{0.5}MnO_3$ and explained the results in terms of hopping of localized magnetic polarons above and around the Curie temperature (figures 1.3 and 1.4).

In 1993 Ken-ichi Chahara *et al.*[18] reported a giant magnetoresistance in thin films of $La_{0.72}Ca_{0.25}MnO_\delta$ grown by an ion beam sputtering method on magnesium oxide single crystal substrates (figure 1.5). But It wasn't until 1994, when Jin *et al.* reported[2] a "Thousandfold Change in Resistivity in Magnetoresistive La-Ca-Mn-O Films", that a renewed interest in mixed-valence perovskites erupted in the physics community. They reported a 127000% magnetoresistance (MR) in thin films of $La_{0.67}Ca_{0.33}MnO_3$ grown by pulsed laser deposition (PLD) technique (figure 1.6). The MR ratio is defined here as

$$\frac{\Delta\rho}{\rho} = \frac{[\rho(H) - \rho(0)]}{\rho(H)} \qquad \text{eq. 1. 2}$$

which can be larger than 1. This way of defining MR has an advantage over the conventional definition (which is similar to equation 1.2 but has R(0) in the denominator) in that it is easier to distinguish between two different values of MR that happen to be seemingly very close to each other, such as 99% and 99.99%. Since 1994, there have been numerous reports on the manganites regarding their resistivity, magnetoresistance, magnetostriction, lattice distortion, magnetization, and magnetic susceptibility which we will refer to in the body of this thesis. Recently, there have been reports on related structures such as layered manganites[19] which are beyond the scope of this thesis. The binary crystals of

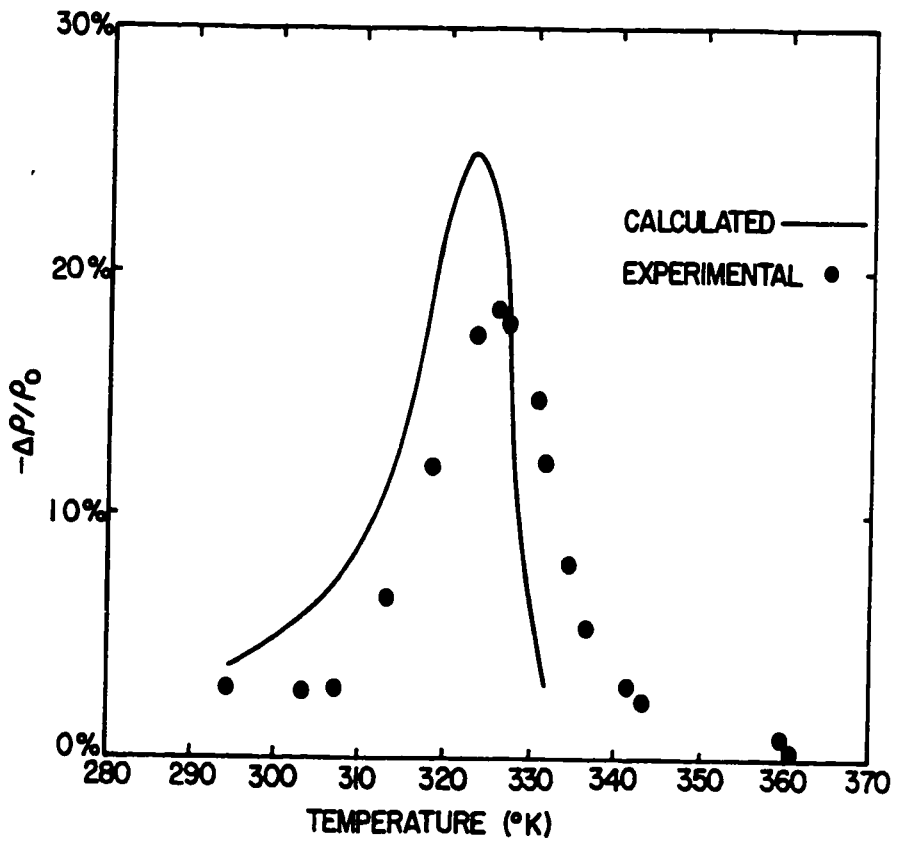

Figure 1.2. Magnetoresistance as a function of temperature for a single crystal sample of $La_{0.69}Pb_{0.31}MnO_3$[15].

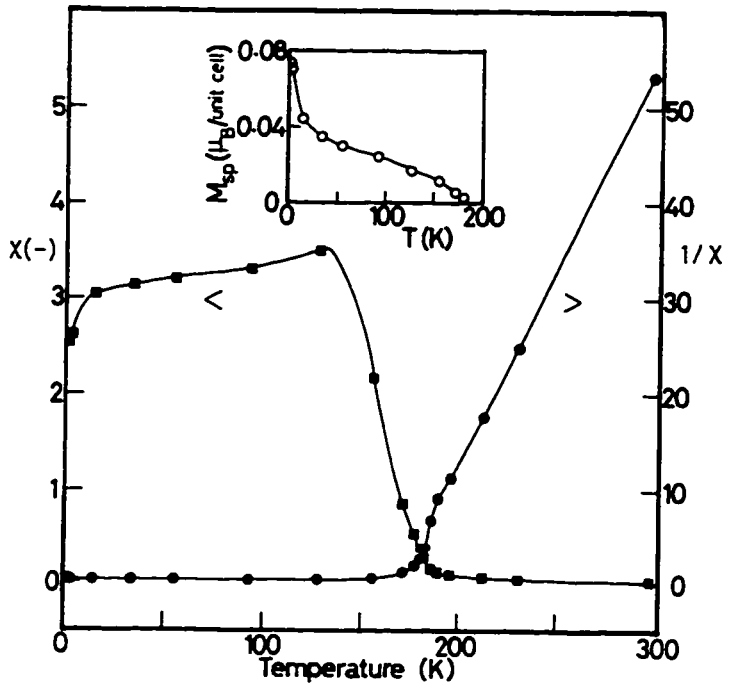

Figure 1.3. Magnetic susceptibility and its inverse as functions of temperature for a single crystal sample of $Nd_{0.5}Pb_{0.5}MnO_3$[17]. The inset shows the spontaneous magnetization.

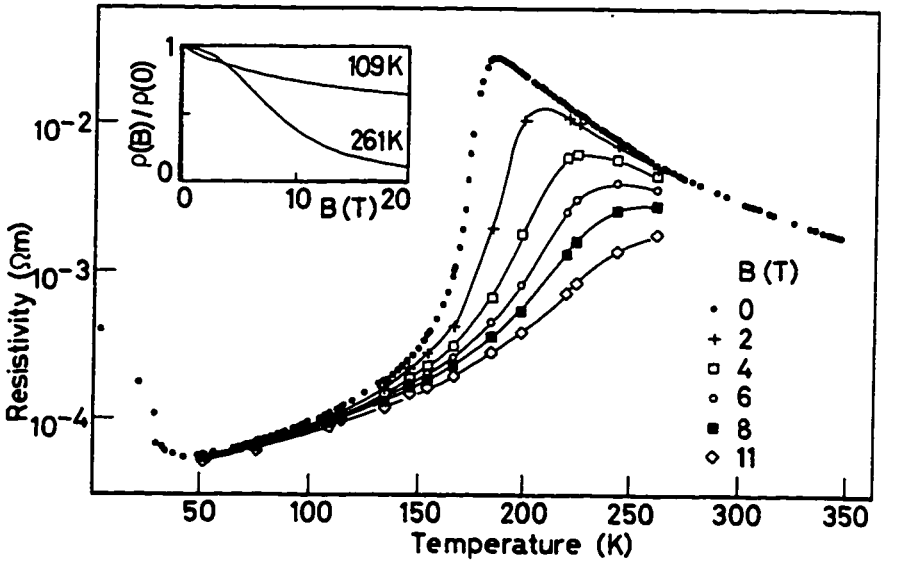

Figure 1.4. Magnetoresistance of the sample of figure 1.3. The inset shows the behavior of the resistivity as a function of applied magnetic field[17].

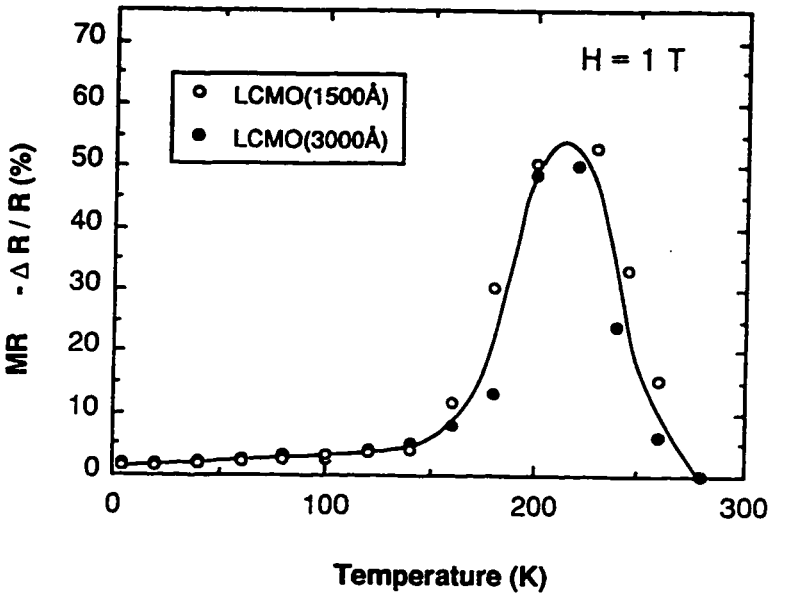

Figure 1.5. Magnetoresistance of two different sputtered films of $La_{1-x}Ca_xMnO_\delta$ as a function of temperature[18]. The inset indicates the thickness of the films.

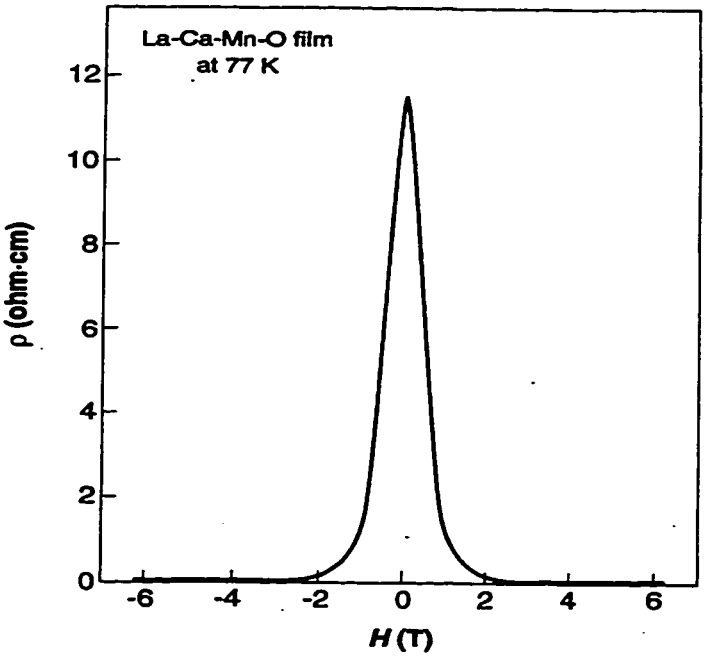

Figure 1.6. Magnetoresistance of a pulsed laser deposited film of $La_{0.67}Ca_{0.33}MnO_3$ as a function of applied magnetic field[2].

perovskite manganites, the so-called mixed-valence manganites, or commonly known as doped manganites are the subject of the next section.

1.4 Doped manganites

When two or more species of the A ions with different valencies are present in a manganite crystal (see figure 1.1), the manganese ions are forced to assume two different ionic states, namely Mn^{3+} and Mn^{4+}, in order to keep the whole crystal neutral (the ionic charges in the formula unit should add up to zero). To emphasize the ionic charges, the formula unit is simetimes written as $(A^{3+}_{1-x}B^{2+}_{x})(Mn^{3+}_{1-y}Mn^{4+}_{y})O^{2-}_{3}$, where A is an atom in the ionic state of 3+ such as La^{3+}, and B an atom in ionic state of 2+ such as Ca^{2+}. Notice that the neutrality requirement forces the concentration of Mn^{4+}, y, to be equal to x, the concentration of B^{2+}; hence, the formula unit is commonly written as $A_{1-x}B_xMnO_3$.

1.5 Magnetic properties

Neutron diffraction studies[9], complemented by X-ray diffraction measurements, of the series of perovskites $La_{1-x}Ca_xMnO_3$ in the range $0<x<1$ have revealed that the end members, x=0 and x=1, are antiferromagnetic with Neel temperatures around 140 K, but that the magnetic unit cells at x=0 and at x=1 are different. Figures 1.7 and 1.8 show the magnetic unit cells of $LaMnO_3$ (x=0) and $CaMnO_3$ (x=1), respectively. Notice that the magnetic unit cell of $LaMnO_3$ is only twice as large as the crystallographic unit cell (doubled in the c-direction),

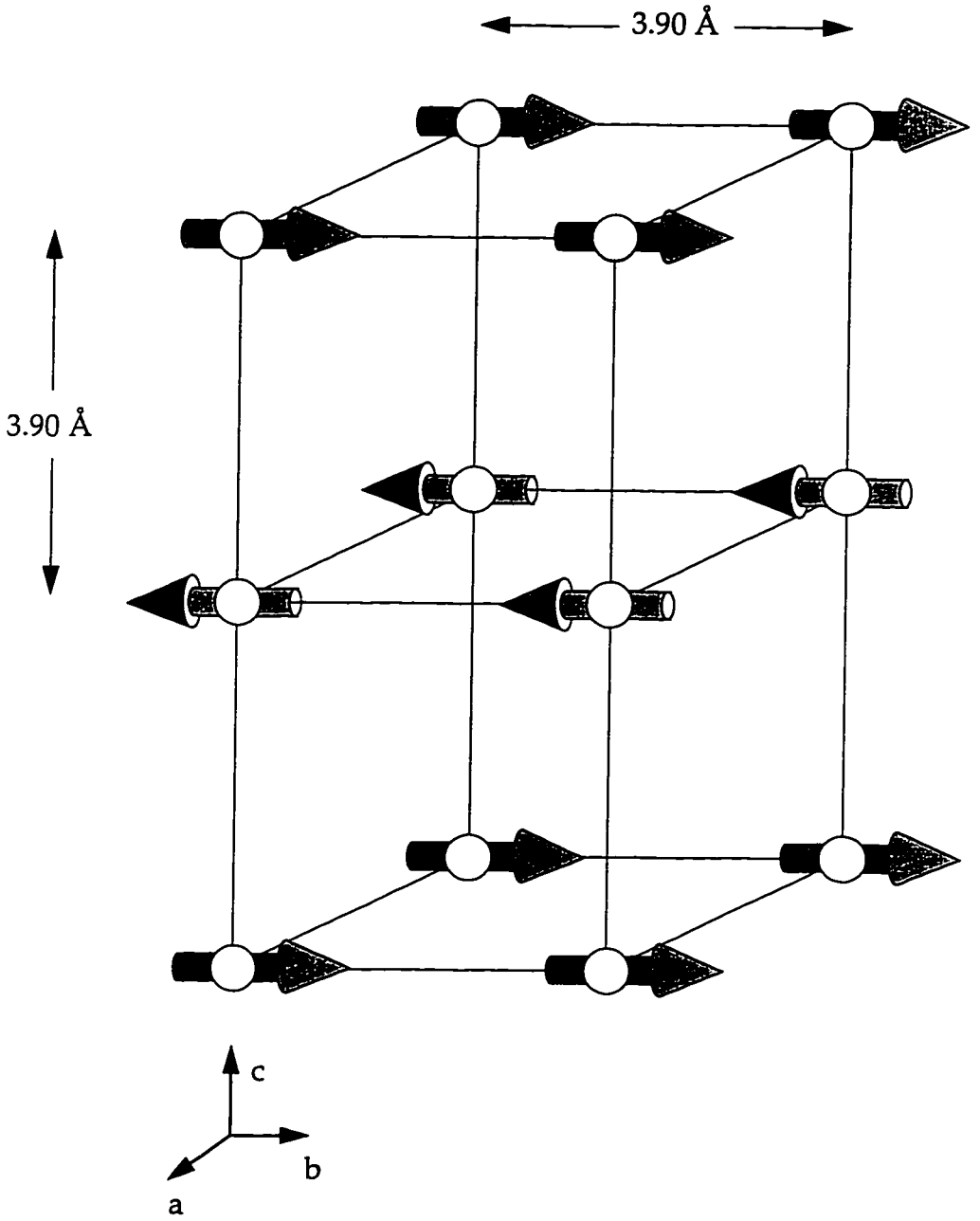

Figure 1.7. The magnetic unit cell of the antiferromagnet $LaMnO_3$[9]. The arrows refer to the local Mn ion spins. Only the manganese ions are shown.

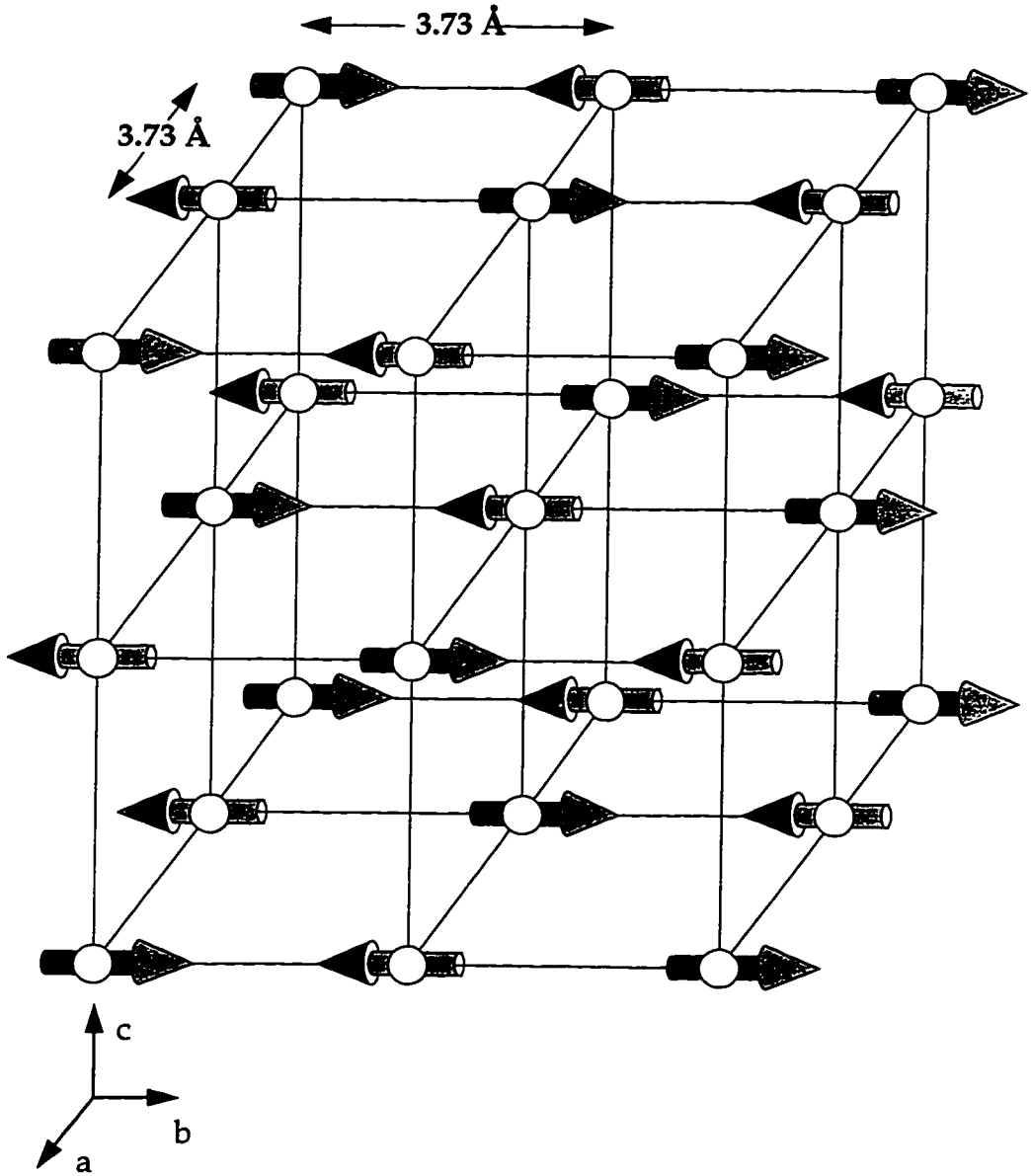

Figure 1.8. The magnetic unit cell of the antiferromagnet $CaMnO_3$[9]. The arrows refer to the local Mn ion spins. Only the manganese ions are shown.

whereas the magnetic unit cell of $CaMnO_3$ is double that of the crystallographic unit cell in all three directions. The other important thing to notice is that the spins of the manganese ions in $LaMnO_3$ are ferromagnetically ordered in the **ab** plane and antiferromagnetically ordered in the **c** direction; hence, the crystal as a whole is an antiferromagnet. The spins of the manganese ions in $CaMnO_3$ have octahedral coordination, i.e. each manganese ion is completely surrounded by six nearest neighbor manganese ions with opposite spin orientations.

The magnetic properties of the mixed-valence manganites strongly depend on the value of x (which is the same as the Mn^{4+} content) and temperature. Figure 1.9 shows the magnetic phase diagram of $La_{1-x}Ca_xMnO_3$. The materials are ferromagnetic insulators for $0<x<0.17$, with Curie temperatures ranging from 160 to 200 K. For $0.17<x<0.50$, they are ferromagnetic metals, with Curie temperatures starting from 200 K at x~0.17, reaching a maximum of ~260 K around x=0.33, and going back down to ~200 K at x=0.5. Beyond x=0.5, $La_{1-x}Ca_xMnO_3$ materials are antiferromagnetic insulators with Neel temperatures between 120 and 260 K. The magnetic phase diagram of other mixed-valence manganites is similar to that of $La_{1-x}Ca_xMnO_3$, although of course the actual values of the Curie and Neel temperatures[1] differ. It should be mentioned that it is not necessary to introduce any divalent ions to get any Mn^{4+} content. It has been shown[20] that $La_{1-\delta}Mn_{1-\delta}O_3$ has a magnetic phase diagram similar to figure 1.4 as a function of δ (cation vacancy): it undergoes a ferromagnetic phase transition with a substantial Mn^{4+} content (33%) for $\delta=0.055$.

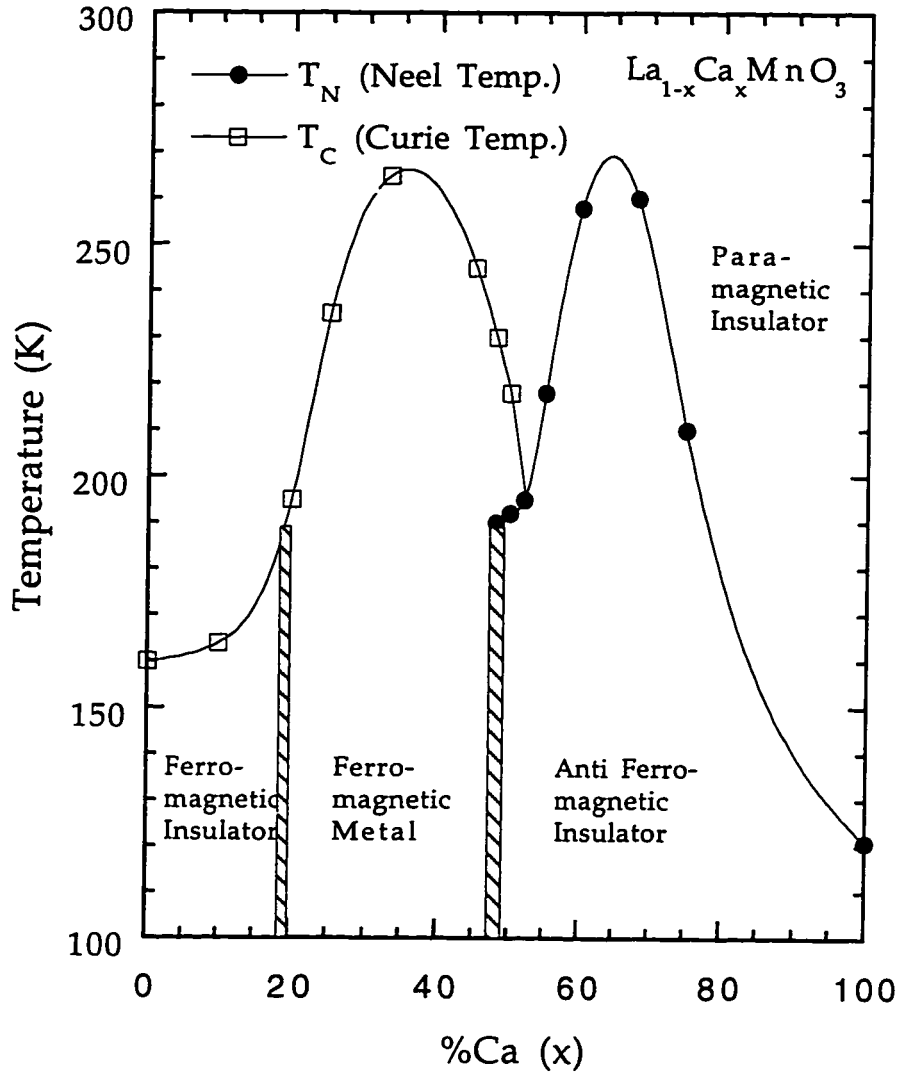

Figure 1.9. Magnetic phase diagram of $La_{1-x}Ca_xMnO_3$ (after reference 34).

As mentioned earlier, low-temperature ground states of the mixed-valence manganites are metallic ferromagnets in the range ~0.20<x<~0.50. The materials are metallic in the sense that their resistivities decrease with temperature, which is characteristic of metals. This is the range in which manganites have been studied more intensely. The magnetic behavior of the manganites is extremely rich and strongly correlated to their transport properties. This "magneto-transport" is the subject of chapter 3.

Chapter 2

Crystal growth and resistivity measurements techniques

2.1 Crystal growth

Most measurements on the manganites have been performed on their polycrystalline and thin film forms. Performing measurements on single crystals is important in probing the physical properties of materials, especially the electronic transport, since the presence of impurities, grain boundaries, and defects can in principle mask the intrinsic behavior of the system.

The mixed-valence perovskite manganite crystals used in the studies presented in this thesis were grown by Dr. X. Y. Jia and the author of this thesis here in the Zettl group's materials synthesis laboratory at U. C. Berkeley[21]. The crystals were grown by the flux technique, motivated by the work of A. H. Morrish *et al*[12]. In this method, the constituents of the final product, which are in the form of oxides and carbonates, are mixed in stoichiometric amounts with another low-melting-temperature oxide/fluoride called the flux. The mixture is then heated above the melting temperature of the flux. This final temperature (soak temperature) is maintained for 1 to 2 days and then slowly reduced over two to three weeks to allow for the formation of crystals.

The flux acts as a solvent, mixing the constituents into a uniform "melt", and should evaporate much more quickly than the other materials, i.e. should

have the highest vapor pressure among all constituents at elevated temperatures. It is difficult to find a suitable flux for the manganites since the oxides and the carbonates of the constituents have varying melting/vapor-pressure temperatures with large differences. Another problem with the flux technique is that the final crystals can have significant amount of the flux's constituents in them as inclusions. Therefore the problem becomes that of finding the "right" flux. The right flux to grow Pb doped $LaMnO_3$ was found by Morrish *et al.*[12] to be 1:1 mixture (by weight) of PbO and PbF_2. Note that Pb is not only a part of the final product, but also a part of the flux. This technique is called the self-flux method. It should be mentioned that a successful crystal synthesis run, one that leads to a large number of good single crystals, depends on a variety of factors such as evaporation losses which are unique to a particular situation.

The optimum mixture and temperature schedule to grow the crystals used in this study were found to be as follows. A 4.56:1 by weight mixture of flux (1:2 by weight of PbO and PbF_2 respectively) and stoichiometric $La_{0.67}Pb_{0.33}Mn$, $Nd_{0.67}Pb_{0.33}Mn$, or $Nd_{0.67}Sr_{0.33}$ Mn powders in the form of oxides and carbonates, was finely ground and loaded into a platinum crucible (1× 1× 2 inch) covered by a platinum lid. The loaded platinum crucible was then placed inside a larger alumina crucible and was covered with an alumina plate. The whole assembly was transferred inside a high temperature furnace which was located inside a fume hood. The temperature of the furnace was controlled with a programmable digital Omega temperature controller. The temperature of the furnace was set to go to ~1700 K from room temperature over 3 hours, stay at 1700 K for

16 hours, and then slowly cool down to 1300 K at a rate of 1 to 2 K/hour, at which point the furnace was turned off and samples were allowed to cool down to room temperature.

Thick, shiny, rectangular parallelepiped single crystals were extracted from the exposed top surface of the remaining solidified flux, as well as from inside the cavities of the solid flux. The typical dimensions of the crystals were 1 mm × 1 mm × 0.3 mm. The final stoichiometry was measured by Energy Dispersive X-ray (EDX) spectroscopy. The oxygen content of the crystals was not determined since EDX is not very sensitive to oxygen, but magnetization measurements on these samples (see chapter 3) indicated that the oxygen stoichiometry was very close to 3 (see for example reference 22). Figure 2.1 shows an X-ray diffraction pattern for a $Nd_{0.60}(Sr_{0.70}Pb_{0.30})_{0.40}MnO_{3-\delta}$ single crystal obtained by Dr. Y. X. Jia[21]. As it can be seen, only sharp (001) and (002) peaks are observed, demonstrating the high quality of the crystal. From the X-ray diffraction data, the symmetry of the crystal was determined to be cubic with lattice constant of 3.86 Å. Crystals of $La_{0.67}Pb_{0.33}MnO_3$, $Nd_{0.67}Pb_{0.33}MnO_3$, and $Nd_{0.67}Sr_{0.33}$ MnO_3 were similarly grown and characterized. These crystals again proved to be of high quality and uniformity.

2.2 Magneto-resistivity measurements

Resistivity measurements on the single crystals were performed using the standard four-probe method (see figure 2.2). Two 1 to 2 cm long annealed gold wires (1 to 2 mil diameter) were glued to the ends of long rod-shaped crystals

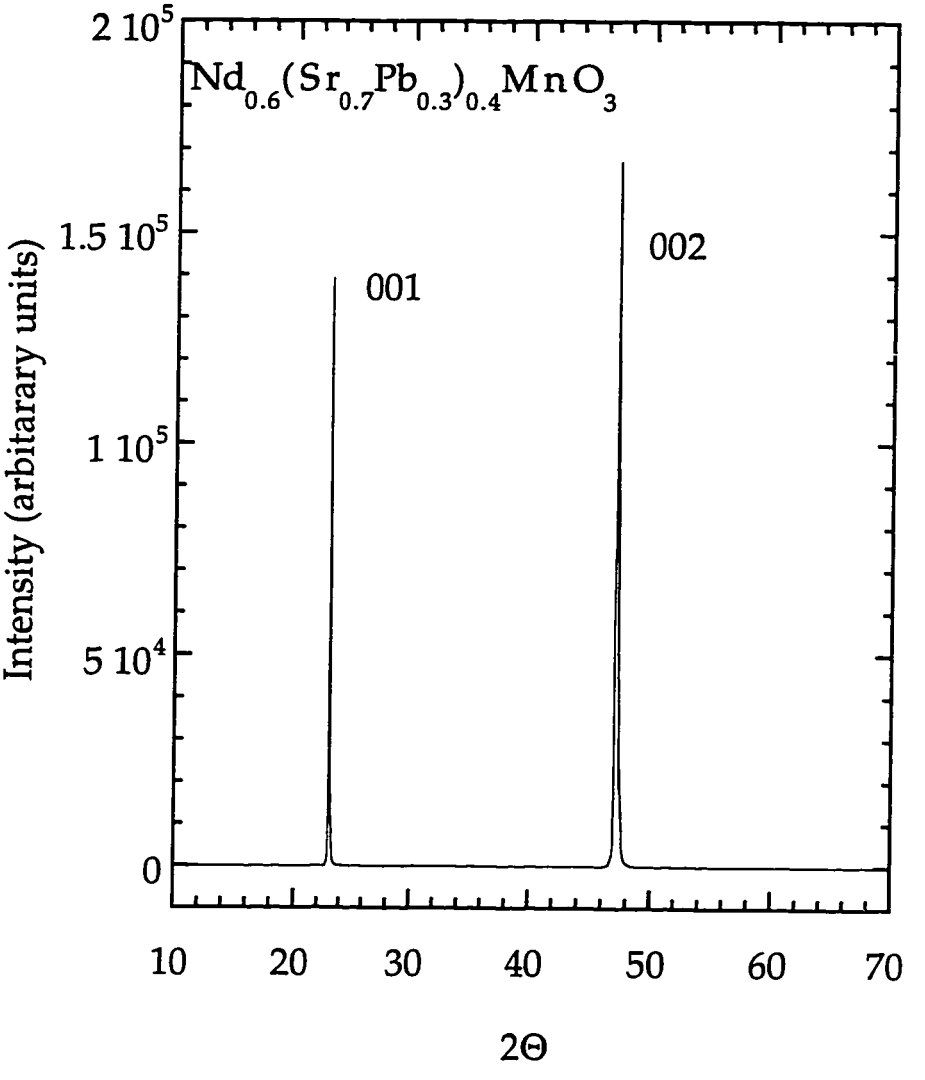

Figure 2.1. X-ray diffraction pattern of a single crystal of $Nd_{0.60}(Sr_{0.70}Pb_{0.30})_{0.40}MnO_{3-\delta}$ obtained by Y. X. Jia[21].

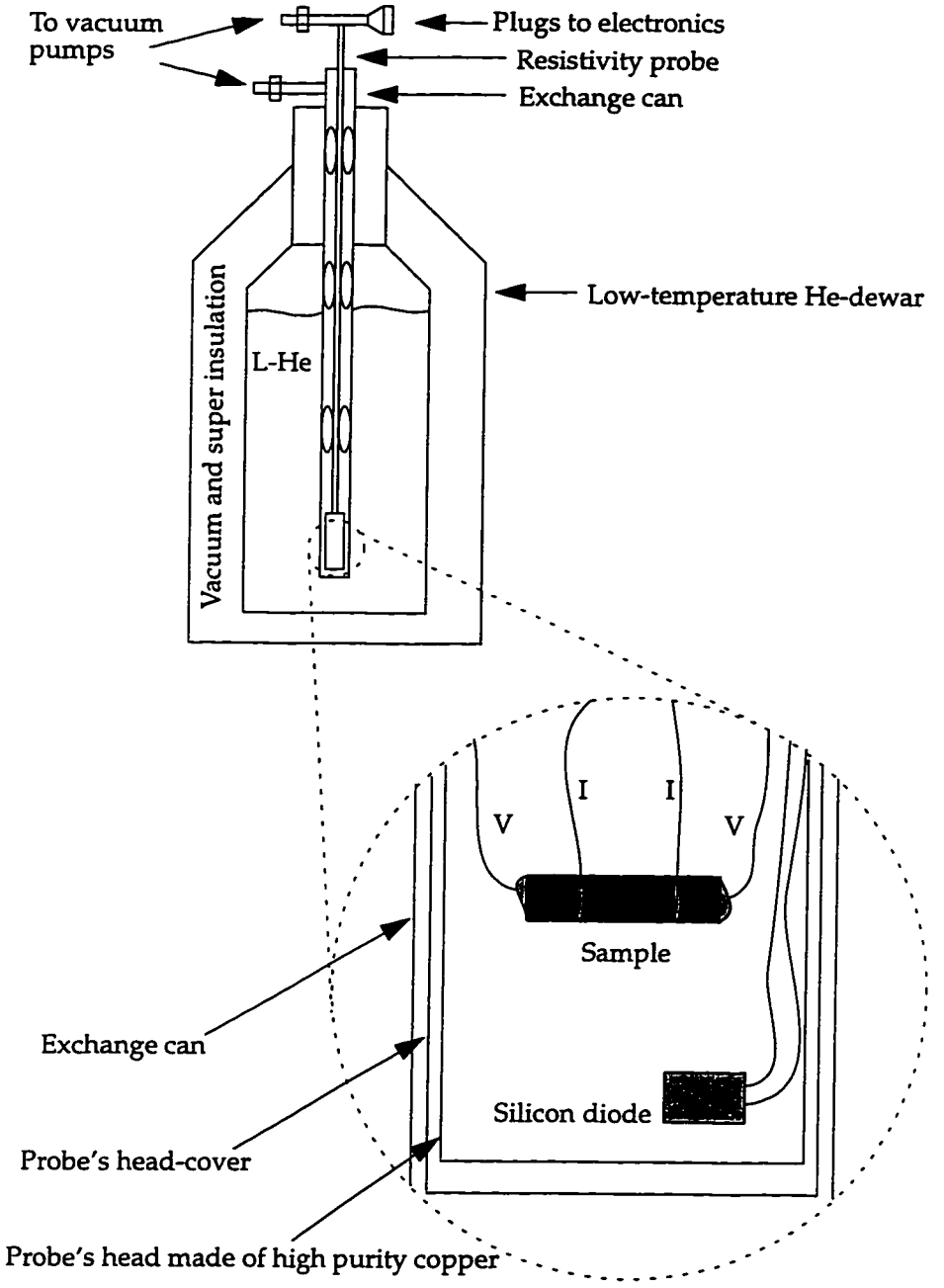

Figure 2.2. Schematic of the resistivity measurement.

using silver paint. These wires are used to run current (I) through the sample. Two other gold wires of the same size were glued to the top face of the crystal to measure the voltage drop (V) across the sample. The resistance is then V/I. The resistivity is $\rho = R(L/A)$, where L is the distance between the voltage leads and A is the cross sectional area of the crystal. The sample was then placed on a low-temperature probe and slowly cooled down to 4.2 K in a liquid He dewar, while the resistivity was monitored at small temperature intervals, usually every 1 K. Since the wires that run to the sample travel distances of the order 1 to 2 meters from the bottom of the dewar to the electronics outside, the voltage measurements can be affected by the induced emf's due to the thermal gradients along the wires and the stray electromagnetic fields present in the laboratory. To cancel these effects, the voltage difference V was measured for both directions of the dc current I, and the average of the two measurements was taken to be the actual voltage drop across the sample. The temperature was read by a calibrated silicon diode (Lakeshore model DT-470). Since the temperature was typically drifting while the resistivity of the sample was read, the temperature corresponding to a particular resistivity datum was assigned as follows. For each set of data, R versus T, the first thing to measure was the temperature, say T_1. Then the resistivity would be read by the average method explained above. Finally the temperature would be read once again, say T_2. The temperature corresponding to the value of the resistance would then be assigned as $T = (T_1+T_2)/2$, the average of the two temperatures. The rate of change of temperature, dT/dt, was controlled by the amount of the exchange gas (He) in the exchange can (see figure 2.2).

The amount of current used to measure the resistivity is also important. A large current can cause excessive heating of the sample; therefore, the value of the temperature read by the diode (see figure 2.2) would not correspond to the true temperature of the sample. In order to minimize this effect, current was chosen so that the amount of heat generated would be less than or equal to 1 μJ. There are other measures one can take to minimize this effect. One is that the sample should be very well heat-sunk near the temperature-sensing diode. The other thing to watch is the resistivity of the silver-painted contacts, called the contact resistance. Since the current runs through the contacts and the sample in series, the heat generated by the contact resistance can also be significant. The total resistance of the sample and the current contacts should be such that the heat generated remains less than 1 μJ.

Magnetoresistance is simply the resistance of the sample in the presence of a uniform magnetic field (although conventionally, magnetoresistance is defined by equation 1.2). The magnetic field used in these experiments was generated by a superconducting solenoid operating at liquid He temperature (4.2 K) with a maximum field of 8 Tesla, uniform over a 1 cm radius, at its center. The resistivity probe was designed to be inserted into the bore of the superconducting magnet, so no modifications were needed for the magnetic measurements of the resistivity. The silicon diode cannot be used when a magnetic field is present because it has a very large magnetic field-dependent response. The temperatures in the presence of the magnetic field were therefore measured with a calibrated carbon-glass resistor (Lakeshore model CGR).

Chapter 3

Magnetization and Magneto-transport

3.1 Magnetization and magnetic susceptibility

3.1.1 General overview

A ferromagnetic solid has a spontaneous magnetic moment, i.e. it is magnetized even in zero applied magnetic field. The temperature below which the spontaneous magnetization occurs is called the Curie temperature T_c. Above T_c a ferromagnet acts as a paramagnet. The magnetization **M** is defined as the magnetic moment per unit volume in thermal equilibrium. A macroscopic ferromagnetic sample is usually divided into magnetic domains. Therefore **M** is the value of the magnetization inside a single magnetic domain. The magnetization of each domain points in a particular direction in order to oppose the effect of the other magnetic domains. As a result, the magnetic field produced outside the sample, by the sample as a whole, is very close to zero. This effect was first explained by Landau and Lifshitz as a natural consequence of various contributions to the energy (exchange, anisotropy, and magnetic) of a ferromagnetic object. There is a critical size, which is about 300 atoms in the case of iron[23], below which the entire ferromagnetic sample consists of one domain. But most everyday ferromagnetic samples consist of a large number of magnetic domains.

Today, the magnetization of a ferromagnet is typically measured by a

device called the SQUID magnetometer. In order to measure the spontaneous magnetization of a ferromagnetic sample, it is necessary to apply a finite uniform magnetic field to the sample under investigation. This external field partially aligns the magnetic domains inside the sample so that the measured magnetization corresponds to the correct value of **M** inside a domain.

A plot of the magnetization versus the applied magnetic field typically shows a gradual increase of the magnetization from zero to a final saturation value $\mathbf{M}_s$, at an applied saturating magnetic field $\mathbf{B}_{ap}^{s}$. Beyond $\mathbf{B}_{ap}^{s}$ the magnetization does not increase with the applied field. For small values of $\mathbf{B}_{ap}^{s}$ the material is called a soft magnet, otherwise it is called a hard magnet. There exist ferromagnets with different saturation magnetizations for a magnetic field applied in different crystallographic directions. In such cases the material has at least one hard axis. Figure 3.1 shows a schematic plot of **M** vs. $\mathbf{B}_{ap}$ for such material.

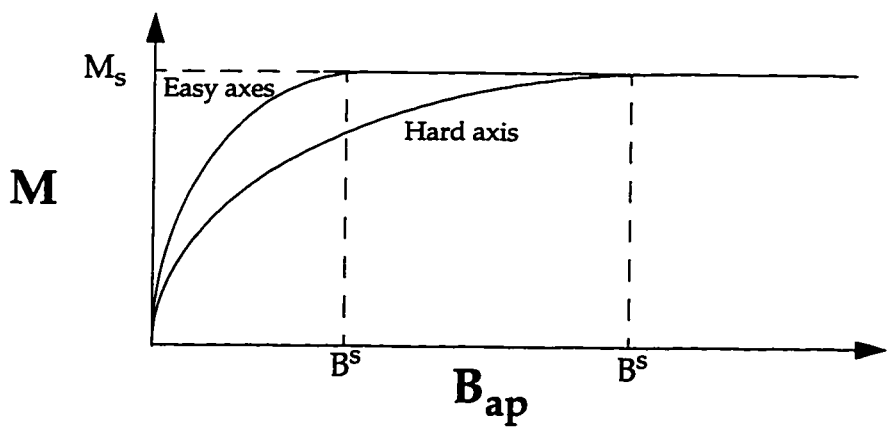

Figure 3.1. A typical Plot of M vs. B_{ap} (M_s is the saturation magnetization and B^s is the saturating applied magnetic field).

The magnetization **M** is zero above the Curie temperature, so we can only talk about the magnetic susceptibility above T_c. The magnetic susceptibility χ is defined as $\frac{\mathbf{M}}{\mathbf{B}_{ap}}$,where $\mathbf{B}_{ap}$ is the applied magnetic field. There are many calculations based on various models to calculate the magnetic susceptibility. In the simplest approach[23] one assumes that each magnetic atom experiences a net magnetic field proportional to the magnetization $\mathbf{B}_{net}=\lambda\,\mathbf{M}$, where λ is independent of temperature. This so-called mean field approximation predicts

$$\chi \sim \frac{1}{(T - T_c)} \qquad \text{eq. 3.1}$$

which is called the Curie-Weiss law. It describes fairly well the observed susceptibility in the paramagnetic region above T_c. It is worth mentioning that detailed calculations[24] predict

$$\chi \sim \frac{1}{(T - T_c)^{1.33}} \qquad \text{eq. 3.2}$$

for temperatures very close to T_c (from above) which is in good agreement with the observed experimental data. The mean field approximation can also be used to calculate the temperature dependence of the magnetization below T_c[23]. The results show that for temperatures much less than the Curie temperature

$$\frac{\Delta M}{M(0)} = 2N\mu e^{-2\frac{T_c}{T}} \qquad \text{eq. 3.3}$$

where $\Delta M = M(0) - M(T)$, N is the total number of magnetic atoms and μ is the magnetic moment of the atoms. For temperatures very close to the Curie temper-

ature, the mean field approximation predicts

$$\frac{\Delta M}{M} = N\mu\left(1-\sqrt{3}\left(1-\frac{T_C}{T}\right)^{\frac{1}{2}}\right) \qquad \text{eq. 3.4}$$

However, neither of the two limiting forms has been confirmed by experiment. It has been shown[25,26] experimentally that the critical exponent in the vicinity of the Curie temperature is 1/3 and not 1/2. The temperature dependence at low temperatures is also incorrect due to the existence of elementary ferromagnetic excitations called magnons. When magnons are taken into account[23], the fractional change of magnetization becomes

$$\frac{\Delta M}{M(0)} = AT^{\frac{3}{2}} \qquad \text{eq. 3.5}$$

where A is a constant independent of the temperature. Equation 3.5 is called the Bloch $T^{3/2}$ law, and has been confirmed experimentally.

3.1.2 Magnetization and magnetic susceptibility in manganites

Magnetization and magnetic susceptibility measurements on the mixed-valence manganites in the range $0.20<x<0.50$ show a ferromagnetic transition at a Curie temperature that ranges from ~50 to ~350 K. Figure 3.2 shows the magnetization as a function of temperature of a single crystal of $Nd_{0.6}(Sr_{0.7}Pb_{0.33})_{0.4}MnO_3$ (measurement performed by Y. X. Jia[21] using a SQUID magnetometer). The transition looks like a classical ferromagnetic transition, but at very low temperatures the magnetization has a slight upturn. This has also been seen by others[17] and to date no clear explanation has been given as to its origin, but recent Mössbauer

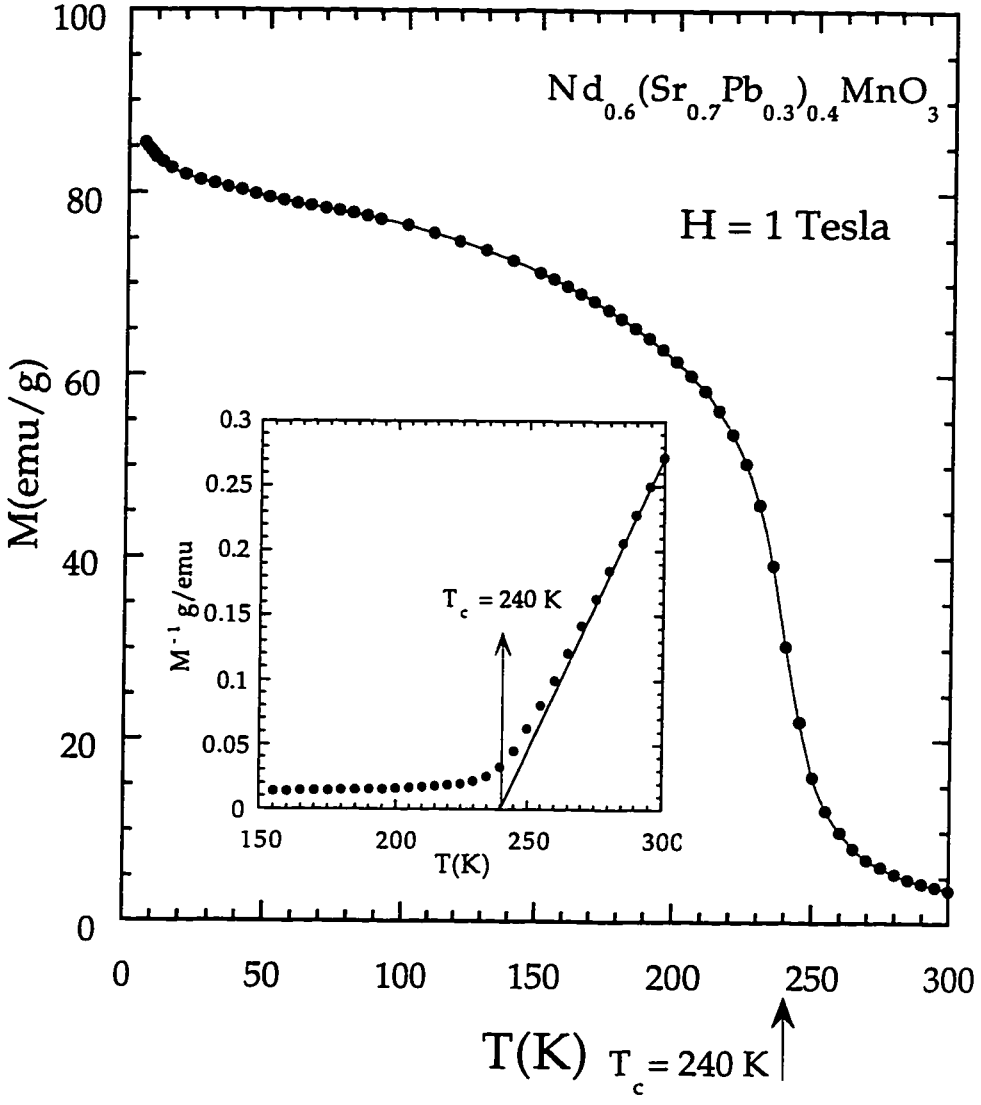

Figure 3.2. Magnetization of single crystal $Nd_{0.6}(Sr_{0.7}Pb_{0.33})_{0.4}MnO_3$ vs. temperature (measurement performed by Y. X. Jia[21]). Notice the upturn at the lowest temperatures. The inset shows the inverse of the magnetization.

spectroscopy studies[27] on $La_{1-x}Ca_xMnO_3$ have shown that both ferromagnetism and paramagnetism coexist below the Curie temperature. This could explain the observed upturn of the magnetization at very low temperatures. The value of the magnetization at T=0 can be theoretically estimated. At T=0 the spins of all of the manganese ions are aligned ferromagnetically; therefore, a simple addition of all the spins should correspond to the observed value of **M** at very low temperatures. Now $|\mathbf{M}| = \mu_B g n$ at T=0 where μ_B is the Bohr magneton, g is the average g_B for Mn^{4+} and Mn^{3+} ions weighted by their concentrations ($g = g_B [x S_{Mn^{4+}} + (1-x) S_{Mn^{3+}}]$), and n is the volume density of the manganese atoms. From Hund's rule, Mn^{4+} is in $^4F_{3/2}$ state and Mn^{3+} is in $^5D_0$ state. Therefore, $S_{Mn^{4+}} = 3/2$ and $S_{Mn^{3+}} = 2$. Putting everything together for the sample of figure 3.2, the calculated value of **M** at T=0 is 83 emu/g, which is in very good agreement with the observed value. The inset of figure 3.2 shows the inverse of the magnetization. Also shown in the inset is extrapolation of the linear paramagnetic high-temperature region that crosses the x-axis at ~ 240 K, which defines the Curie temperature. Another peculiarity in the magnetic properties of the manganites is the behavior of the inverse of the magnetic susceptibility at temperatures very close to T_c. In particular, χ^{-1} shows a negative curvature just before it drops to zero from above T_c[17] (see figure 1.3). In contrast, $SrRuO_3$, which also undergoes a ferromagnetic transition, does not show any of the peculiarities associated with the manganites; it behaves like a classical ferromagnet[28]. Note that $SrRuO_3$ is not a manganite, but does have a perovskite structure.

For illustrative purposes, the magnetization[21] of a single crystal of $La_{0.6}Pb_{0.4}MnO_3$ is shown in figure 3.3. The inset to the figure shows the behavior of **M** as a function of the applied magnetic field. No saturation has been reached at high-temperatures even at ~ 6 Tesla.

3.2 Transport

The electronic transport of the perovskite manganites in the ferromagnetic range ($0.20<x<0.50$) is highly unusual. The resistivity ρ (T) shows what looks like a semiconducting state for temperatures above the Curie temperature. Upon cooling from above the Curie temperature there is a sharp drop in resistivity as the magnetization sets in at T_c. This results in a large peak in ρ (T) in the crossover regime. Below T_c the material behaves like a metal, i.e. the resistivity decreases with the temperature. Figure 3.4 shows the resistivity of a single crystal sample of $Nd_{0.6}(Sr_{0.7}Pb_{0.33})_{0.4}MnO_3$ grown in the Zettl lab, and superimposed on it is the magnetization data for the same sample, both as functions of temperature. The Curie temperature for this sample is ~240 K and, as can be seen, the peak in resistivity is very close to this temperature. Therefore, the peak of ρ(T) very closely, not to mention conveniently, follows and measures the Curie temperature.

The functional form of ρ(T) mimics an Arrhenius behavior ($\rho \sim e^{\Delta/T}$) above T_c. In fact many authors have claimed this to be the case[29] and have extracted activation energies of the order of 0.1 eV (~1200 K) by fitting the resistivity data above T_c to an Arrhenius form. The actual fitted data are hardly ever published to be judged by the reader.

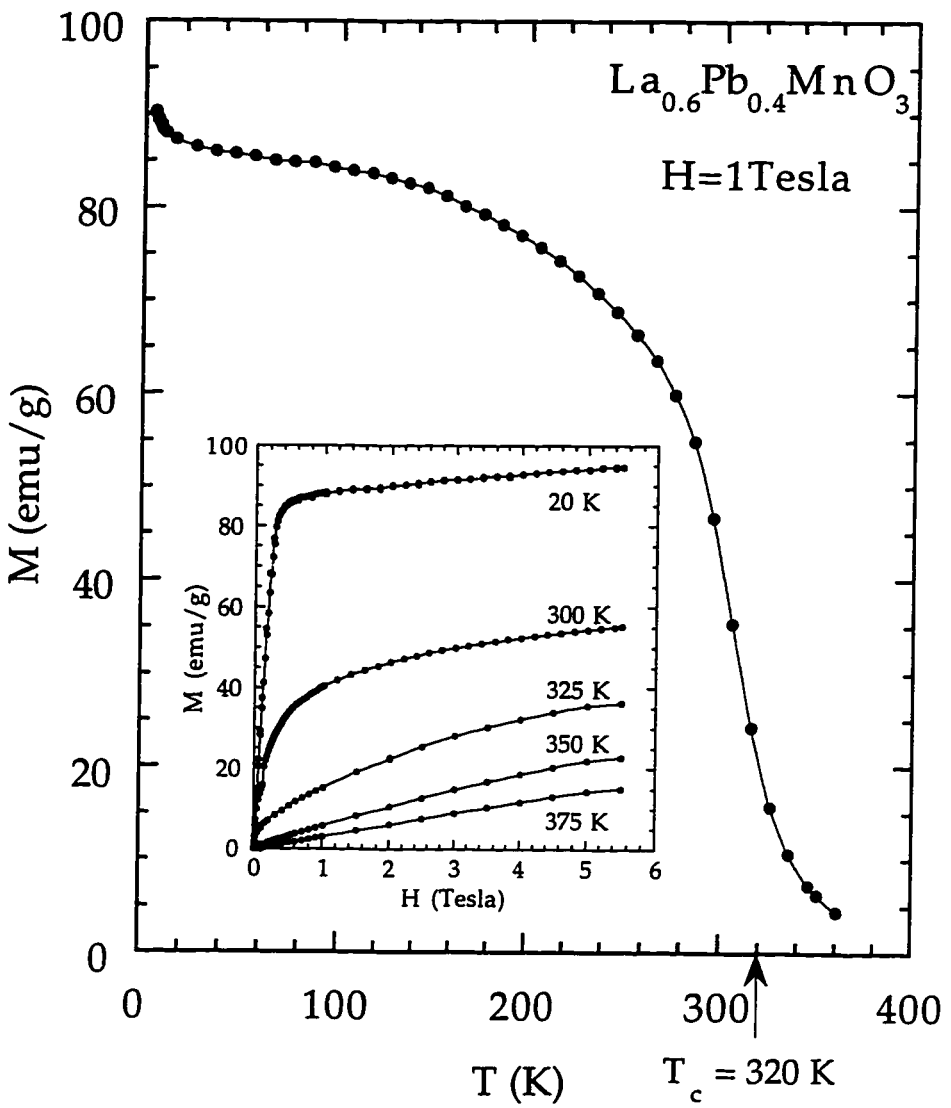

Figure 3.3. Magnetization of single crystal $La_{0.6}Pb_{0.4}MnO_3$ (measurement performed by Y. X. Jia[21]). The inset shows the behavior of magnetization as a function of the applied magnetic field.

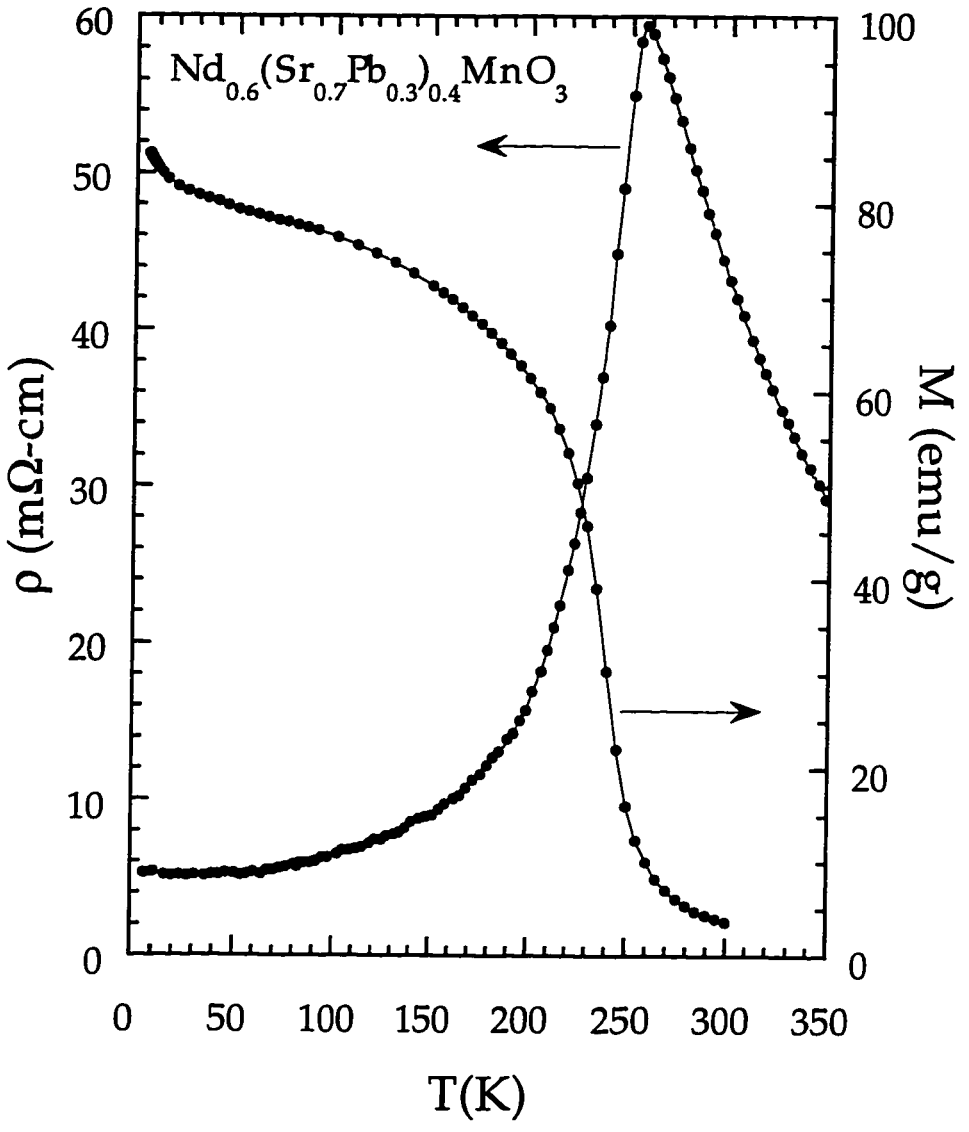

Figure 3.4. The resistivity and the magnetization of single crystal $Nd_{0.6}(Sr_{0.7}Pb_{0.33})_{0.4}MnO_3$ (measurement performed by Y. X. Jia[21])

In all of the studies done in this laboratory[21,30,31,32], on polycrystalline samples as well as on single crystals, it was found that above T_c the resistivity *can* be fit to an Arrhenius form *but* the fit is not as good as a fit to a variable-range hopping (VRH) form. This behavior has also been reported by at least one other group[33]. Variable-range hopping of the carriers happens in a system with a relatively high degree of disorder, e.g. in non-crystalline materials. The resistivity in such system has the following temperature dependence[34]

$$\rho = \rho_0 e^{\left(\frac{T_0}{T}\right)^{\frac{1}{4}}} \qquad \text{eq. 3.5}$$

where T_0 and ρ_0 are constants. Although the samples studied here usually have a high order of crystallinity, the source of disorder might come from ionic spins and other sources which will be discussed later in section 3.5. Figure 3.5 shows the resistivity of a single crystal sample of $Nd_{0.57}Pb_{0.39}MnO_3$ (measurement performed by Li Lu[32]). It can be seen in the upper inset that the VRH model fits the data extremely well. The lower inset to figure 3.5 shows the same data fitted to an Arrhenius (activated) form. Notice the inferiority of the activated fit compared to the VRH fit. It should be mentioned that not all the samples show VRH behavior, but such samples don't show an activated behavior either. The samples with the sharpest transition to the metallic state, which indicates a uniform high purity sample, show VRH above T_c.

In the metallic region (below T_c), the ferromagnetic manganites don't follow any conventional functional form. To date, no extensive theoretical study has

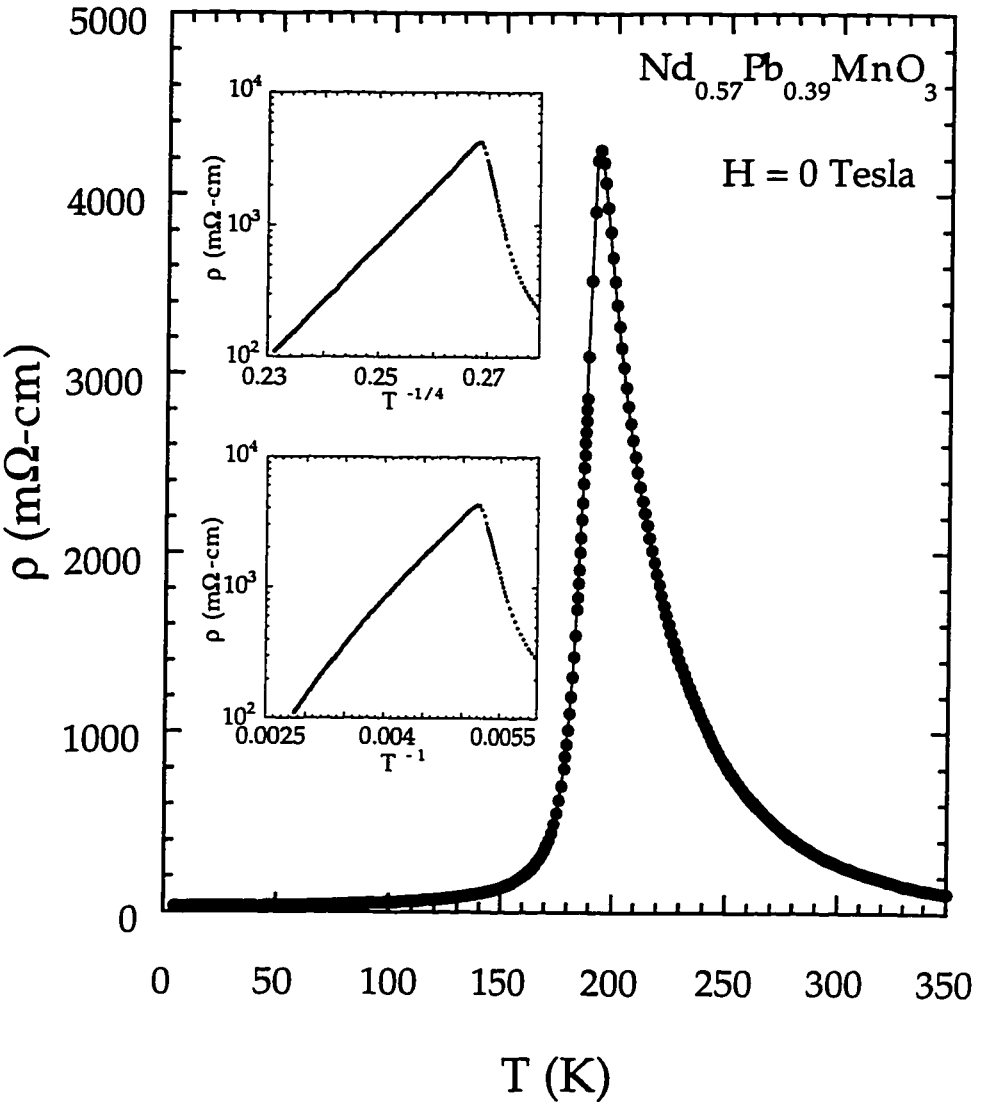

Figure 3.5. Resistivity of $Nd_{0.57}Pb_{0.39}MnO_3$ as a function of temperature (measurement performed by Li Lu[32]). The insets show the behavior of resistivity at temperatures above T_c.

attempted to describe the resistivity of the ferromagnetic manganites below T_c. Of course, the resistivity just below T_c is hard to handle theoretically due to the ferromagnetic fluctuations. However, these fluctuations are very small at temperatures below $0.5T_c$ (see figures 3.2 and 3.3) where the ferromagnetic order is fairly complete. From the experimental data[35], $\rho(T)$ has the following functional form at low temperatures

$$\rho(T) = \rho_1 + \rho_2 T^{\gamma} \qquad \text{eq. 3.5}$$

where ρ_1 and ρ_2 are temperature-independent factors and $\gamma \sim 2.5$. This empirical fit to $\rho(T)$ should represent a combination of electron-electron, electron-phonon, and electron-magnon scattering contributions. There is a slight upturn in $\rho(T)$ at very low temperatures (below ~25 K) which is seen in most samples of these materials[21,30]. Figure 3.6 shows such a upturn in $Nd_{0.6}(Sr_{0.7}Pb_{0.33})_{0.4}MnO_3$. This upturn is interpreted as reentrance into the activated behavior seen for temperatures above T_c. This will be discussed later in section 3.5.

One last important note is that the resistivity of the manganites in the metallic region can, depending on the dopants[33], violate the Ioffe-Regal limit. The Ioffe-Regal limit puts an upper bound on the resistivity of metals by arguing that the mean free path of the carriers can't be less than the lattice parameter a. Using the free electron model, the Ioffe-Regal limit is

$$\rho_L = \frac{h}{e^2 a}\left(\frac{3}{8\pi n^2}\right)^{\frac{1}{3}} \qquad \text{eq. 3.6}$$

which, with $n = 4.5 \times 10^{27}$ m^{-3} and $a = 3.8$ Å for manganites[33], gives the value of ~1

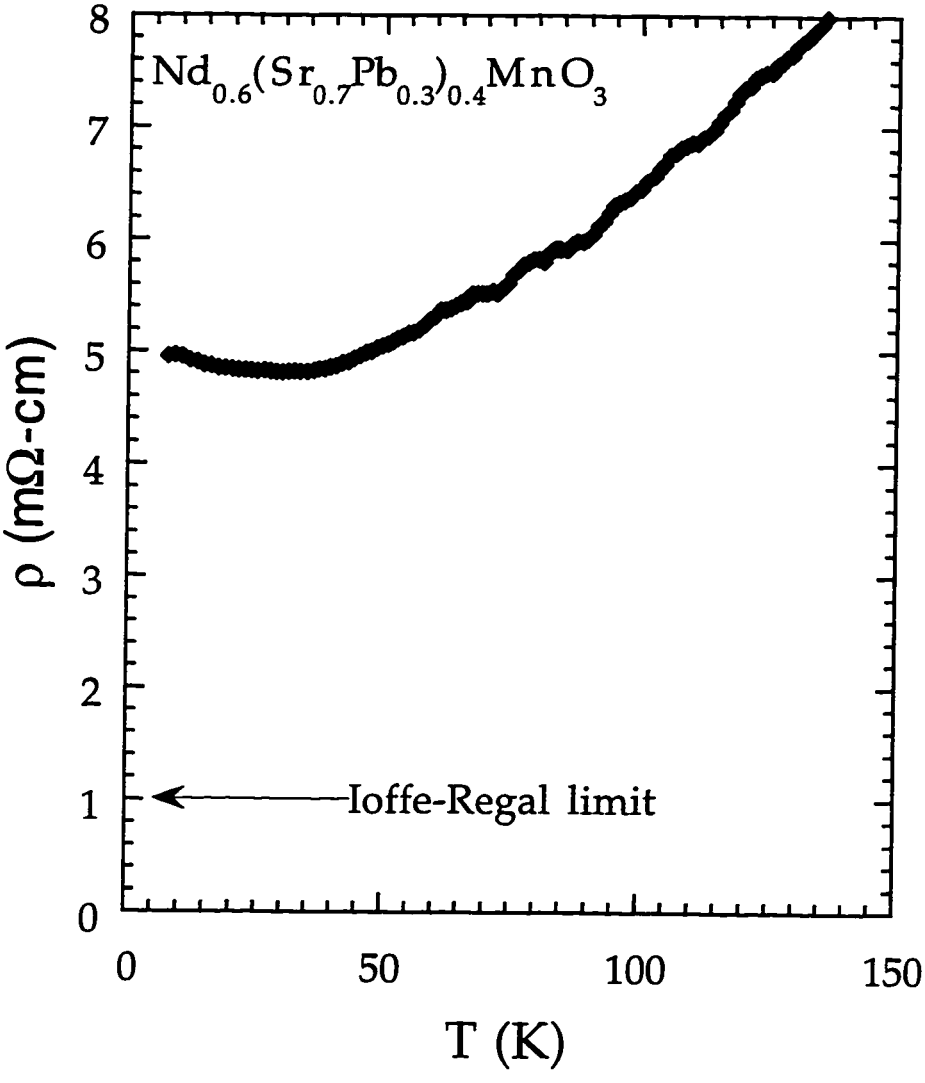

Figure 3.6. The resistivity upturn at very low temperatures in $Nd_{0.6}(Sr_{0.7}Pb_{0.33})_{0.4}MnO_3$. Notice that the Ioffe-Regal limit is violated even at the lowest temperatures.

mΩ-cm. This is clearly violated for the Pb doped samples grown in this lab, even at the lowest temperatures, as seen in figure 3.6.

3.3 Magneto-transport

The mixed-valence perovskite manganites in the range $0.2<x<0.5$ display a remarkably large negative magnetoresistance (MR); hence, they have been called the colossal magnetoresistance (CMR) materials to distinguish them from the GMR materials[36,37,38], the giant magnetoresistance magnetic multilayers. The magnetoresistance of the mixed-valence manganites is *negative*, i.e. their resistivity decreases under an applied magnetic field. The magnitude of this change is so large that the conventional definition of the MR,

$$\frac{\rho(H)-\rho(0)}{\rho(0)} \qquad \text{eq. 3.5}$$

becomes obsolete in the sense that it becomes difficult to distinguish between two samples with the MR values very close to 1, for example 99% and 99.99 %. Therefore, the denominator in equation 3.5 is replaced with $\rho(H)$ to make the ratio large (eq. 1.2).

Figure 3.7 shows the resistivity and magnetoresistance of a single crystal sample of $Nd_{0.62}Pb_{0.30}MnO_{3-\delta}$ in zero and in 7 Tesla applied magnetic field, both as functions of temperature. The resistivity drops by a factor of ~16 at T_c under application of a 7 Tesla magnetic field. The magnitude of the MR increases as the temperature is lowered from above T_c it reaches its maximum at T_c and then decreases with the temperature. The maximum magnitude of the MR is around 1600% which corresponds to 94% in the conventional definition (eq. 3.5). The MR

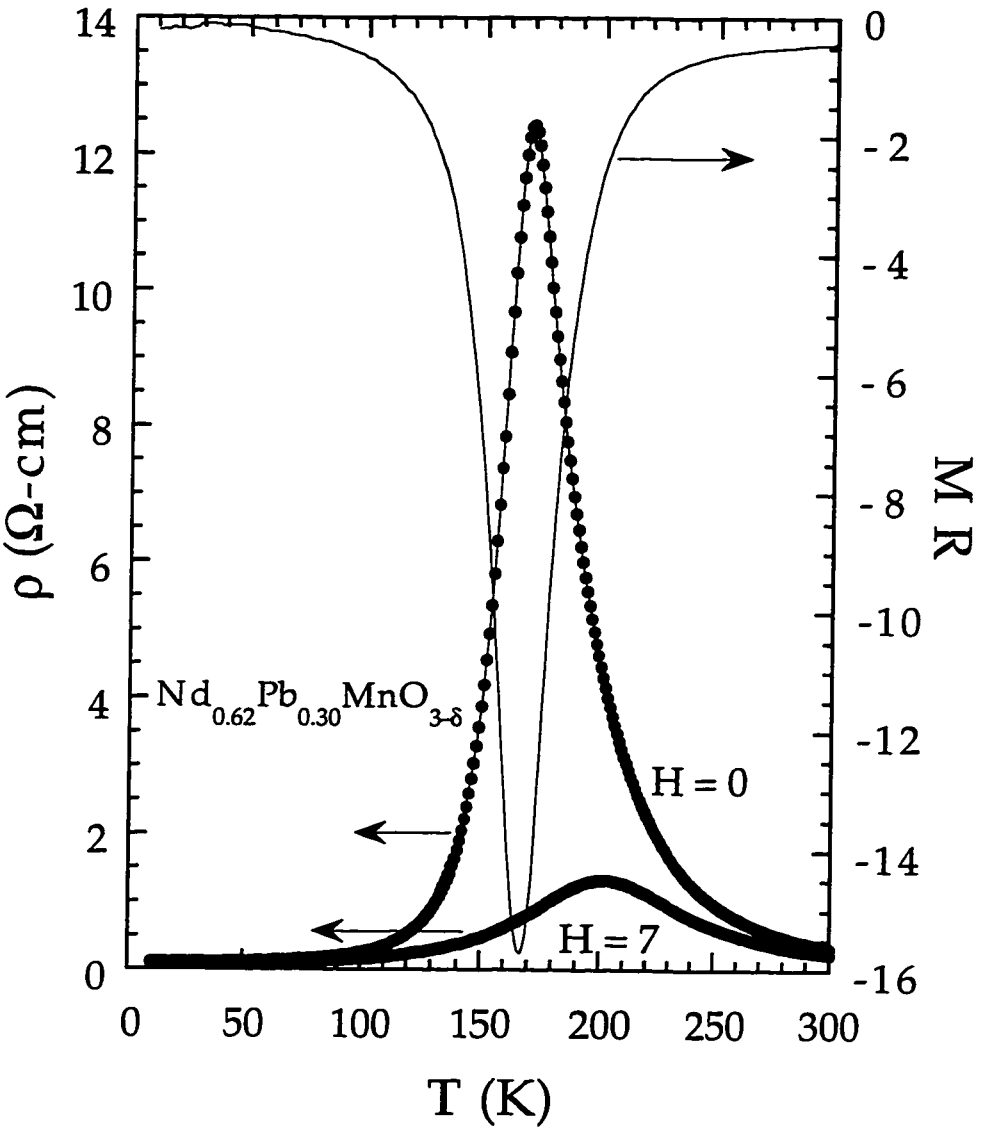

Figure 3.7. Resistivity and MR (max.~1600%) of $Nd_{0.62}Pb_{0.30}MnO_{3-\delta}$ at zero and at 7 Tesla applied magnetic field. Notice that the minimum of MR is at T_c.

goes to zero as T --> 0. This behavior is seen in single crystals[21] and in epitaxial thin films[2,29], but there is a substantial MR even at the lowest temperatures in polycrystalline samples[30,35]. This can be attributed to the grain-boundary scattering processes present only in polycrystalline samples.

The behavior of $\rho(H)$ is also interesting. Figure 3.8 shows the resistivity of $Nd_{0.62}Pb_{0.30}MnO_{3-\delta}$ as a function of the applied magnetic field. The resistivity drops with a finite large negative slope at H=0 for temperatures below T_c and drops with zero slope at H=0 for temperatures above T_c. Notice that the resistivity has not reached any saturation value at least up to 7 Tesla; therefore, larger applied magnetic fields produce larger values of MR.

3.4 Universal behavior of the magnitude of the magnetoresistance

The absolute value of the maximum MR (which happens at or very close to T_c) in the mixed-valence perovskite manganites in the range $0.2<x<0.5$ follows a universal trend as a function of T_c. Figure 3.9 shows a compilation of published results for the maximum MR versus T_c for a variety of $A_{1-x}B_xMnO_{3-\delta}$ materials at fields ranging from 5 to 12 Tesla[2,17,29,39]. Considering the variations in materials and field strengths, a surprisingly robust inverse relationship between T_c and maximum MR is observed. The maximum MR at a given field appears to be a universal function of the transition temperature from the insulating to the metallic phase, which is very close to T_c. This trend can be qualitatively explained by looking at simple phenomenological forms for the low- and high-temperature

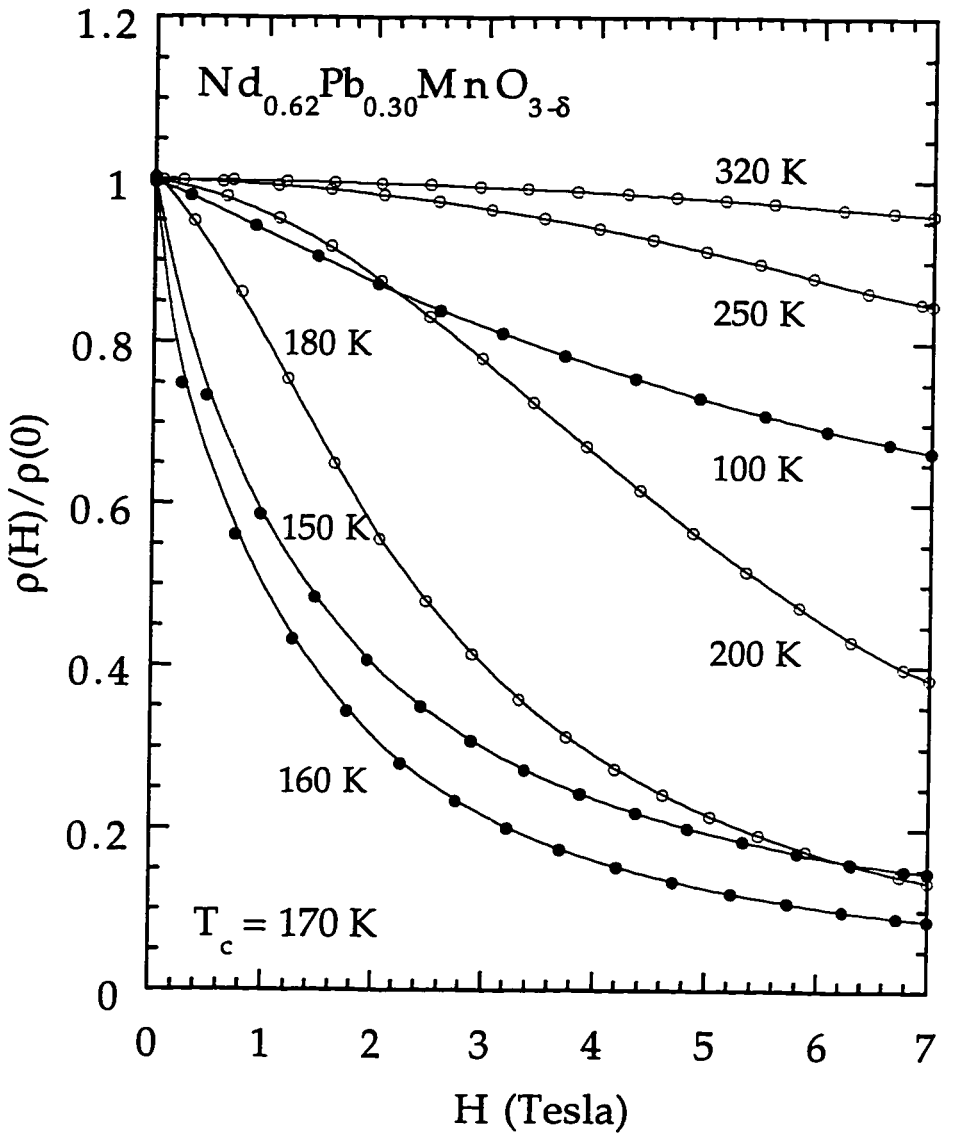

Figure 3.8. The normalized resistivity of $Nd_{0.62}Pb_{0.30}MnO_{3-\delta}$ as a function of the applied magnetic field. Solid circles indicate the data points for temperatures below T_c. Empty circles show the data points for temperatures larger than T_c.

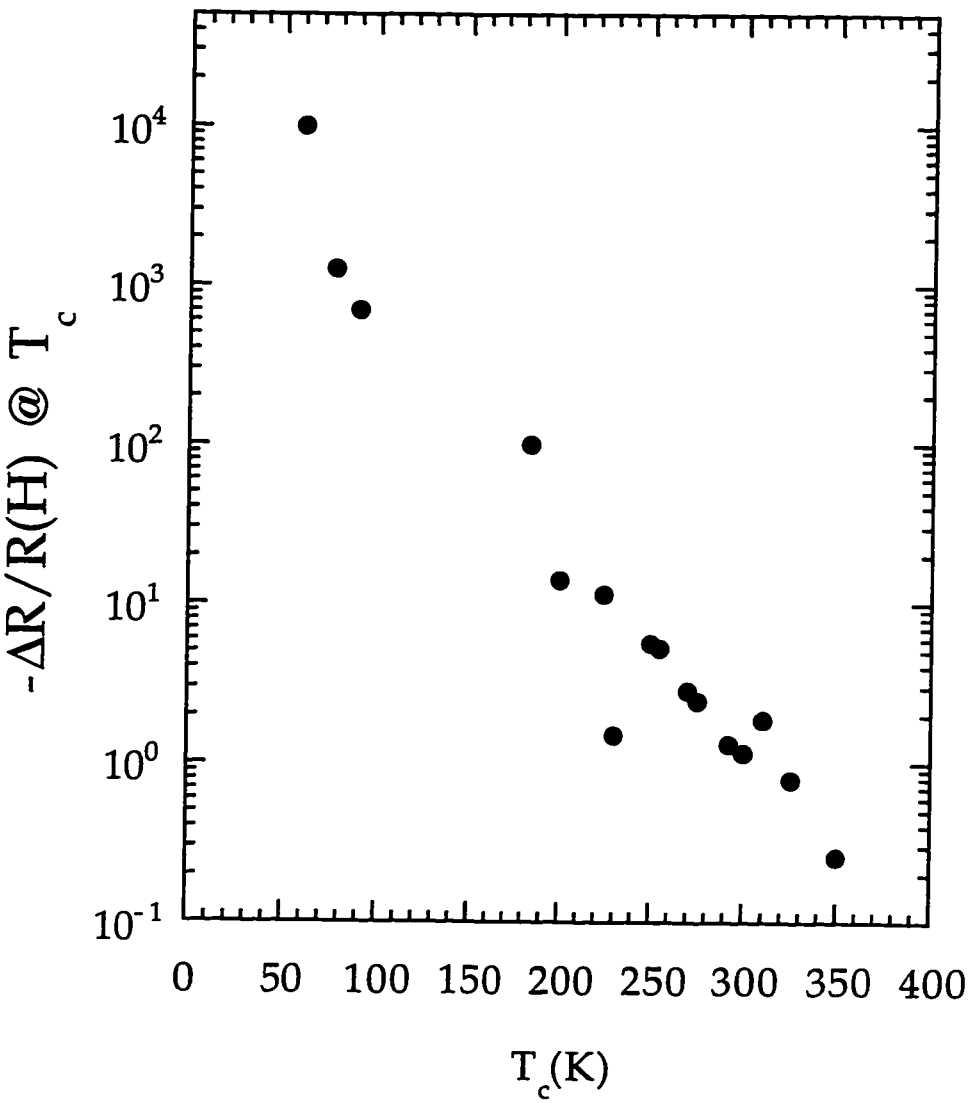

Figure 3.9. Compiled maximum MR vs. T_c from published data.

resistivities[31]. Taking the empirical expressions $\rho(T) = \rho_1 + \rho_2 T^{2.5}$ (eq. 3.5) for the low-temperature phase and $\rho = \rho_0 e^{\left(\frac{T_0}{T}\right)^{\frac{1}{4}}}$ for the high-temperature phase, and assuming that the magnetic field is large enough to induce a complete transition from the insulating to the metallic phase at the temperature of maximum MR, one obtains a maximum MR at T_{MI} of

$$MR_{max} \sim \frac{\left(\rho_0 e^{\left(\frac{T_0}{T_{MI}}\right)^{\frac{1}{4}}} - \rho_1 - \rho_2 T_{MI}^{2.5}\right)}{\rho_1 + \rho_2 T_{MI}^{2.5}} \qquad \text{eq. 3.6}$$

High-temperature activated conduction creates the divergence as $T_{MI} \rightarrow 0$. The MR at high-temperature disappears near a temperature at which the metallic-like resistivity exceeds the activated resistivity.

3.5 Theory

After the pioneering work of Jonker and Van Santen[1] on the perovskite manganites in 1950, the simultaneous occurrence of ferromagnetism and metallic conductivity was explained by C. Zener through a process he named *double exchange*[11]. Jonker and Van Santen had already speculated that the good electrical conductivity in the range $0.20<x<0.50$ is due to the transfer of electrons between the Mn^{3+} and Mn^{4+} ions. As it was shown in chapter 1, this transfer of electrons is not easily achieved since there is an oxygen between every pair of manganese atoms. This is why C. Zener presented the double exchange theory which can be

visualized as follows. Consider two manganese ions separated by an oxygen ion in a linear chain. The transfer of an electron from one Mn^{3+} ion to the adjacent Mn^{4+} ion is thought of as the transfer of an electron from the Mn^{3+} to the central oxygen ion simultaneously with the transfer of an electron from the central oxygen ion to the Mn^{4+} ion; hence the name double exchange. Within this model, the interaction is nonzero only if the spins of the adjacent manganese ions point in the same direction. In fact the transfer integral for this process is $t(\Theta) = t_0 \cos(\Theta/2)$, where Θ is the angle between neighboring manganese ion spins and t_0 is the angle-independent transfer integral[10]. The theory already explains the simultaneous occurrence of ferromagnetism and metallic conductivity: alignment of the spins of adjacent manganese ions is accompanied by an increase in electronic mobility and hence by an increase in the electrical conductivity.

Let's look at the ionic states of Mn^{4+} and Mn^{3+} in compounds $A_{1-x}B_xMnO_3$. It was already mentioned in chapter 1 that x is also the concentration of Mn^{4+}. At $x = 1$, all of the manganese ions are in the Mn^{4+} ionic state with the atomic configuration $3d^3$. All three electrons in this configuration occupy the lower energy d_{xy}, d_{xz}, and d_{yz} orbitals (with t_{2g} symmetry). These orbitals would be degenerate with d_{x2-y2} and d_{3z2-r2} orbitals (with e_g symmetry) if the manganese ion were in free space. But in a cubic environment the crystal field removes this degeneracy. According to the Hund's rule, the total spin of the Mn^{4+} ion is 3/2 (in units of $h/2\pi$). This series ($x = 1$) of manganese perovskites comprises cubic antiferromagnetic insulators.

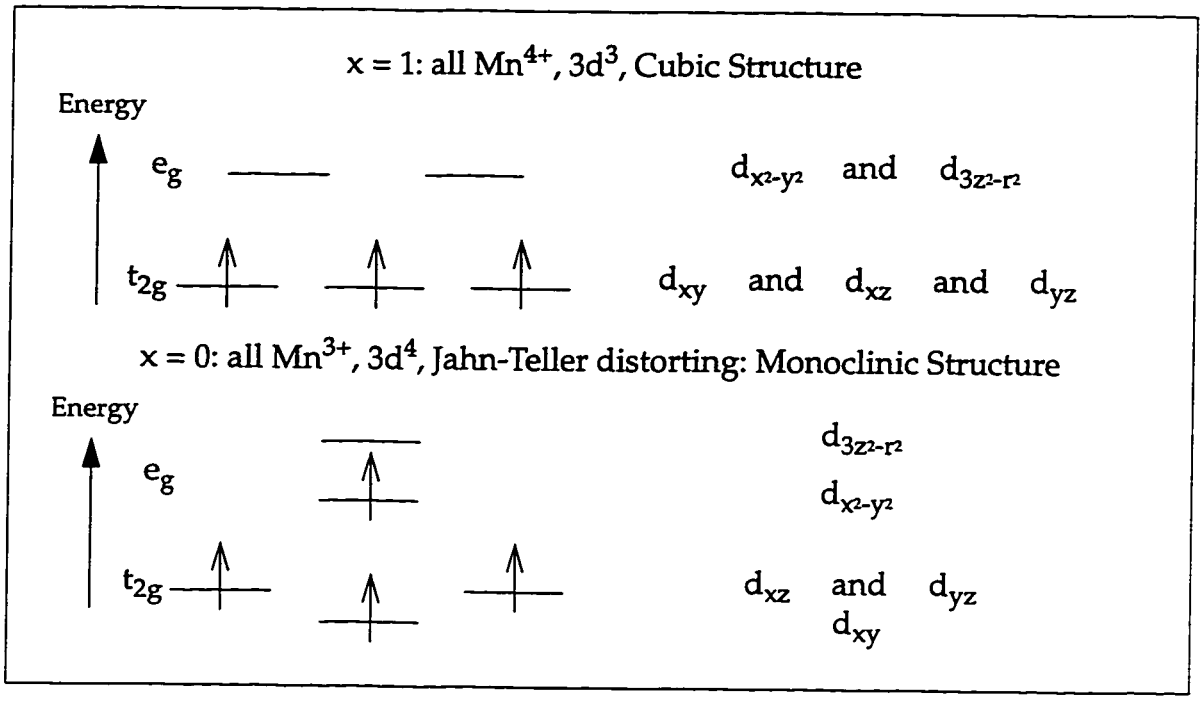

Figure 3.10. Valence energy diagrams of Mn^{4+} and Mn^{3+} ions in the end members of the compounds $A_{1-x}B_xMnO_3$.

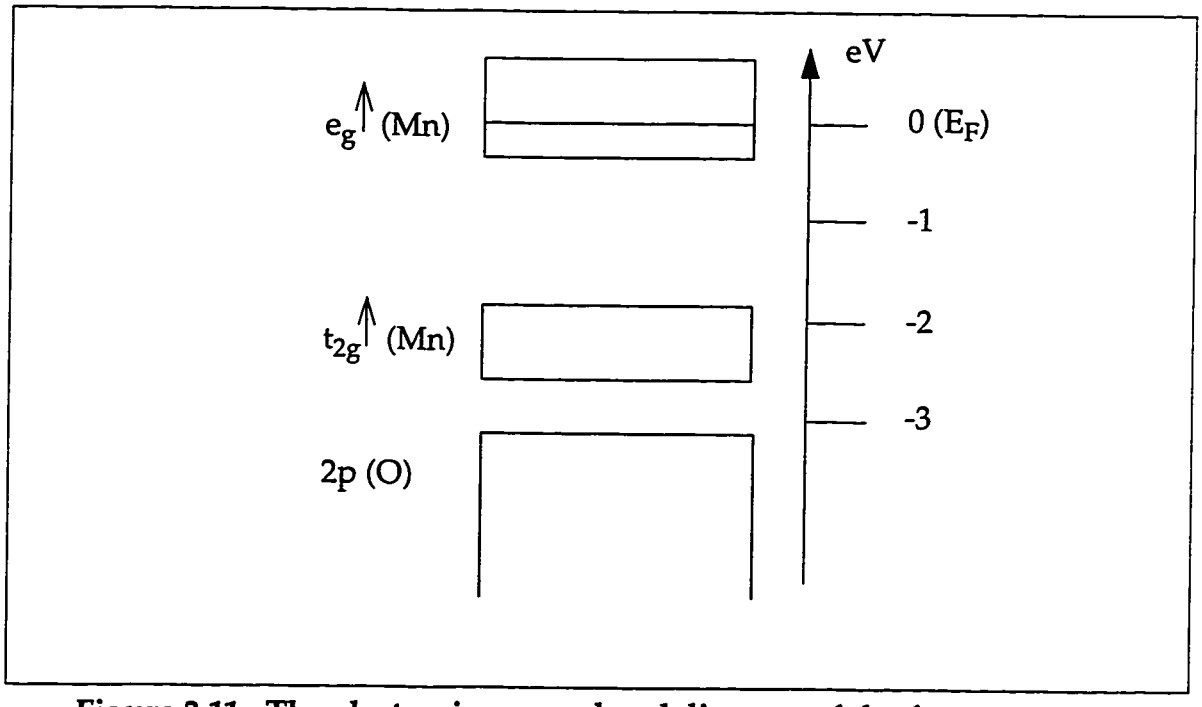

Figure 3.11. The electronic energy band diagram of the ferromagnetic manganites[33].

At the other end of the spectrum, we have the compounds with x = 0, where all of the manganese ions are in the Mn^{3+} ionic state with S = 2. But Mn^{3+} is a strong Jahn-Teller distorting ion[40]; therefore, the oxygen octahedrons containing the Mn^{3+} ions distort in real space[41] to remove the degeneracies of the d_{x2-y2} and d_{3z2-r2} orbitals and the d_{xy}, d_{xz}, and d_{yz} orbitals. The extra electron in Mn^{3+} occupies the d_{x2-y2} orbital which is now lower in energy than the d_{3z2-r2} orbital. This series (x =0) of manganese perovskites comprises monoclinic antiferromagntic insulators. The above ideas are schematically shown in figure 3.10.

In the intermediate range (0.20<x<0.50) the structure of the perovskite manganites is very close to cubic (orthorhombic in some cases) and the materials are ferromagnetic metals below T_c. The electronic structure[33] of the ferromagnetic manganites is illustrated in figure 3.11. The e_g states form a band of about 1 eV wide and the t_{2g}-e_g separation is about 1.5 eV. The Fermi level is 3.0 eV above the top of the 2p(O) band. The Mn^{3+} charge state in this range is mobile and so the Jahn-Teller distortion follows its motion throughout the crystal. This so-called dynamic Jahn-Teller distortion has been confirmed experimentally by NMR measurements[42]. Dynamic Jahn-Teller distortion can be thought of as a strong electron-phonon coupling[43]. In a picture developed by Vincent H. Crespi and Marvin L. Cohen[32], at temperatures above T_c the spins of the manganese ions are randomly distributed since the material is in the paramagnetic state. Therefore the conduction band electrons hop from one site to another at a low rate due to the Hund coupling (Hund's rule). These slow electrons are then self- trapped due

to the Jahn-Teller effect, or equivalently the strong electron-phonon coupling, forming small lattice polarons (spin induced lattice polarons). These small lattice polarons undergo variable range or activated hopping thereby giving rise to the observed behavior of the resistivity at temperatures above T_c.

Below T_c, the spins of the manganese ions are more or less aligned and therefore the Hund's rule coupling is not an obstacle to electronic hopping; hence, the activation energy Δ, decreases. As long as Δ is much less than kT the electronic hopping rate increases: the polaronic conduction disappear and metallic conduction occurs. At very low temperatures kT might become comparable to Δ and so the activated behavior reappear at low temperatures as seen in figure 3.6. These ideas are schematically shown in figure 3.12.

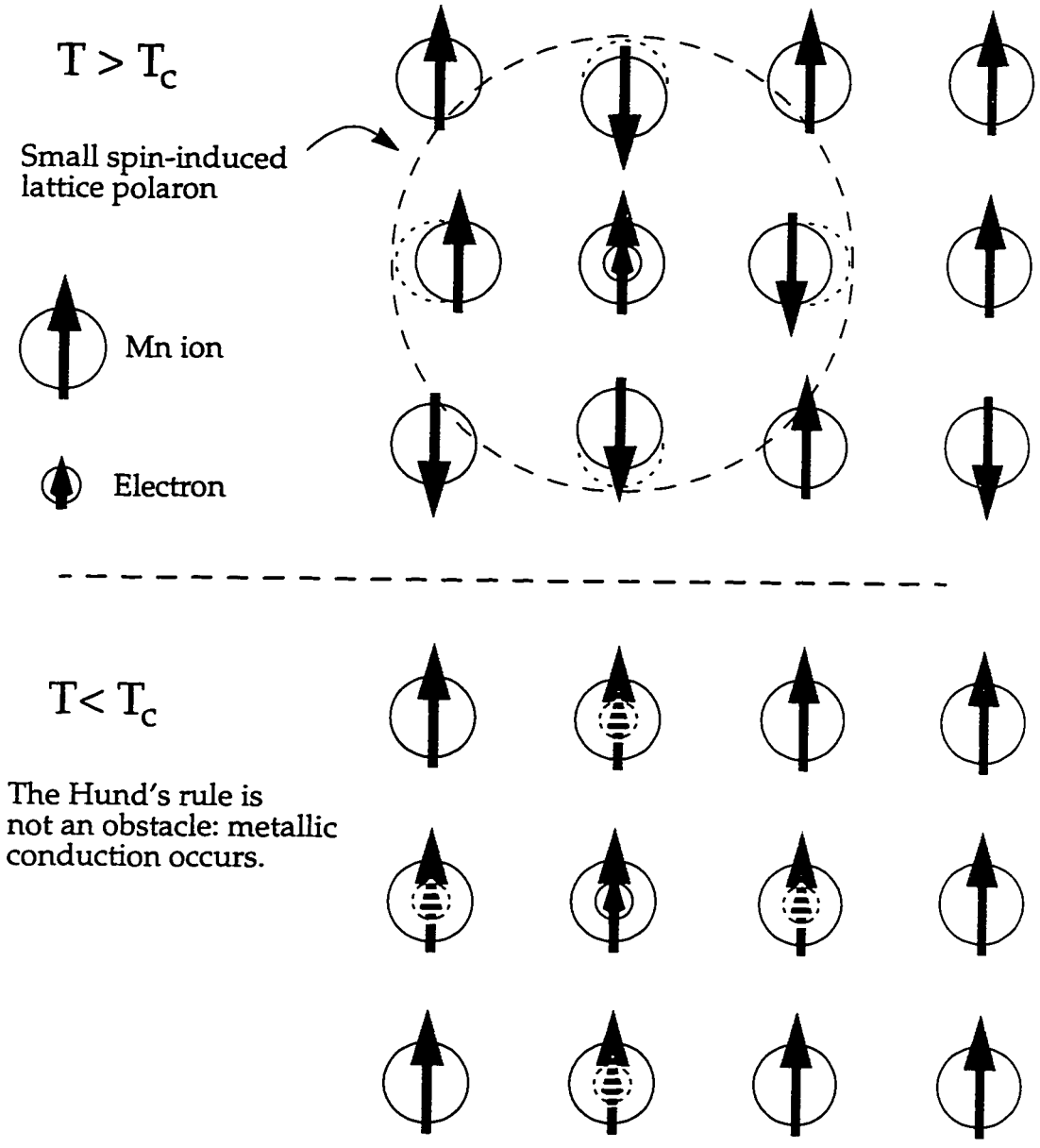

Figure 3.12. The formation of spin-induced small lattice polarons for $T>T_c$ due to Jahn-Teller effect. Below T_c the polarons cannot form (after V. H. Crespi).

Chapter 4

Transport measurement techniques under pressure

4.1 Pressure cells

High pressure experiments have long been of great interest to researchers in the fields of physics, geophysics, geology, material science and chemistry. Structural and electronic phase transitions can occur at high pressures in many solids and liquids. Some semiconductors such as CsI can undergo pressure-induced metallization at a pressure of about 1 Mbar[44]. Silicon becomes a metal and a superconductor at around 130 kbar.[45] There are two basic ways to produce high pressures: dynamic and static. In the most common dynamic approach a high-pressure shock wave is generated by impacting a high-speed projectile into a target containing the sample under investigation. The disadvantage of this method is that the experiment is destructive and its duration is extremely short (order 1 μs)[46]. On the other hand, in the static technique pressure can be maintained for a long time. In this method, either the sample is squeezed directly between flat faces of two or more anvils or the pressure is applied to the sample via a pressure medium. The static technique is the method used in this study.

There exist many pressure cell designs which achieve high static pressures. The two most widely used designs are the self-clamping cell and the diamond-anvil cell (DAC). There are also many DAC designs for different applications.

The Merrill-Basset cell[47] is a flat DAC for X-ray measurements under pressure. The piston-cylinder Mao-Bell[48] DAC is suitable for ultra high pressures. The design and application of the self-clamping piston-cylinder pressure cell used in this study is described in section 4.2. In section 4.3, the design of the piston-cylinder DAC used in the Zettl lab for ultra-high pressure resistivity measurements is described.

4.2 Self-clamping piston-cylinder pressure cell

The self-clamping pressure cell used in this study was built by Dr. Ian Parker[49]. This cell allows for measurements at up to ~20 kbar of hydrostatic pressure. The entire cell, except for a very small copper ring and a Teflon cap, is made of BeCu (Berylco 25) which has a hardness of c40-c45 on the Rockwell scale when heat treated for 2.5 hours at 320 C. Figure 4.1 shows the schematic of the cell, its components and the sample assembly. After it has been machined and heat treated, the body of the cell must further be hardened by a process called autofrettaging. This process involves pressurizing the cell with a lead plug until the outside diameter of the cell has swelled by 0.003 inches. The lead plug is then machined out and the inside diameter of the cell is reamed to the final size and honed smooth.

The sample is mounted on the sample mount, and suspended from four gold pins which allow the pressure medium to surround the sample. The experimental procedure is as follows. Four pieces of 2 mil gold wire, about 2 cm in length each, are attached to the sample (four-probe geometry) by small dabs of sil-

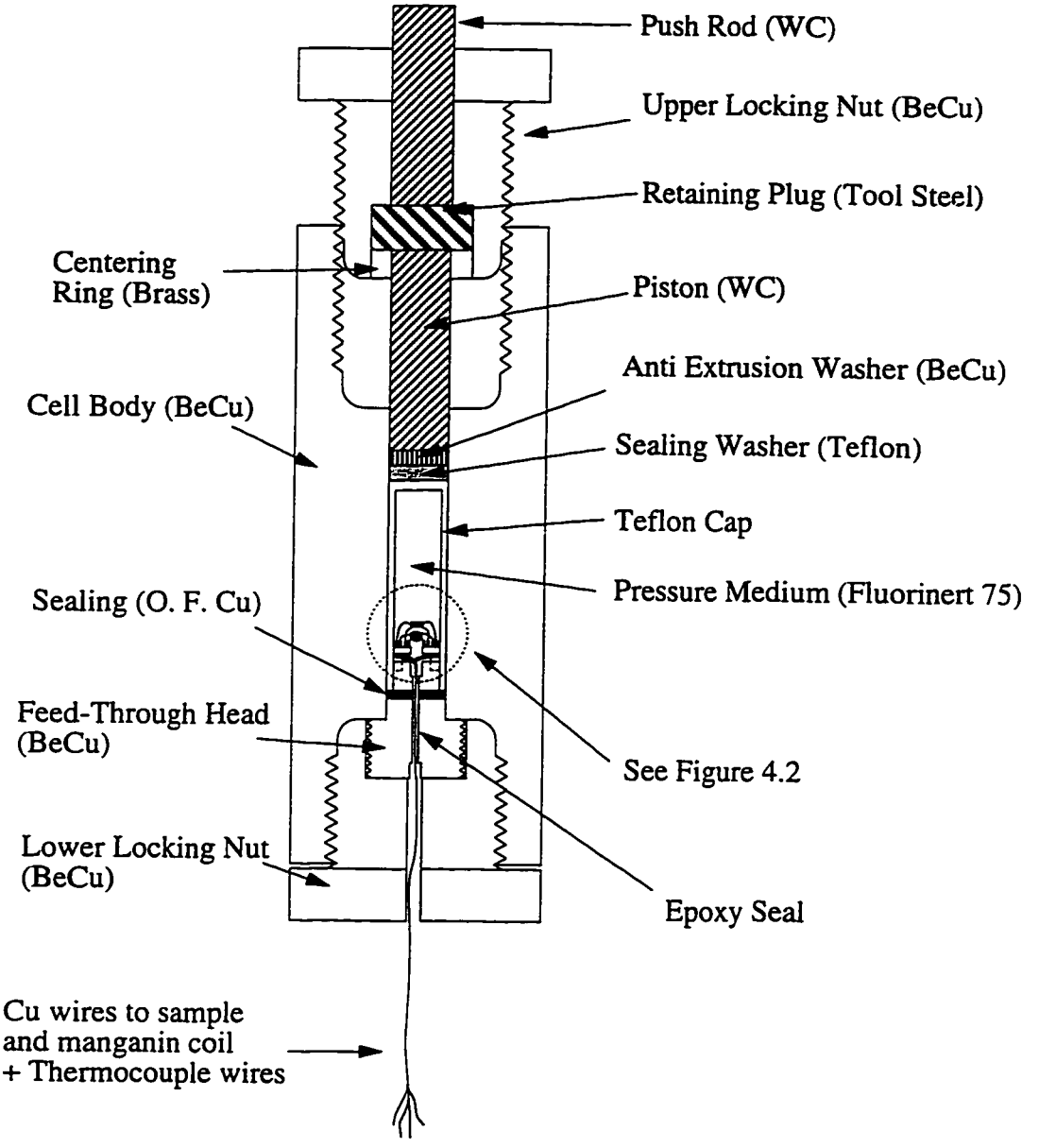

Figure 4.1. Schematic of the self-clamping pressure cell. The body of the cell is made of BeCu. The sample mount is made of G10.

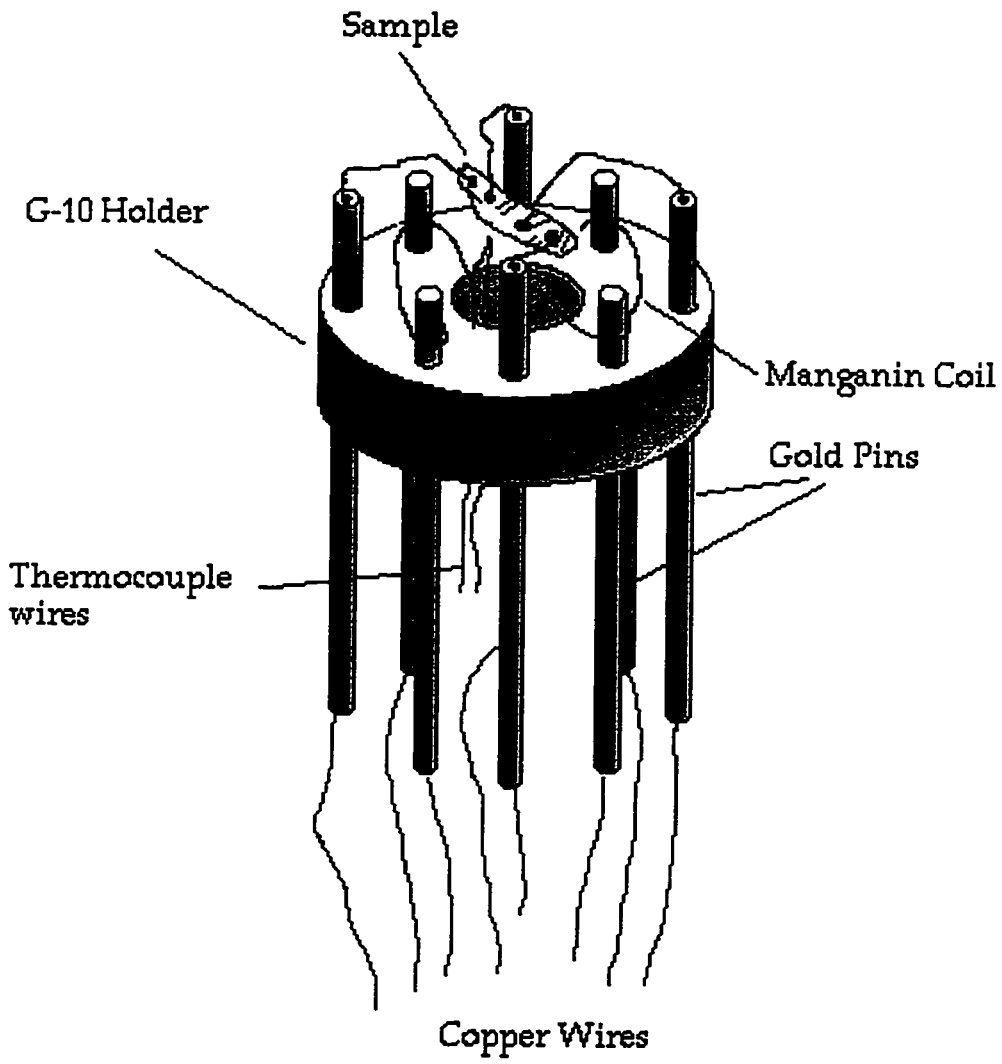

Figure 4.2. Schematic of the sample mount showing the sample, the manganin coil, and the gold pins. The body of the holder is made of G-10.

ver paint, and set aside to dry. This is done under a stereoscopic microscope on a glass slide (not on the sample mount). The sample mount is wired and attached to the feed-through head, and the assembly is placed under the microscope, held by its special holder[49]. After the silver paint is dried, the free end of one of the gold wires is picked up with a pointy tweezer. The sample is now at the other end of the gold wire, with three other gold wires attached to it. This wire is glued, using silver paint, to one of the gold pins on the sample-mount (see figure 4.2). Again, the silver paint should be allowed to set. Now the sample is in midair, in the middle of the sample mount (on top of the hole close to the thermocouple) with only one of the wires attached to one of the gold pins of the sample mount. The other wires are now carefully attached to the rest of the gold pins on the sample-mount.

The copper wires that come out from the other end of the feed-through head are bundled with heat-shrink tubing. This bundle is fed through the hole in the lower locking nut and gold-pinned plugs are soldered at their ends so that they can be plugged into the sockets on the low-temperature probe. The feed-through head can now sit inside the lower locking nut. A Teflon cap is filled with an appropriate pressure medium using an eye dropper. Note that the Teflon caps can only be used once. The pressure medium is usually a 1:1 mixture of two different alcohols (n-pentane and isopentane) but it was Fluorinert FC-75 (an inert electronic liquid made by 3M) for this study. A few drops of the pressure medium are poured on the sample. The Teflon cap containing the pressure medium is now ready to cap the sample. To do this, the feed-through head (now inside the lower

locking nut) should be held upside down and inserted into the teflon cap. One should not try to put the Teflon cap onto the feed through head as the pressure medium would obviously pour out of the Teflon cap. This step should be done with great care since many things can go wrong. For example, the sample could hit the edges of the Teflon cap and be destroyed, or the feed-through head could drop out of the lower locking nut destroying much more than just the sample.

After the Teflon cap has been placed on the sample, a focused light source is placed behind the cap and one visually inspects the inside of the cap for any possible trapped air bubbles. If any air bubbles are detected, the above procedure should be repeated again with the same Teflon cap (Teflon caps can only be used once *if* they have been used in an actual pressurization). The whole assembly of the Teflon cap, the feed-through head, and the lower locking nut is now in one piece. The body of the pressure cell is brought to this assembly, and the Teflon cap is carefully inserted into the hole inside the cell from the shorter threaded end. The lower locking nut is then tightened by a wrench (some WD-40 should be applied to the lower locking nut before tightening). From this point on, the procedure to pressurize the sample is simple and can be found in the pressure cell manual[49] in Zettl's lab.

The pressure inside the cell is measured and monitored by measuring the four probe resistivity of a calibrated manganin coil. The resistance of manganin wire varies linearly with pressure in the range $0<P<30$ kbar[50], and the typical value of the pressure coefficient of the resistance ($dlnR/dP$) is 2.4×10^{-3}. The pressure coefficient of the resistance is independent of the temperature[51] but the actual

value of the resistance does change with the temperature. The calibration of the manganin coil is as follows. The resistivity of the coil is measured as a function of pressure at room temperature using a previously calibrated manganin coil. This yields R(P,T=room) and in turn dlnR/dP. Then the resistivity of the coil is measured as a function of temperature at zero pressure. This yields R(P=0,T). The pressure inside the cell at any temperature is then given by[51]

$$P(T) = \left[\frac{R(P,T)}{R(P=0,T)} - 1\right]\left[\frac{\partial P}{\partial \ln R}\right] \qquad \text{eq. 4.1}$$

where R(P, T) is the value of the resistance of the manganin coil at pressure P and temperature T. Figure 4.3 shows a typical resistance vs. temperature for a manganin coil used for pressure measurement. The inset to figure 4.3 shows the resistance vs. pressure at room temperature. Notice that the slope of the resistivity vs. temperature is zero at temperatures close to room temperature.

The pressure inside the cell drops upon cooling. This is because the pressure medium contracts more than the cell does as the temperature is lowered. The amount of this decrease depends on the pressure medium used. In the case of Fluorinert FC-75, the pressure inside the cell drops about 3.5 kbar from its value at 300 K, roughly independent of the initial clamping pressure. The temperature inside the cell (next to the sample) is measured by a Chromel/Constantan thermocouple since a diode cannot be used inside the cell. It has been shown that the voltage of the Chromel/Constantan thermocouple is independent of pressure[52]. The procedure is as follows. A diode is heat-sunk to a block of copper just outside the cell. The thermocouple that comes out of the cell is also heat-sunk to the same

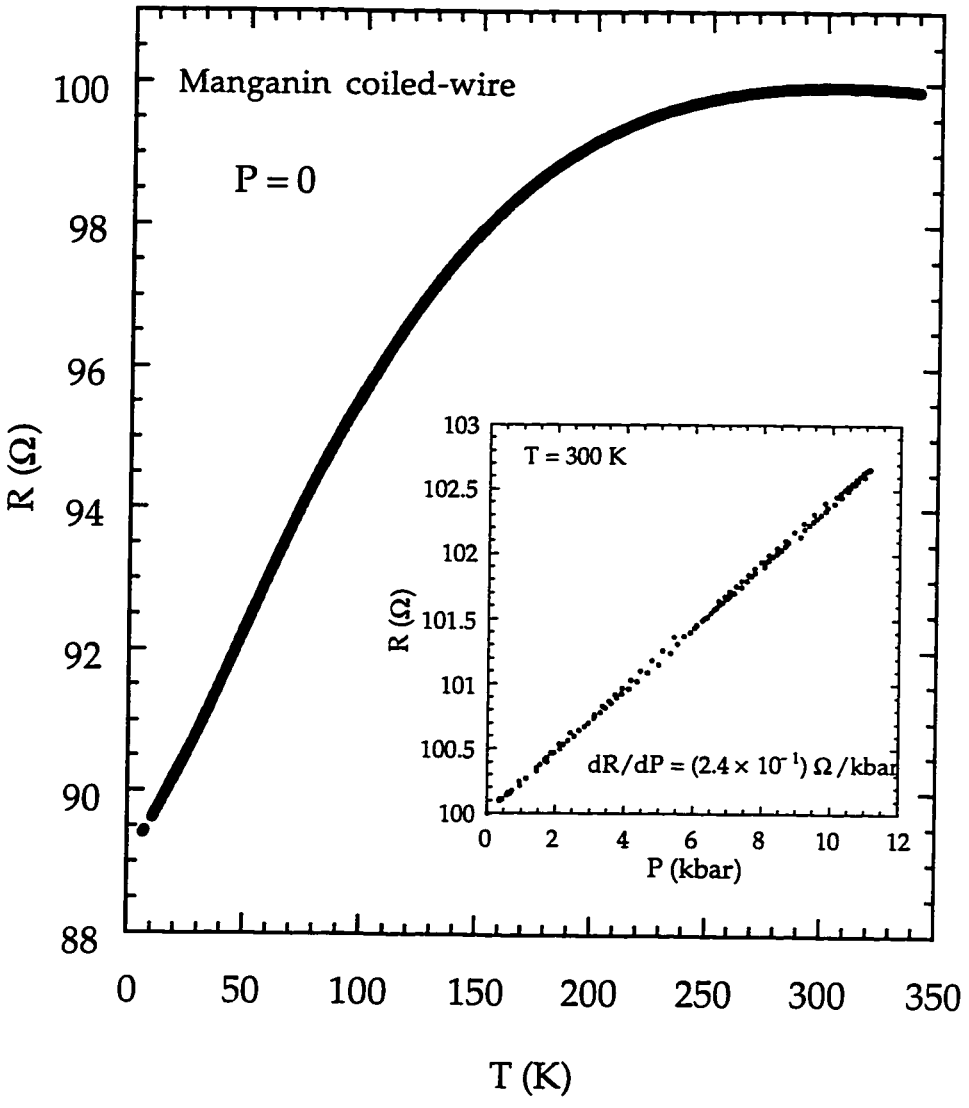

Figure 4.3. The plot of R vs. T for a typical manganin coil at zero pressure. The inset shows R vs. P for the same coil.

block. The temperature-sensing end of the thermocouple is inside the cell next to the sample. The temperature just outside the cell (temperature of the copper block) is measured using the diode. At the same time, the voltage across the thermocouple is measured. Using the thermocouple's calibration file, the temperature difference ΔT, between the inside of the cell and the copper block is calculated. This ΔT is then added to the measured temperature of the block (diode's measurement) to get the temperature inside of the cell next to the sample. All of the measurements presented in the following chapters have been performed with this pressure cell.

4.3 Piston-cylinder Diamond anvil cell

The piston-cylinder diamond anvil cell used in the Zettl lab was built by the author of this thesis and its design was motivated by the design of the DAC used in Peter Yu's laboratory at U.C. Berkeley. The entire DAC is made of beryllium copper. Figure 4.4 shows the schematic of the DAC, its components, and their sizes. All the components are heat-treated for maximum hardness (2.5 hours at 320 °C in flowing argon). The diamonds used in this DAC were purchased from Drukker International and are the Standard Design, type I diamonds. The diamonds are eight-sided and the distance between any two parallel sides of the resulting hexagon on the top flat part of the diamonds, the so-called culet size, is 0.5 mm. Usually, the diamonds are fixed to their backing by application of a good quality epoxy glue. The disadvantage of this method is that the diamonds can go out of alignment (explained later) after each pressurization since epoxy glue cannot support shear forces. By the same token, high-temperature measurements

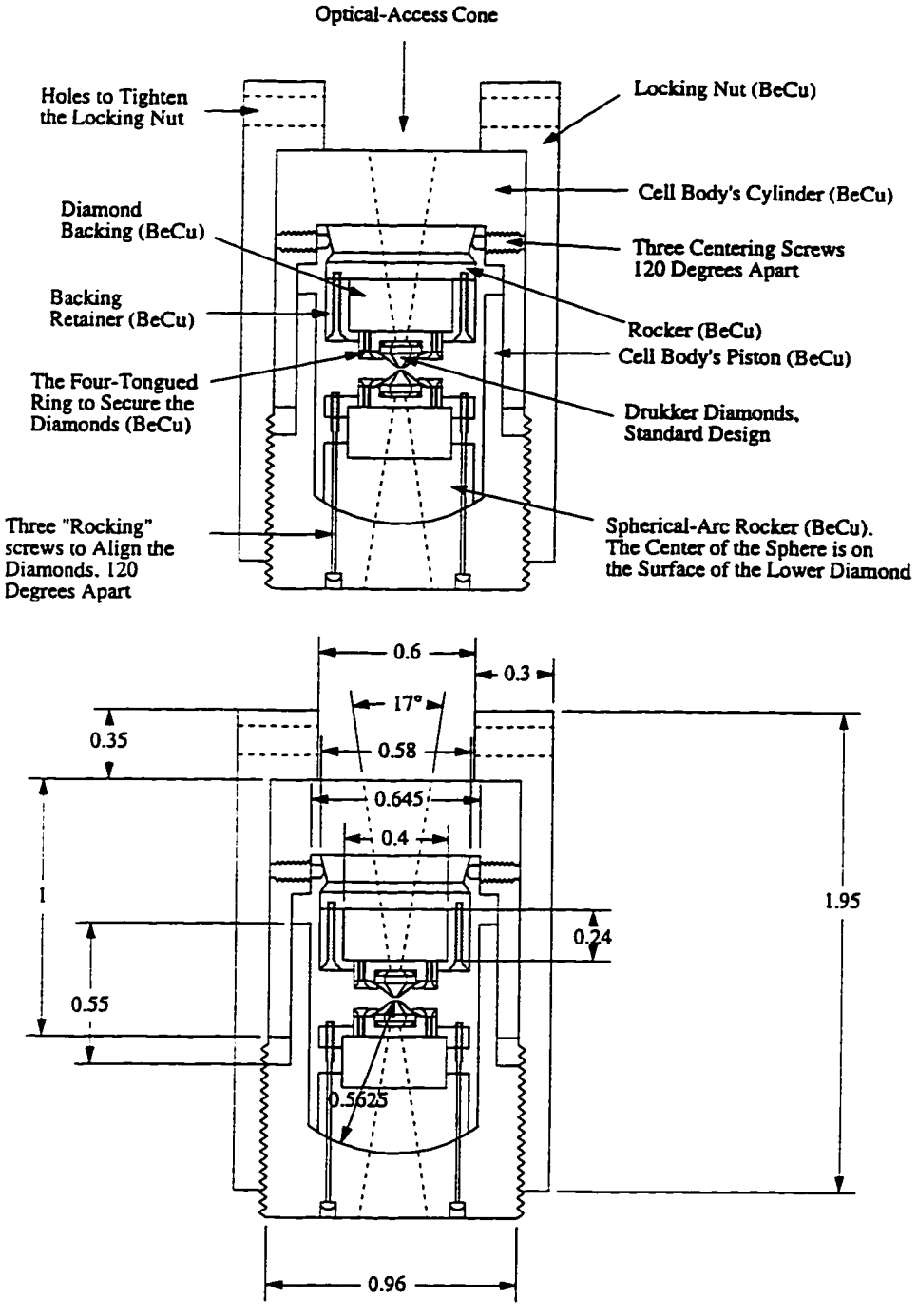

Figure 4.4. Technical drawings of the DAC used in the Zettl lab for transport measurements. The dimensions are in inches unless stated otherwise.

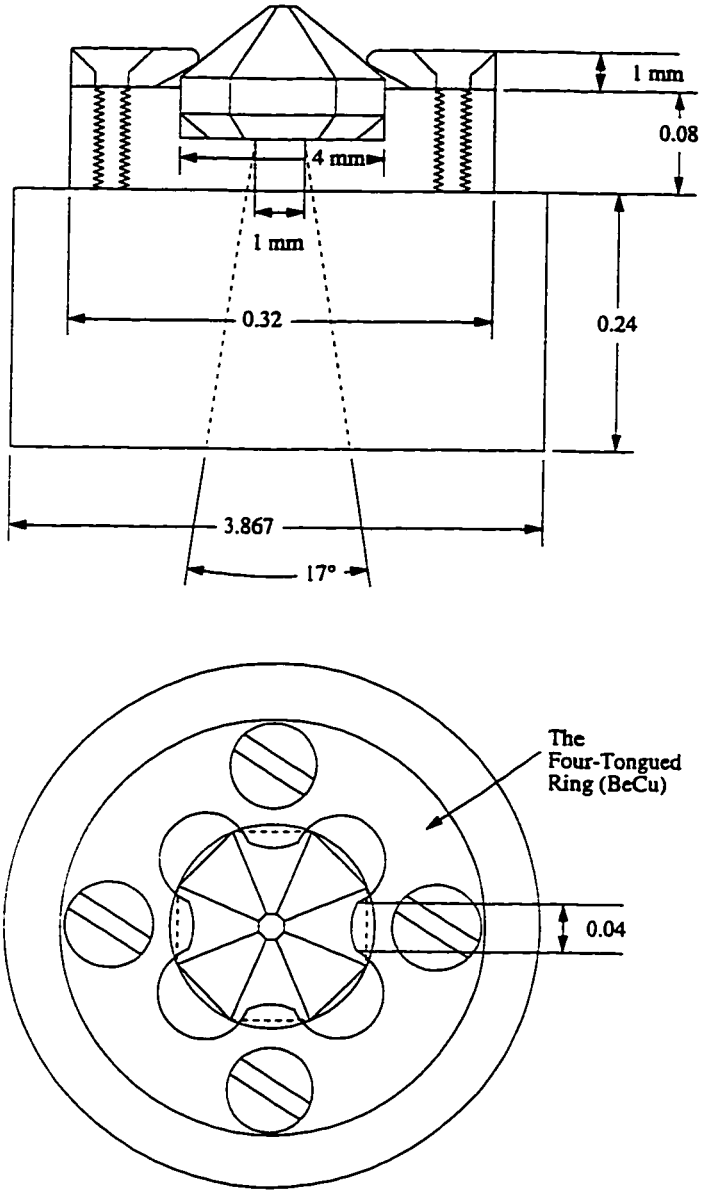

Figure 4.5. The four-tongued ring holding the diamond down by the springy action of the tongues after the screws are tightened. The dimensions are in inches unless stated otherwise.

cannot be easily done either.

In the DAC described here, a new method has been used to fix the diamonds down to their backing. This method uses a four-tongued ring made of beryllium copper that has been heat treated. Four screws hold the ring down to the backing so that the tongues press down on the diamond and keep it firmly in place. Figure 4.5 shows the ring and its relation to the diamond and the backing. The lengths of the tongues are such that they touch the diamonds' sides before the bottom of the ring makes complete contact with the backing. This assures that the diamonds are firmly held down as the four screws tighten the ring down, since the tongues act as linear springs.

Before pressurization, the diamonds need to be aligned. The two halves of the DAC are put together very carefully since they have been machined with very high tolerance. These two halves can only fit each other one way as there is a pin sticking out on the side of the lower half that fits into a groove on the side of the upper half. First, the diamonds must be aligned laterally using the three Allen screws on the sides of the upper half of the DAC (see fig. 4.4) (these screws move the upper backing in the radial plane) while looking through the diamonds at their culet faces with a powerful stereo microscope. The hexagons of the culet faces should also be aligned so that they overlap perfectly. To do this the two halves of the DAC should be taken apart and the backing of the upper half turned in the correct direction. When pulling the two halves of the DAC apart, one needs to use a large force (manually) at the beginning because the lubrication used to reduce the friction between these parts is spread over a larger contact area. As the

halves are pulled apart, the applied force should be decreased so they do not accelerate away from each other. This acceleration causes some loss of control and the lateral forces that one unknowingly applies can jam the halves at the ends. Practice is required for this process. Care must also be taken when diamonds are touching each other since they can be scratched.

The faces of the two diamonds must be parallel when the two halves of the DAC are brought together. This is done to within one wavelength of visible light by the use of the Newton's fringes. To achieve this, the lower diamond assembly sits on a spherical-arc (the center of the sphere is on the culet face) rocker that allows for the wobbling movement of the lower diamond. It rocks by the use of the three "rocking screws" on the bottom of the lower half of the DAC. Again, the diamonds are brought together under a stereoscopic microscope. A light source is placed under the microscope and transmitted through the diamonds. Fringes of light appear across the hexagon (there are two hexagons but they perfectly overlap and appear as one) as strips of "rainbow" since the light source is not monochromatic. While the fringes are watched under the microscope, the rocking screws on the bottom are turned as needed so that the distance between the fringes increases until the fringes finally disappear. The rocking screws should not be too tight or too loose; neither should they drastically differ in the torque required for alignment. All of these could cause strange stresses to build up which could cause misalignment of the diamonds after the first pressurization or the first cool-down of the DAC. The two halves of the DAC should now be taken apart and put back together and the alignment of the diamonds should be

checked again. When the diamonds are aligned correctly, no fringes should be seen and different colors of the visible spectrum should appear uniformly across the culet faces (in the case of a non-monochromatic transmitted light) as the diamonds are pulled apart.

High pressure is achieved by drilling a hole, smaller than the culet size, in a sheet of stainless steel or some other appropriate metal called a gasket filling it with a pressure medium and the sample under investigation, and sandwiching it between the culet faces of the diamonds. As the diamonds are forced closer to each other and thereby pinch the gasket, pressure is built up and increases inside the small hole containing the sample and the pressure medium. To achieve very high pressures the gasket must be preindented by the diamonds before the hole is drilled.

A gasket of an appropriate material (usually the thickness of the gasket is 0.010 inches and it is made of stainless steel or spring steel) is cut into an equilateral triangle to fit inside the inner diameter of the upper half of the DAC. On the backing retainer of the upper half of the DAC (see fig. 4.4) there are three tapped holes. One has to drill out three holes on the gasket to match these tapped holes. The gasket is then fastened (not too tight, not too loose) onto the retainer using three screws. Before the gasket is screwed down to the retainer, the culet face of the diamond is cleaned with a cotton applicator and acetone. The gasket is marked at some corner so that it can be put back in its place exactly in the same orientation. Now the gasket is screwed down to the retainer, slightly pushing on the diamond at its center, and is marked at some corner. The other diamond's

culet face should also be cleaned with acetone and a cotton applicator. This step should be done carefully since there are four wires around the base of this diamond that might get damaged by the cotton applicator.

The DAC is now assembled (two halves put together) and put inside a specially designed press. Pressure is applied to the DAC until the gasket is preindented appropriately. It has been found in this lab that "appropriately" means that the thickness of the preindented area should be more or less equal to the diameter of the hole to be drilled in the gasket. There is an indicator on the press that has been calibrated to do just that. Once the gasket is preindented, the DAC is disassembled and the gasket removed. Now the challenge is to drill a hole, usually 0.25 mm in diameter, in the middle of the preindented area. This should be done under a very powerful microscope using a micropress and a sharp tungsten-carbide drill. One way to find the exact center of the area is to put a very sharp pin in place of the drill bit and measure the distances to the sides of the preindented area while the gasket is firmly held on an x-y stage equipped with micrometers. After the hole is drilled out, a slightly larger drill bit is used to chamfer the edges of the hole and then the gasket is cleaned with acetone in an ultrasonic bath. The diamonds are cleaned again and the gasket is screwed back in its place on the upper diamond.

The pressure inside the hole is measured by optical means[53]. This is done by measuring the change in the wavelength, $\Delta\lambda$, of the ruby fluorescence. The R lines of Cr^{3+} in ruby are quite intense and the doublet R_1 and R_2 have the wavelengths 6927 and 6942 Å respectively. These lines shift linearly with hydrostatic

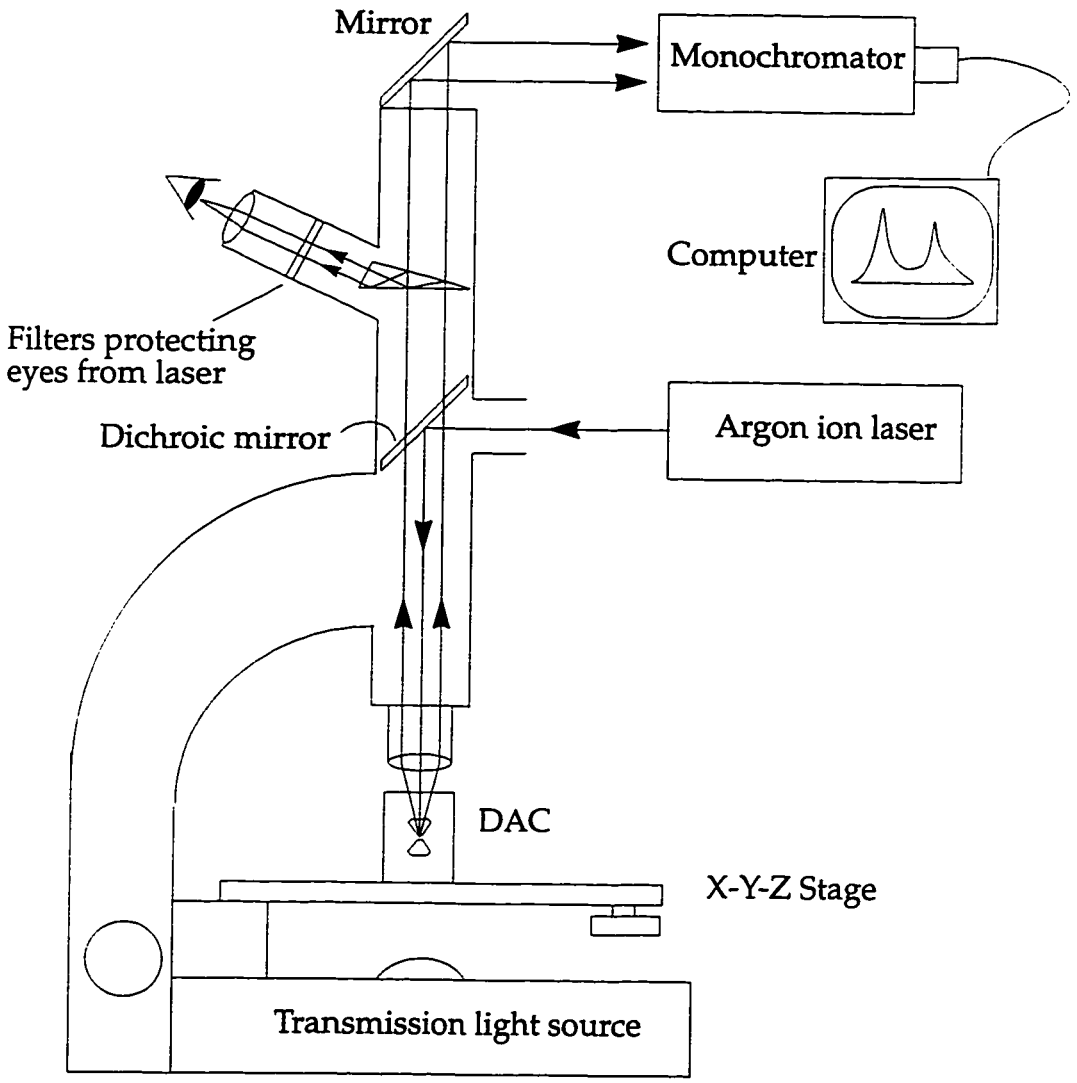

Figure 4.6. Schematic of the pressure measurement set up using the ruby fluorescence technique.

pressure at a rate of 0.365 Å/kbar up to ~300 kbar, beyond which the linearity doesn't hold and the equation P(Mbar) = 3.808 $[(\Delta\lambda/6942)^5-1]$ ($\Delta\lambda$ in nm) should be used to measure the pressure. If the pressure becomes non-hydrostatic, the R lines broaden. These lines are excited by an intense light source or by a laser such as an Ar-ion laser focused on the ruby under pressure by the aid of a powerful microscope. This pressure measuring microscope is coupled to a monochrometer for wavelength measurements. Figure 4.6 shows the schematic of such set up.

A few ruby chips are placed at the bottom of the drilled hole on the diamond face, working under a powerful microscope. This is done carefully with a sharpened wood stick. If the ruby chips are too large, they need to be ground down in a mortar. The hole should now be filled with an appropriate pressure medium. For resistivity measurements, powdered $CaSO_4$ is used since it is very soft and becomes transparent under pressure. The hole should be packed with $CaSO_4$ powder by first placing a small amount of the powder with a sharpened wooden stick in the hole on the ruby chips. The DAC should then be assembled and pressed with fingers to compact the powder. This process should be repeated until the hole is completely filled with compacted $CaSO_4$ powder.

Some epoxy is now applied to the surroundings of the indentation area (see figure 4.7). The epoxy in this region helps to secure the Al_2O_3 powder applied later as described below. Resistivity measurements inside a DAC are very difficult since the wires that are fed into the hole must be insulated from the metal gasket. This is done as follows. When the epoxy is set, a very fine Al_2O_3 powder is applied to the indentation area as seen in the inset of figure 4.7. In order to

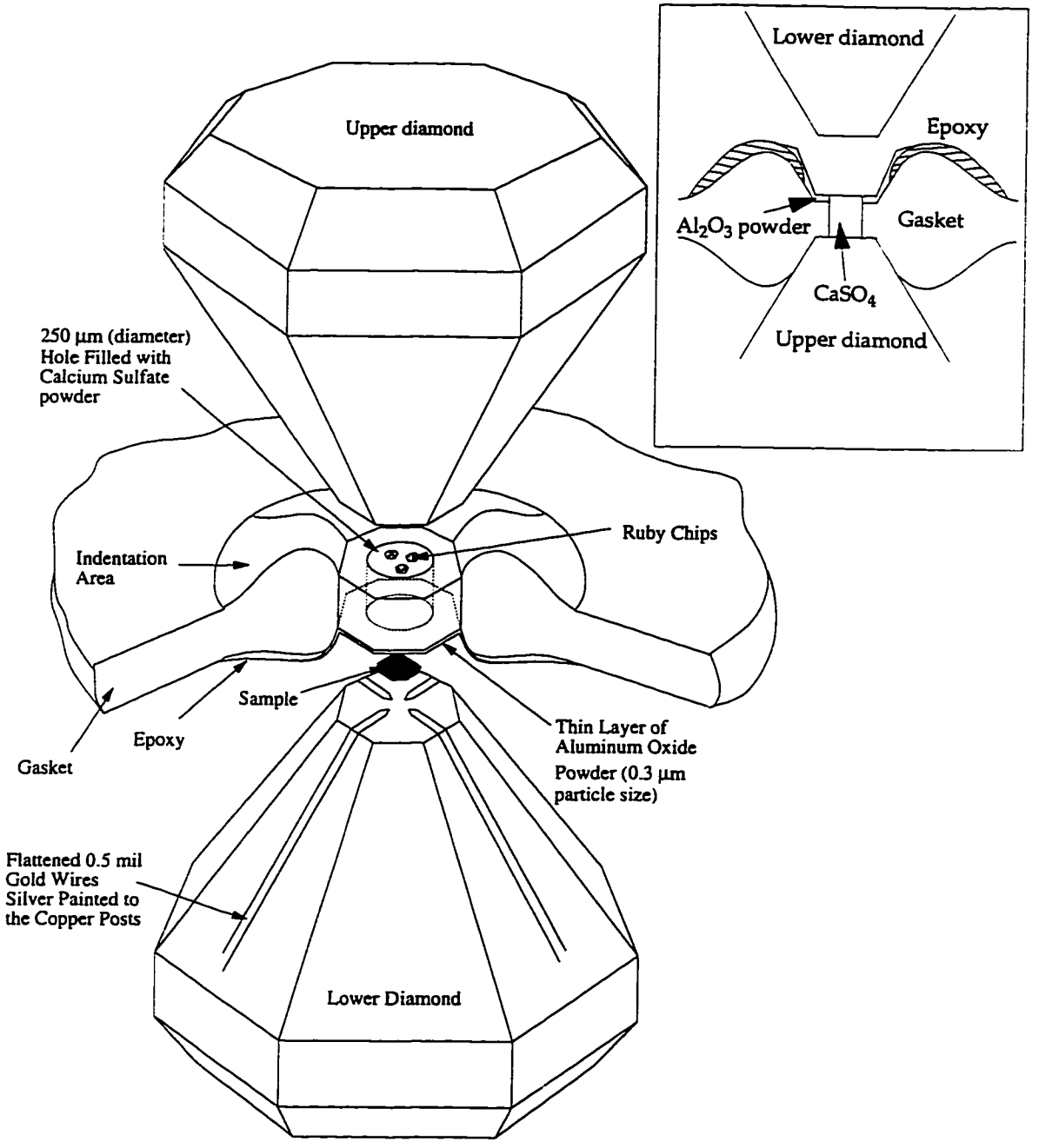

Figure 4.7. The details of the sample wiring in a DAC.

avoid the inclusion of the Al_2O_3 powder into the hole, it is mixed with some E. B. Acetate to make an Al_2O_3 "paint". This "paint" is then applied to the area and set aside to dry out. The DAC is then assembled and the Al_2O_3 powder is pressed by fingers into a thin layer. This layer acts as an insulator for the wires.

A long piece (~10 cm) of 0.5 mil gold wire is laid down on a very smooth surface such as Plexiglas or a glass slide. The wire is flattened by rolling a stainless steel roller on it making a gold ribbon. It is then put under a microscope and cut into approximately 1 cm pieces. The cuts are not made perpendicular to the length of the wire. Instead, the cuts are made so that the resulting pieces have pointy ends (see figure 4.7). The wires are then picked up with a tweezer and glued to the culet face of the lower diamond, forming a star, using tiny dabs of epoxy. When the epoxy is set, the other end of the wires (which are now hanging from the culet face radially outward in a diving board fashion) is bent carefully so that they lay on the diamond's side as shown in figure 4.7. The ends of the wires must be silver painted to the copper posts at the base of the diamond (see figure 4.8). The copper posts, which are just the ends of four pieces of 3 mil insulated copper wires, will eventually come out of the DAC from the bottom for resistivity measurements.

The samples used in Zettl's lab are usually in single-crystal form. To prepare the sample for the resistivity measurements inside the DAC, it should first be sanded into a very thin layer, about 10-20 μm thick. Since the sample is small, sanding is extremely challenging and difficult. One reason for this is that sanding can crack the sample into very small pieces, practically powder. For this reason,

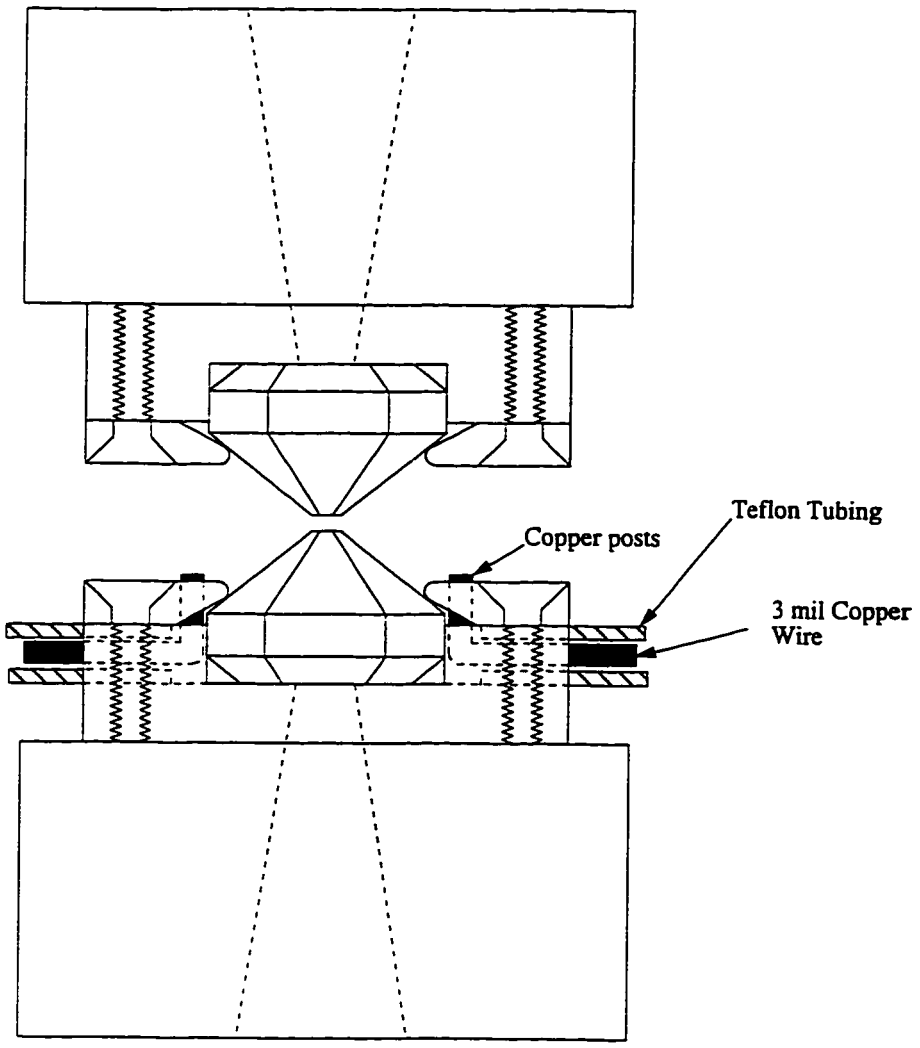

Figure 4.8. The copper posts that lead outside the DAC for resistivity measurement purposes.

the sample is embedded inside a transparent hard glue, such as super glue, on a glass slide. It is then sanded very carefully until the desired thickness is reached. To remove the super glue, a few drops of acetone are poured on the hardened glue until it is dissolved away. The sample is cut roughly into a square 0.05 mm on the side (again, under the microscope). It is then placed on the compacted $CaSO_4$ powder on the gasket without disturbing the flatness of the powder. The lower half of the DAC (the half with the wires) is then closed onto the upper half containing the sample, while looking through the diamond. Before the sample makes contact with the wires, one needs to make sure that all the wires will come in contact with the sample as the DAC closes completely. If it looks like one or more wires will not end up on the sample, the DAC has to be opened and the sample moved to the right location. Once the DAC is closed with the sample successfully loaded, the locking nut (see figure 4.4) should be put in place and the sample pressurized to the desired pressure. The temperature is measured with a calibrated silicon diode mounted on the retainer of the lower diamond.

Chapter 5

Resistivity and magnetoresistance measurements at high pressures

5.1 $\rho(T, P)$ of $Nd_{0.62}Pb_{0.30}MnO_{3-\delta}$

In 1995 S. Jin, et al.[54] prepared two polycrystalline samples of $La_{0.67}Ca_{0.33}MnO_{\delta}$ and $La_{0.60}Y_{0.07}Ca_{0.33}MnO_{\delta}$. X-ray diffraction measurements revealed that the lattice parameter of $La_{0.60}Y_{0.07}Ca_{0.33}MnO_{\delta}$ was smaller than that of $La_{0.67}Ca_{0.33}MnO_{\delta}$ by ~0.2%. The magnetoresistance of the $La_{0.60}Y_{0.07}Ca_{0.33}MnO_{\delta}$ sample was an order of magnitude larger than the $La_{0.67}Ca_{0.33}MnO_{\delta}$ sample (figure 5.1). The authors attributed this increase in MR to the smaller lattice parameter of $La_{0.60}Y_{0.07}Ca_{0.33}MnO_{\delta}$. To test this idea, the magnetoresistance of a single crystal of $Nd_{0.62}Pb_{0.30}MnO_{3-\delta}$ (grown in the Zettl lab) was measured as a function of pressure.

Single crystals of $Nd_{0.62}Pb_{0.30}MnO_{3-\delta}$ were grown using the flux method described in chapter 2. The crystal used in this study was a rectangular parallelepiped of dimensions 1 mm × 0.14 mm × 0.14 mm with smooth reflective surfaces. X-ray diffraction showed a single phase with lattice constant 3.86 Å. Energy dispersive X-ray spectroscopy (EDX) measurements on several parts of the sample

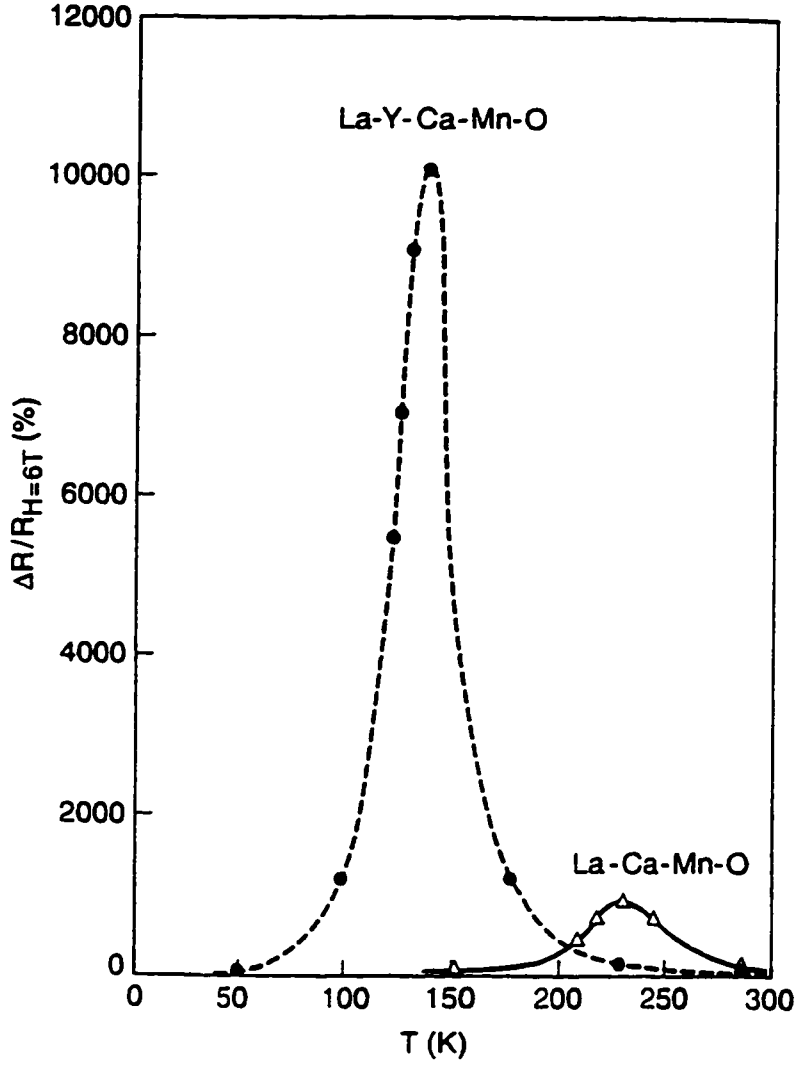

Figure 5.1. Magnetoresistance of two polycrystalline samples of $La_{0.67}Ca_{0.33}MnO_{\delta}$ and $La_{0.60}Y_{0.07}Ca_{0.33}MnO_{\delta}$, after reference 50.

showed a uniform stoichiometry of $Nd_{0.62}Pb_{0.30}MnO_{3-\delta}$[55]. Current leads were attached with silver paint to the smaller end faces of the crystal. Voltage leads were attached 0.4 mm apart along the long axis. The resistivity was first measured at zero pressure from 10 to 300 K with and without an applied magnetic field.

The sample was next mounted in a self-clamping pressure cell with Flourinert FC-75 as a pressure medium, and a clamping pressure of approximately 6 kbar was applied at room temperature. The resistivity was again measured from 10 to 300 K with and without an applied magnetic field. The pressure inside the cell drops monotonically with decreasing temperature because the thermal expansion coefficient of the cell is smaller than that of the pressure medium. A calibrated manganin coil monitored the pressure inside the cell as a function of temperature as described in section 4.2. The pressure decreased by 2-3 kbar as the temperature was lowered from 300 to 10 K. The procedure was repeated for clamping pressures of approximately 8 and 12 kbar so that resistivity $\rho(T, P)$ and $MR(T, P)$ as functions of temperature and pressure were obtained. The theoretical interpretation of the data is due to Vincent H. Crespi and Marvin L. Cohen.

Figure 5.2 shows the resistivity as a function of temperature in zero applied magnetic field for zero initial pressure and three different clamping pressures. The sharp narrow transitions are characteristic of a uniform high-quality crystal. Comparison of cooling and warming data show no hysteresis in temperature. The temperature T_{MI} (which is very close to the Curie temperature T_c) of the peak in resistivity increases with application of pressure. The magnetic phase is stabi-

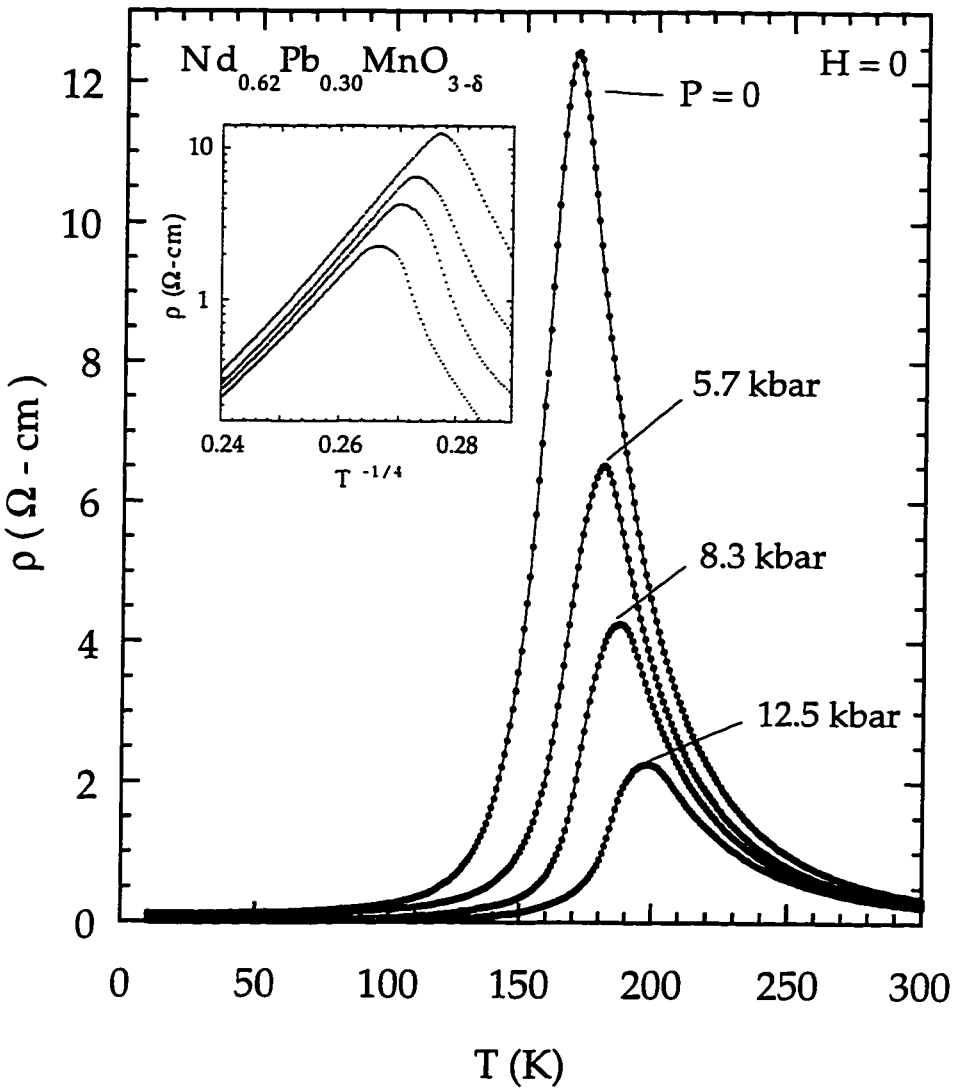

Figure 5.2. Resistivity of single-crystal $Nd_{0.62}Pb_{0.30}MnO_{3-\delta}$ as a function of temperature in zero applied magnetic field for clamping pressures of 0, 5.7, 8.3, and 12.5 kbar. The inset shows the high-temperature behavior of the resistivity.

lized under pressure which is consistent with the double exchange model[9,10,11] (explained in section 3.5) in which ferromagnetic order is encouraged by an increase in electronic hopping integrals[56,57]. The resistivity drops monotonically with increasing pressure at all temperatures. The general trend to decreased resistivity is consistent with an increase in electronic overlap under pressure.

As was seen in chapter 3, the zero-pressure high-temperature resistivity of $Nd_{0.57}Pb_{0.39}MnO_3$ shown in the inset of figure 5.2 has a form which resembles variable-range hopping, $\ln\rho \propto T^{-1/4}$ [34]. By considering the variation in the polaron on-site energies due to spin and cation disorder, one obtains an additional T^{-1} term ($\ln\rho \propto T^{-1/4} + T^{-1}$) which could account for the measured resistivity[32]. As the temperature is lowered, the pressure inside the cell drops (section 4.2). On the other hand, the sample's volume decreases upon cooling. Therefore, the pressure applied to the sample acts oppositely to the thermal expansion of the sample. These two counteracting effects ensure that the correction to constant volume is small at higher temperatures and the approximate $T^{-1/4}$ behavior seen is not an artifact of a varying sample volume. Pressure seems to decrease primarily the pre-factor ρ_0, having a smaller effect on the exponent T_0 in the expression

$$\rho = \rho_0 e^{\left(\frac{T_0}{T}\right)^{\frac{1}{4}}} \qquad \text{eq. 5.1}$$

The pre-factor $\rho_0 \sim \sqrt{\frac{\alpha}{N(E_F)}}$, where α is the inverse size of the polaron[34], is more sensitive to changes in the density of states than is the slope

$T_0^{1/4} \sim \left(\frac{\alpha^3}{N(E_F)}\right)^{1/4}$, indicating that perhaps pressure mainly affects the density of states. A decrease in pre-factor is consistence with an increase in the density of states and/or an increase in the size of the polaron under pressure, both consistent with pressure destabilizing the polarons. For illustrative purposes, a polaron size of $\alpha^{-1} \sim 4$ Å implies a density of states at zero pressure of $N(0) \sim 10^{20}$ cm^{-3} eV^{-1}.

5.2 $\rho(T, P, H)$ of $Nd_{0.62}Pb_{0.30}MnO_{3-\delta}$

Figure 5.3 shows the resistivity versus temperature in an applied magnetic field of 7 Tesla for different clamping pressures. T_{MI} again increases with increasing pressure. The decrease in resistivity under pressure is not as dramatic as in zero field, since the resistivity peak itself is suppressed and broadened under field. Figure 5.4 shows T_{MI} as a function of pressure in both zero and 7 Tesla magnetic fields, revealing a linear relationship with the same slope, 2.6 K/kbar, at zero and finite field. The free-energy difference that stabilizes the low temperature phase is most likely linear in the characteristic hopping integral. The linear relation shown in figure 5.4 suggests that the hopping integral varies roughly linearly with pressure over the measured range. The same slope for a single crystal sample of $Nd_{0.5}(Sr_{0.36}Pb_{0.14})MnO_{3-\delta}$ with T_{MI} = 204 K (at P = 0 and H = 0) reported previously is dT_{MI}/dP = 2.0 K/kbar[56]. This slope is smaller than what is shown in figure 5.3 for the sample under study here. This pair of results confirms and extends measurements on polycrystalline samples[28] which indicated that $dT_{MI}/$

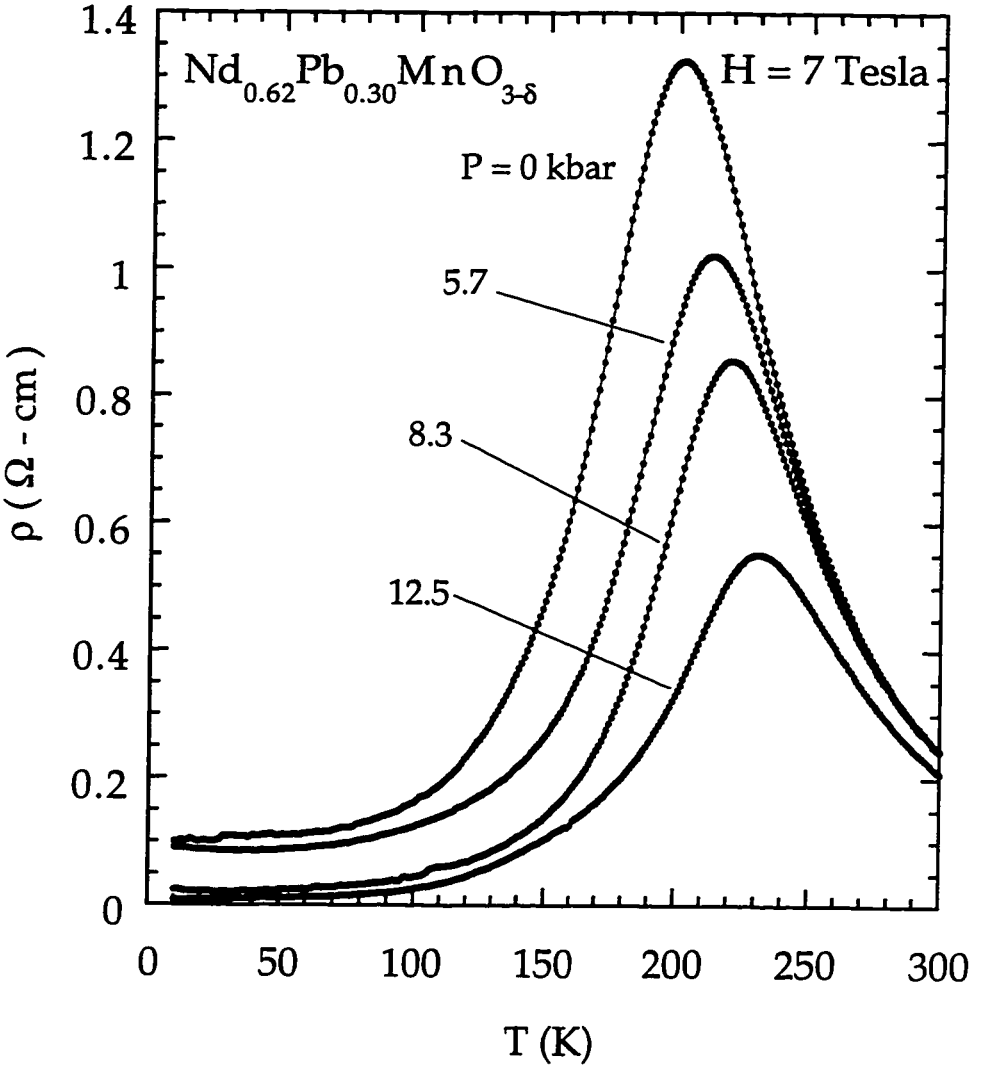

Figure 5.3. Resistivity of single crystal $Nd_{0.62}Pb_{0.30}MnO_{3-\delta}$ as a function of temperature in a 7 Tesla magnetic field for clamping pressures of 0, 5.7, 8.3, and 12.5 kbar.

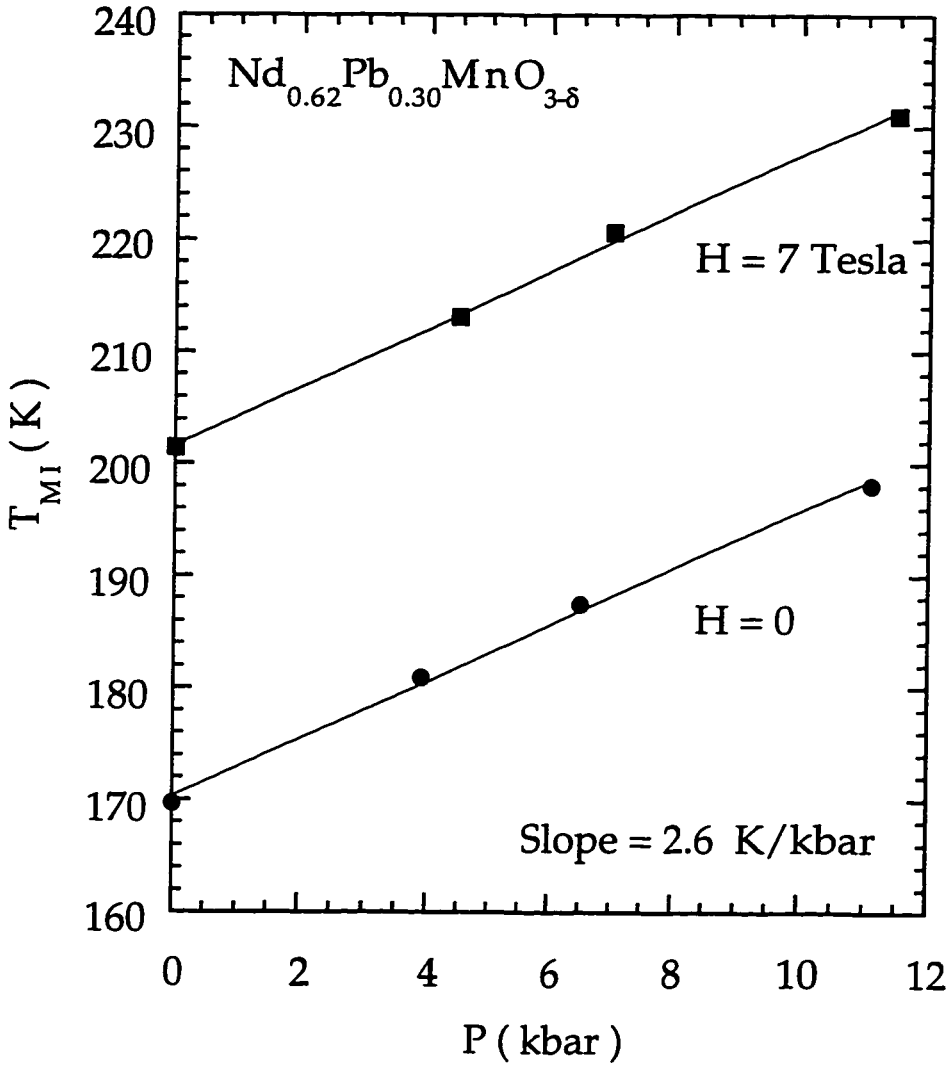

Figure 5.4. Temperature T_{MI} of peak resistivity versus pressure for zero applied magnetic field and H = 7 Tesla. Application of the magnetic field shifts the curve upwards but does not significantly affect the slope.

dP is larger for samples with lower T_{MI}.

5.3 Magnetoresitance of $Nd_{0.62}Pb_{0.30}MnO_{3-\delta}$

Figure 5.5 shows the MR defined as [R(0 Tesla)-R(7 Tesla)]/R(7 Tesla) for different clamping pressures. The inset to figure 5.5 clearly shows that peak in MR decreases as pressure increases, contrary to what S. Jin *et al.* had suspected (see figure 5.1). In fact the increase of MR reported by S. Jin *et al.* is consistent with the universal behavior of the MR versus T_c as discussed in chapter 3.

The MR peak is suppressed and moved to higher temperatures under pressure. This behavior is similar to the variations in MR and T_{MI} with doping level: in general, higher values of the MR are associated with lower values of T_{MI}, since at lower temperatures the metal-insulator transition is necessarily more abrupt. The MR above T_{MI} at different pressures is not a universal function of temperature and field: the provisional factorized form of ρ in reference 55 is not upheld by this study. The slight positive MR under pressure at the lowest temperatures may be related to the usual positive MR observed for normal metals.

The decrease in average electronic hopping rate upon entry to the high-temperature spin-disordered state induces electron localization which is consistent with either a lattice polaron[30,56,32,58], or an Anderson localization model[59]. Within the double exchange theory, the spin-ordered low-temperature phase is stabilized by reducing the electronic kinetic energy upon removal of the energy constraint against electrons hopping onto opposite-spin ionic sites (Hund's rule). The application of magnetic field clearly favors the low-temperature spin-ordered

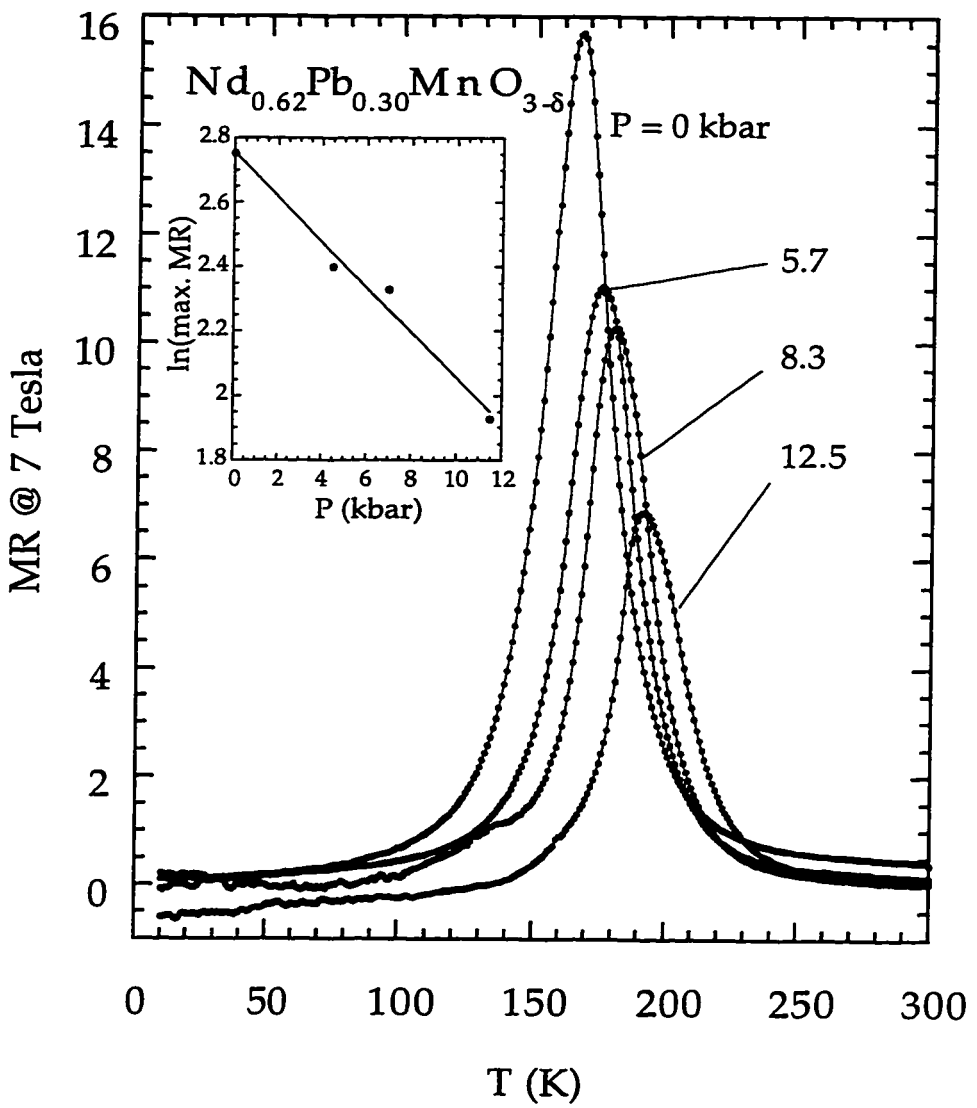

Figure 5.5. Temperature dependence of the magnetoresistance [R(0 T)-R(7 T)]/ R(7 T) of single crystal $Nd_{0.62}Pb_{0.30}MnO_{3-\delta}$ at four clamping pressures. Curves are labelled by the pressure at T = 10 K. The inset shows log of max. MR as a function of pressure.

state by aligning the spins of the ions. Pressure also directly destabilizes the high-temperature localized phase by increasing the electronic hopping rate between sites. Both the magnetic field and the external pressure increase T_{MI} and are expected to cause a large change in the resistance at temperatures near transition. For temperatures far from the transition, the pressure continues to depress the resistivity, whereas the magnetic field has little effect. The magnetic field affects the electronic hopping rate through changes in the magnetization which are only significant near T_{MI}. Pressure, on the other hand, increases the bare hopping rate at all temperatures. The bare hopping rate determines the activation energy. This activation energy is a sensitive function of average electron on-site residency time through the magnetic transition.

Figure 5.6 shows the resistivity as a function of the applied pressure on a log scale. As it can be seen, the resistivity has a roughly exponential dependence on pressure near and above the zero-pressure magnetic transition. This would be expected for hopping conduction if pressure has a roughly linear relation to the spatial extent and/or activation energy of localized electronic states away from the transition, which is consistent with a linear increase in T_{MI} with increasing pressure. The solid lines in figure 5.6 show the behavior of the resistivity in the insulating phase while the broken lines denote the behavior in the metallic phase. The deviation from exponential pressure-dependence is clear from the curves labelled 180 and 190 K for temperatures below the metal-insulator transition T_{MI}, at P=0.

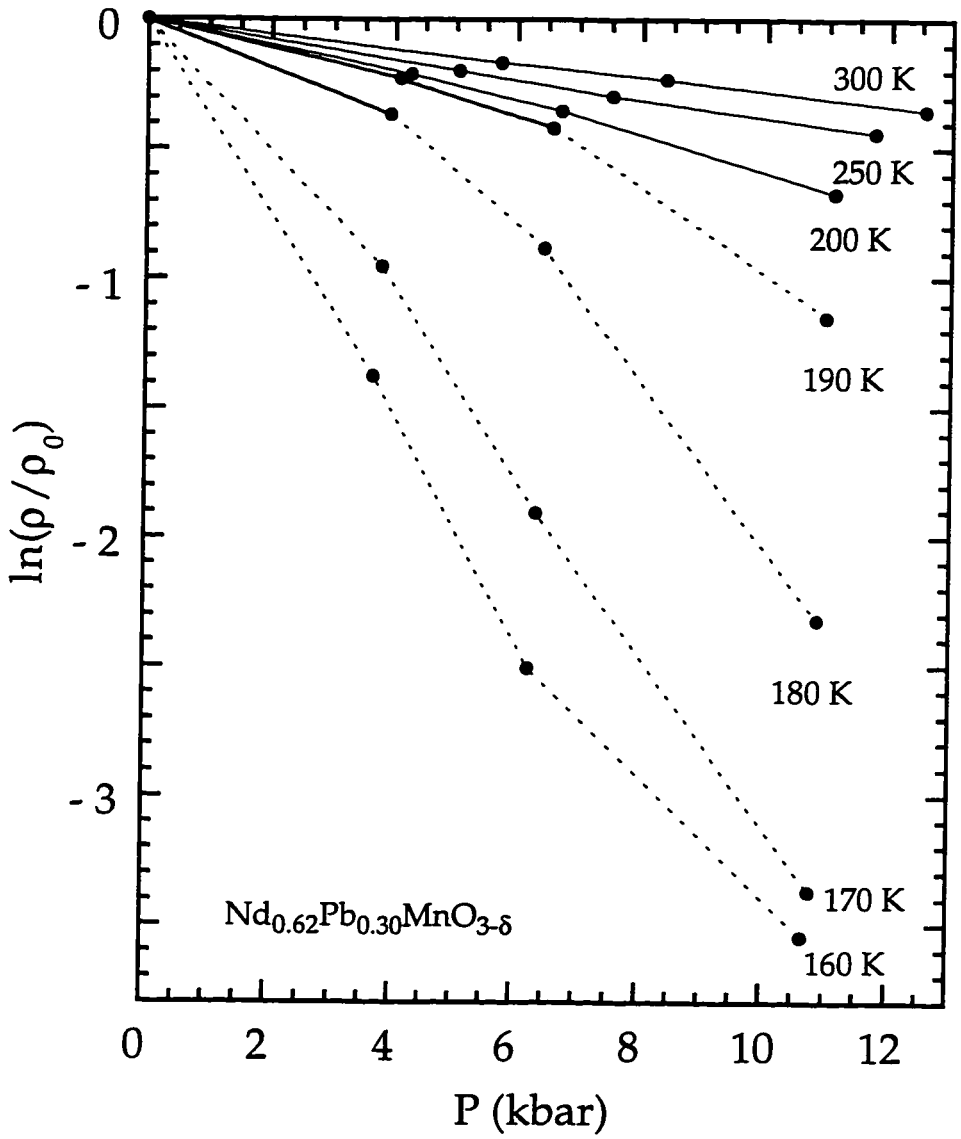

Figure 5.6. The logarithmic resistivity versus applied pressure for temperatures near and above the magnetic transition. The solid lines refer to resistivities in the high-temperature insulating phase. The broken lines refer to samples in the low temperature metallic phase. Note the nearly linear behavior, except across the metal-insulator transition. ρ_0 is the zero-pressure resistivity.

5.4 Discussion of constant-volume correction

The resistivity in these materials is extremely pressure-sensitive. This strongly suggests that changes in the volume of the sample due to thermal expansion has an unusually large influence on the temperature-dependence of the resistivity. Taking a rough guess at the bulk modulus B ~ 1000-2000 kbar, and using $d\rho/dP$ at P = 0 from figure 5.6, and a high-temperature linear thermal expansion coefficient $\alpha \sim 1.0 \times 10^{-5}$ $1/K$[12,13,14,15,16], the measured resistivity at 150 K and P = 0 is a factor of approximately 2 larger than the resistivity would have been if the T = 50 K volume had been maintained assuming the thermal expansion coefficient stays constant at all temperatures and pressures. For higher temperatures the pressure sensitivity is smaller: the resistivity at 300 K is roughly about 1.05 times larger than it would have been if it had maintained the T = 200 K volume. A detailed theoretical model of the resistivity versus temperature should take into account the large effects of thermal expansion, which contributes a substantial positive temperature coefficient to the resistivity, independent of intrinsic temperature-dependent conduction processes. Correction for this effect awaits careful measurement of the bulk modulus and thermal expansion as functions of temperature and pressure.

5.5 Low-temperature $\rho(T, P)$ of $Nd_{0.62}Pb_{0.30}MnO_{3-\delta}$

The resistivity at lower temperatures retains a strong pressure sensitivity (up to $d(\ln\rho)/dP \sim 3$ $kbar^{-1}$), as shown in the resistivity curves in figure 5.7. The pressure derivative $d(\ln\rho)/dP$ at low temperatures and moderate pressures is as

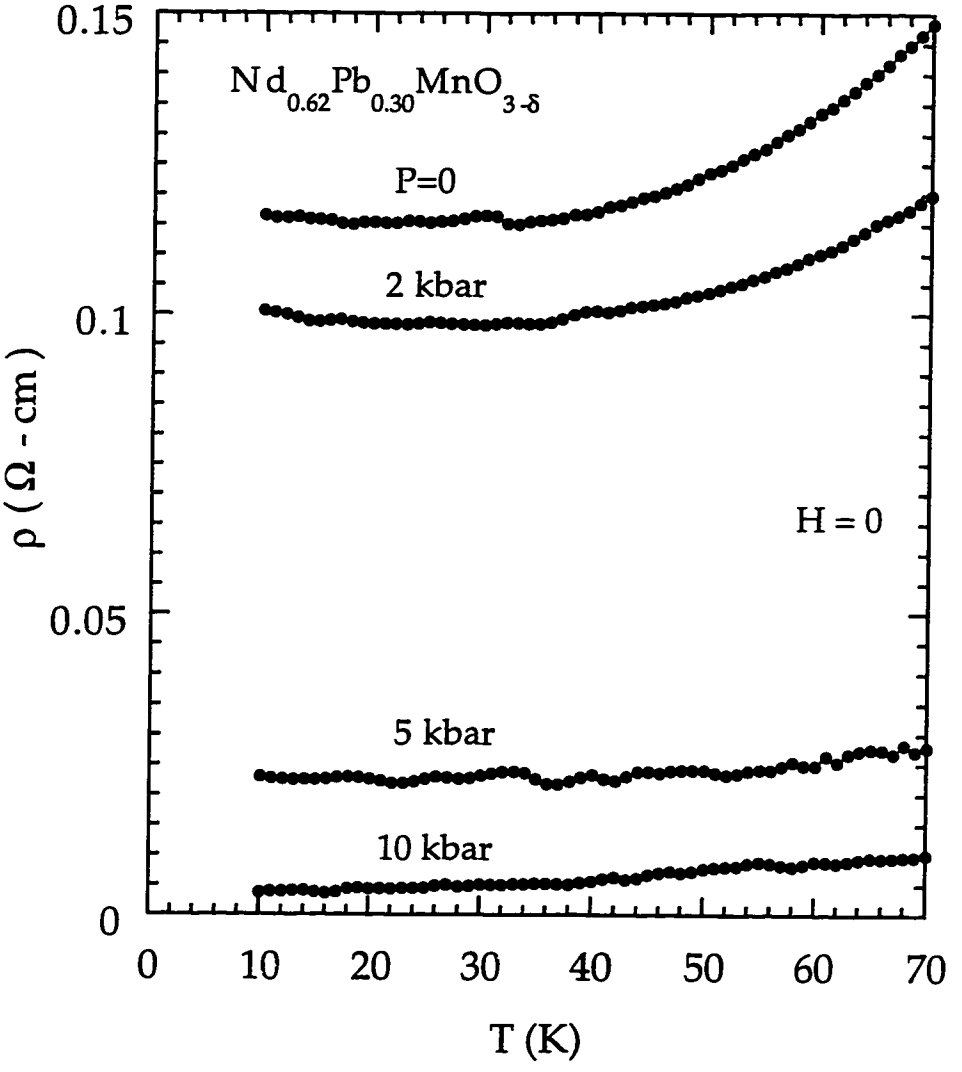

Figure 5.7. Low temperature resistivity upturn is suppressed by the application of greater than 5 kbar pressure. Curves are labelled by the pressure at T = 10 K.

large as those observed near T_{MI}. This large sensitivity away from the transition may seem surprising since the crystal at these low temperatures is in a magnetically ordered state which is apparently metallic. A hint towards this pressure sensitivity is perhaps clear from the upturn in the resistivity at the lowest temperatures and pressures (figure 5.7). Similar measurements on polycrystalline samples with lower doping levels show a similar but more pronounced upturn at low temperatures[60]. Underdoped compounds can show a reemergence of hopping conduction below the resistive transition which suggests that the increase in bare electron hopping rate at temperatures below the transition is sometimes insufficient to unbind the polarons. The continuous evolution of low temperature activated behavior as a function of doping suggests that the upturn observed in optimally doped samples has the same origin, a pressure-dependent incipient activation barrier in the nominally metallic low-temperature phase. As long as the hopping barrier is small or moderate compared with kT, the conduction can present a metallic-like temperature dependence, particularly since thermal expansion biases $\rho(T)$ upwards. A measure of covert hopping or "bad metal" behavior is consistent with a large value of the resistivity in the metallic-like phase which violates the Ioffe-Regal limit as mentioned in section 3.2. Figure 5.7 suggests that the low-temperature pressure dependence of ρ may be weaker at the lower pressures. A detailed correction for thermal expansion is impossible at this time, but the data suggest that lower value of $d\rho/dP$ (at both low and high temperatures) are associated with an activated constant-volume resistivity and very large value of $d\rho/dP$ are associated both with the vicinity of the transition and with regions

of positive temperature coefficient of the resistivity. This common pressure dependence of both activated regimes suggests a common conduction mechanism.

Chapter 6

Introduction to Fullerenes

6.1 Historical Review

Between 1980 and 1984, Richard Smalley and his colleagues at Rice University developed a mass-spectroscopic technique to study the molecular clusters generated in a plasma produced by focusing a pulsed laser on a solid target (usually metallic or semiconducting)[61]. In 1985 they discovered a dominant peak at 720 amu on a mass-spectrograph obtained when a graphite target was used[62]. This peak was assigned to a closed hollow structure containing sixty carbon atoms which completely eliminates all dangling bonds. This closed structure consists of 12 pentagons and 20 hexagons with each pentagon completely surrounded by five hexagons (with one carbon atom at each vertex) resembling a soccer ball. The point group symmetry of the molecule is I_h with 120 elements (icosahedral). The bond between two neighboring carbon atoms on the "bucky ball" is an admixture of sp^2 and sp^3 due to the finite curvature of this "graphitic" sheet. The diameter of the C_{60} molecule is 7.1 Å. Figure 6.1 shows the cage like structure of the C_{60} molecule.

It was soon recognized that C_{60} is a by-product of incomplete combustion[63]. In 1989 Kratschmer et al.[64] successfully produced C_{60} in large

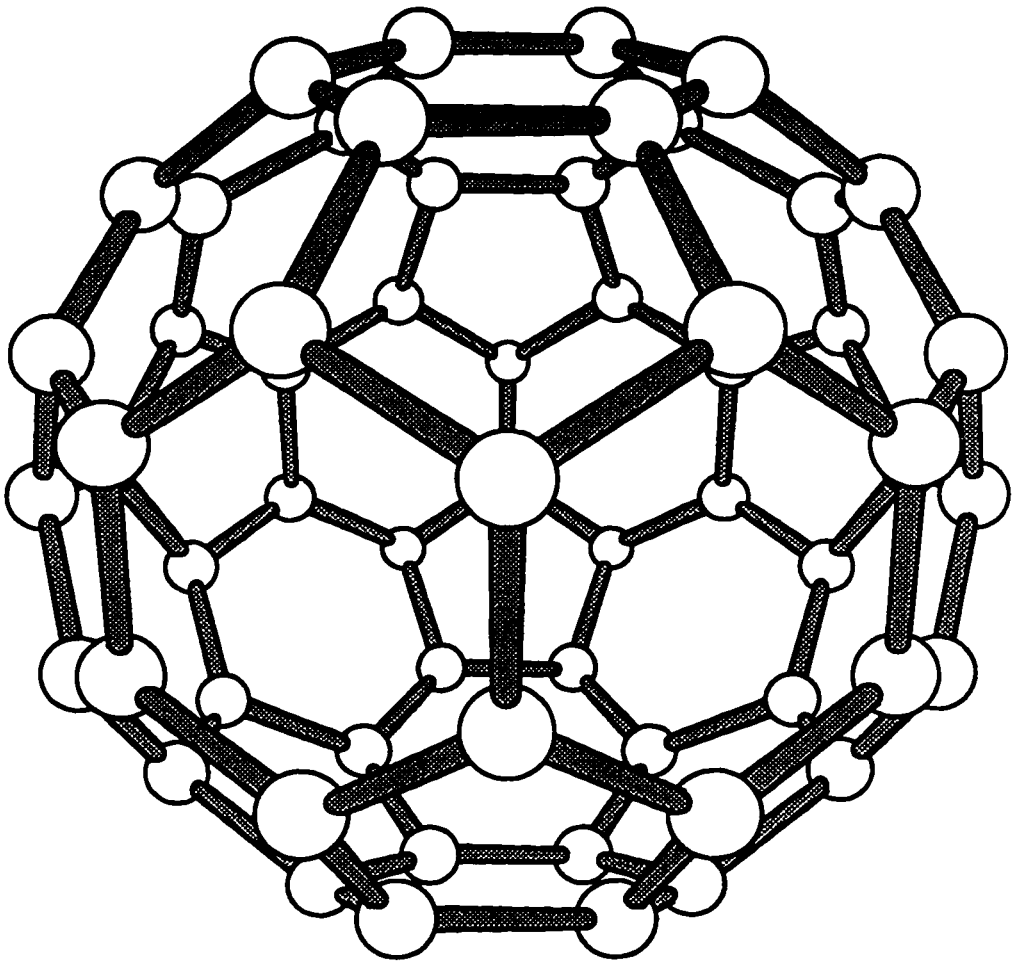

Figure 6.1. The cage-like structure of the C_{60} molecule.

quantities by obtaining soot from arc-processed graphite. With large quantities of C_{60} available, single crystals of solid C_{60} were soon synthesized. The crystal symmetry of this solid was determined and it was shown that solid C_{60} is a semiconductor in which C_{60} molecules are held together by Van der Waals forces. Upon doping with the correct stoichiometry of alkali metals (A_3C_{60} where A denotes an alkali metal), solid C_{60} becomes metallic and a relatively high temperature superconductor[65]. The alkali doped phases of solid C_{60} will be discussed in section 6.3.

6.2 Solid C_{60}

As it was mentioned in the previous section, large quantities of C_{60} are extracted from the soot which is produced by arc-burning graphite rods. The soot is made in an inert atmosphere (e.g. helium) by producing an electric arc between two water-cooled graphite rods using a high current dc power supply. The soot is then mixed with sufficient quantity of benzene or toluene, in which C_{60} is soluble, and placed in an ultrasonic bath to dissolve as much C_{60} as possible. The dissolved C_{60} is then separated from other fullerenes by flash-chromotography yielding a magenta solution. The solvent is evaporated away by heating this solution and C_{60} is extracted as a fine crystalline powder at the bottom of the container.

In order to make physical measurements on solid C_{60}, the crystals must be sufficiently large. The larger crystals are synthesized by vapor transport tech-

nique (synthesized in Zettl's lab by Michael Fuhrer). Powder C_{60} is placed in a gold "boat" inside a quartz tube about 1.4 cm in diameter (1 mm thickness). The quartz tube has "necks" about 1.5 inches apart to induce some turbulence. This quartz tube is then put inside a larger quartz tube (2.5 cm diameter) in which Argon gas flows at a rate of 10 cc/min. The assembly is placed inside a three-zone furnace and temperatures set to 630, 565, and 500 Celsius so that the temperature of the "boat" is at 630 C. The schematic of the arrangement is shown in figure 6.2. The larger crystals form at the cold end in 10 to 15 days.

The quasi-spherical C_{60} molecules form an fcc lattice at room temperature in solid C_{60}. The cubic lattice constant of this fcc crystal is about 14.16 Å. The center-to-center nearest neighbor distance is ~ 10 Å. At room temperature, the molecules rotate effectively free (greater than 100 MHz)[66]. As the temperature is lowered below 260 K, the rotational motion suddenly changes due to an orientational ordering. This transition is accompanied by an abrupt contraction of the lattice constant of about 0.049 Å[67,68]. The C_{60} molecules are no longer at symmetry equivalent sites because of the orientational ordering which leads to a simple cubic structure. This low temperature structure can be understood and traced back to the anisotropic electronic distribution of each C_{60} molecule which comes from two types of carbon-carbon bonds. The electrostatic contribution and the predominately Van der Waals intermolecular bonding is then optimized by aligning the electron-rich regions of the molecule on the electron deficient regions of its neighbors. The rotational dynamics of the molecules below this transition can be described as jump-reorientation motion as the molecules ratchet between two

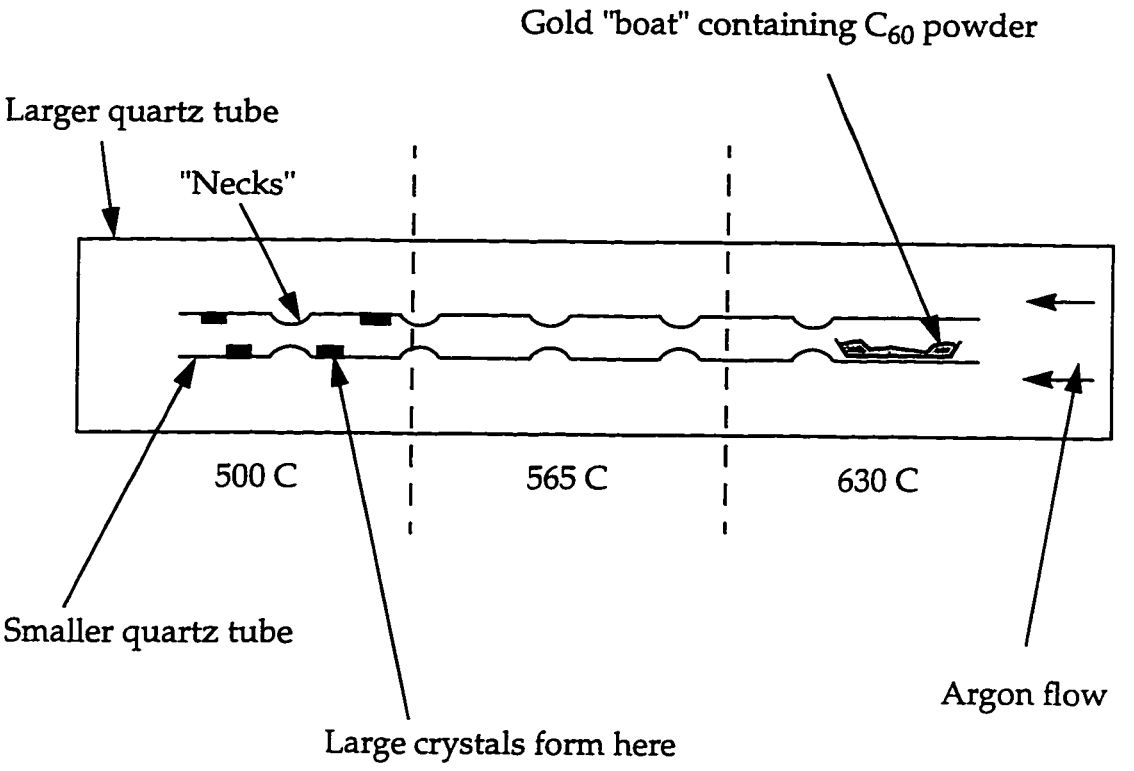

Figure 6.2. Schematic of the assembly needed for C_{60} crystal growth.

nearly degenerate orientations differing in energy by 11.4 meV[69]. There is another phase transition at ~90 K below which the molecular jump motion freezes and a transition to an orientational glass phase occurs[70].

The ground state of the solid C_{60} is insulating with a direct gap at X of 1.23 eV. The valence band accommodates 10 electrons, and comes from the molecular h_u states which have been broadened into a band 0.63 eV wide. The conduction band is formed from the molecular states of t_{1u} symmetry with width of 0.55 eV[71].

6.3 Alkali-doped solid C_{60}

Pure C_{60} forms an fcc solid at room temperature[67]. The fcc structure has one octahedral and two tetrahedral interstitial sites. These sites accommodate the alkali atoms in doped solid C_{60}. There are many stable phases of alkali-doped solid C_{60}. These are denoted as A_xC_{60} (where A stands for alkali atoms) with x=1, 2, 3, 4, and 6. The x=3 member of the family is air-sensitive, metallic, and a high temperature superconductor with T_c's of 20 and 30 K for K and Rb dopants respectively[65]. The band structure of this member of the family is more or less the same as that of pristine solid C_{60} with the conduction band half filled[72]. The x=2, x=4 and x=6 members are air-sensitive insulators. It was recently discovered[73,74] that the x=1 member is an air-stable metallic phase at temperatures below 400 K in which the C_{60} molecules are bonded to each other forming linear polymerized chains. The polymerized alkali doped phase of the solid C_{60} is the subject of this and the next chapters.

6.4 Polymerized Alkali-doped solid C_{60}

Polymerized alkali doped C_{60} is the only air-stable alkali doped solid C_{60} compound. It has been shown[73,74] that this unique phase is also stable in toluene, unlike all other phases of alkali doped C_{60}. At temperatures above 400 K, AC_{60} has a rock salt structure. Upon cooling slowly through 400 K, the C_{60} molecules polymerize into long chains with a substantial contraction of the unit cell along the polymerization direction (see figure 6.3).

The alkali doped polymerized C_{60} sample used in this study were synthesized by J. Hone in Zettl's materials synthesis laboratory as follows. Pristine solid C_{60} was first grown by the vapor transport method described in section 6.2. These crystals were then sealed in an evacuated quartz tube with a stoichiometric amount of the alkali metal. The tube was heated to 400 C for five days and cooled to room temperature over ~ 10 hours. The doped crystals were then exposed to air and immersed in toluene. This step insures removal of any pristine C_{60} or other phases of the alkali doped C_{60}. After a few days, the insoluble pieces were removed. While these samples are not truly single crystals, they have proved sufficient for a variety of measurements. These samples have been characterized by powder X-ray diffraction and transmission electron microscopy[75].

Since its recent discovery[76], polymerized AC_{60} has been characterized by many techniques, including structural analysis (XRD[77,78], TEM[75]), magnetic probes such as NMR[79-84], electron spin resonance ESR[77,85,86,87] and muon spin resonance[88,89,90], optical spectroscopy[91,74,92-96,97,98,99], and electronic transport[94,100].

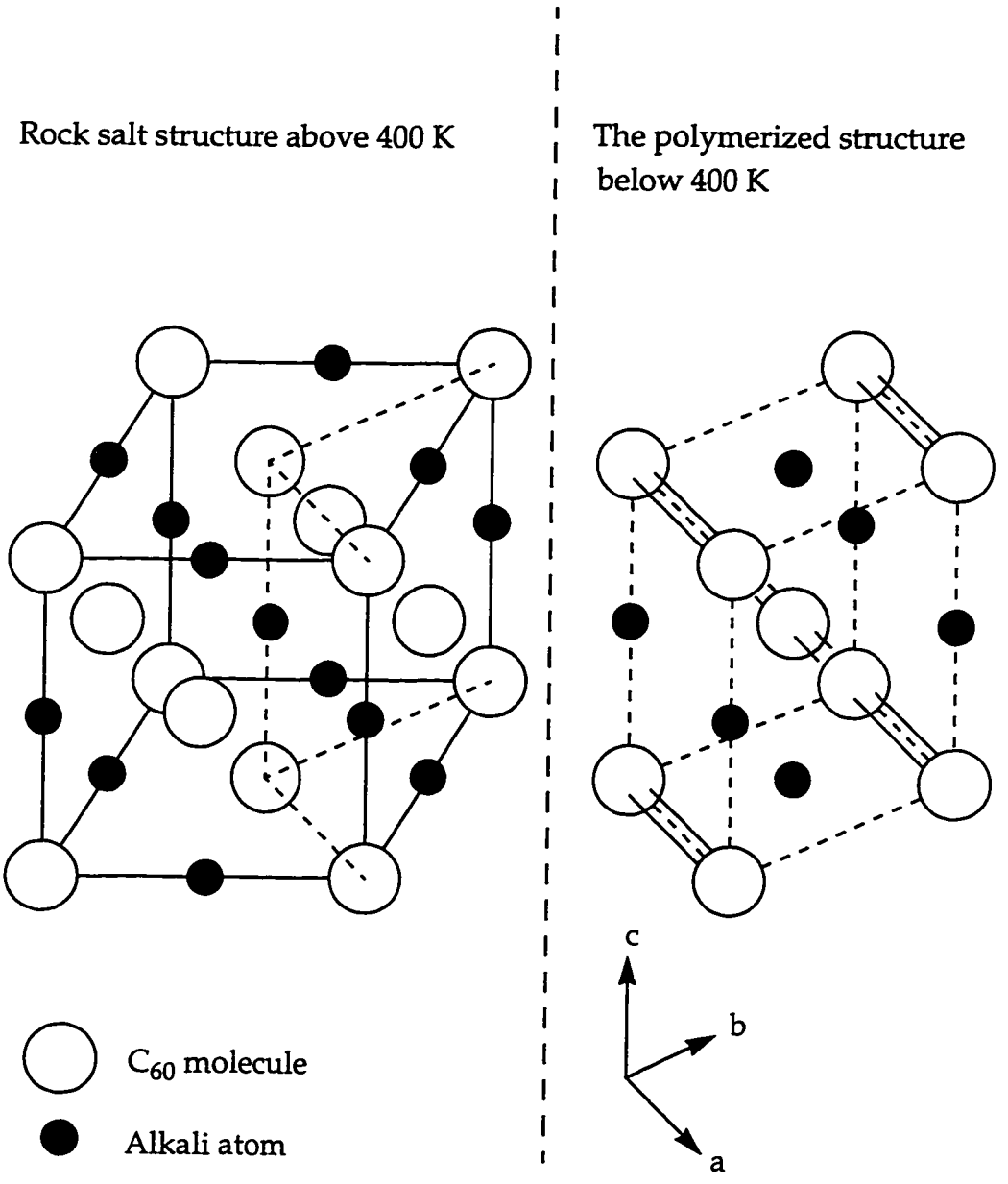

Figure 6.3. The unit cell of polymerized alkali doped AC_{60} at temperatures above and below 400 K.

Optical and magnetic probes indicate that polymerized RbC_{60} and CsC_{60} undergo a transition to what seems to be a magnetic ground state at a transition temperature close to 50 K. These "magnetic signatures" have not been found in polymerized KC_{60}.

The structure of these compounds is interesting in itself. It consists of covalently bonded C_{60} molecules which form linear chains as shown schematically in figure 6.3. The lattice constants of polymerized KC_{60} and RbC_{60} are a = 9.11Å, b = 9.95Å, c = 14.32Å and a = 9.13Å, b = 10.11Å, c = 14.23Å respectively[77,78]. The possibility of one-dimensional conduction arises from such geometry; however, there have been suggestions[101] that the electronic transport along the chains is complicated by the existence of the covalent bonds between the C_{60} molecules. The electronic transport perhaps follows a zig-zag pattern were electrons hop from one chain to a neighboring chain. In spite of the structural similarities between polymerized KC_{60} and RbC_{60}, they have greatly different transport properties at zero pressure. The transport properties of polymerized KC_{60} and RbC_{60} are the subject of the next chapter.

Chapter 7

Resistivity measurements of polymerized AC_{60} (A = K, Rb)

7.1 ρ(T, P) of polymerized KC_{60} at zero and high pressure

Molecular solids have narrow electronic band widths with large density of states. Therefore, the electronic transport in these materials is extremely sensitive to small changes in lattice parameter. The resistivity of Rb_3C_{60} versus temperature follows a T^2 form at zero constant pressure. However, at constant volume, it becomes a linear function of temperature[102]. This result motivated the pressure study presented in this chapter.

The sample used in this study was gray/black and is of "polycrystalline" nature. DC resistivity measurements were performed using the standard four-probe technique. The best contacts were obtained by cleaving the surface of the sample and evaporating gold pads on it using a mask and an evaporator. Gold wires were then glued to the gold pads using silver paint.

Figure 7.1 shows the resistivity of polymerized KC_{60} as a function of temperature at zero pressure (measurements were performed by J. Hone[100]). ρ(T) shows a metallic temperature dependence from room temperature down to ~ 50 K, i.e. ρ decreases with decreasing temperature. ρ(T) does not follow any conven-

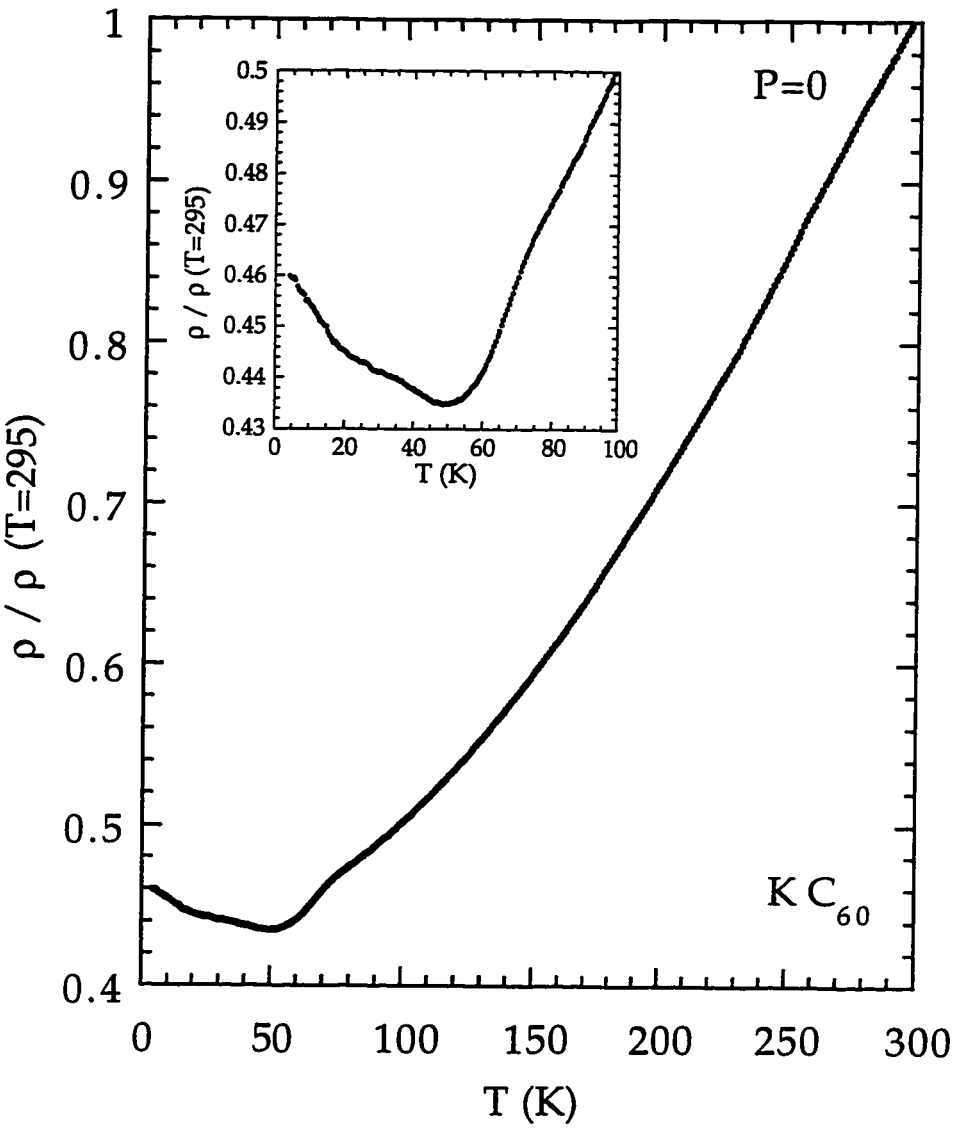

Figure 7.1. The normalized resistivity of polymerized KC_{60} as a function of temperature (measurements were performed by J. Hone[100]). The inset shows the low-temperature behavior. The material shows a transition from a metallic to a semi-metallic phase close to 50 K.

tional form and displays a marked upward curvature, similar to that of the A_3C_{60} materials. The inset to figure 7.1 shows the resistivity of polymerized KC_{60} at low temperatures. Near 50 K, it displays a broad upturn, which may be the sign of a structural and/or electronic phase transition as in the case of the spin density wave (SDW) transition in the low-dimensional organic salt $(TMTSF)_2PF_6$[103]. The low temperature resistivity in polymerized KC_{60} does not follow any activated form as might be expected with the opening of a gap at the Fermi energy. If the transition is indeed due to a SDW (or a charge density wave) then the Fermi surface is most likely only partially gapped. No superconductivity was observed to 1.5 K, nor did the material display any magnetoresistance (within 0.1%) in fields up to 7 T from 4.2 K to 300 K.

The sample was then mounted in a self-clamping pressure cell. Fluorinert FC-75 was used as the pressure medium. About 5 kbar of hydrostatic pressure was locked in at room temperature while monitoring the resistivity of the sample. The pressure cell was then cooled down slowly to 4.2 K while making measurements of the resistivity as a function of temperature. The pressure inside the cell decreases with the temperature due to a larger thermal expansion coefficient of the pressure medium than that of the cell; therefore, the pressure inside the cell was continuously monitored using a calibrated manganin coil. The procedure was repeated for pressures of approximately 6, 8, and 16 kbar.

Figure 7.2 shows the normalized resistivity of polymerized KC_{60} at pressures up to 16.7 kbar, and temperatures from 300 K to 4.2 K. Figure 7.3 shows the low-temperature behavior of the resistivity. Applied pressure greatly reduces the

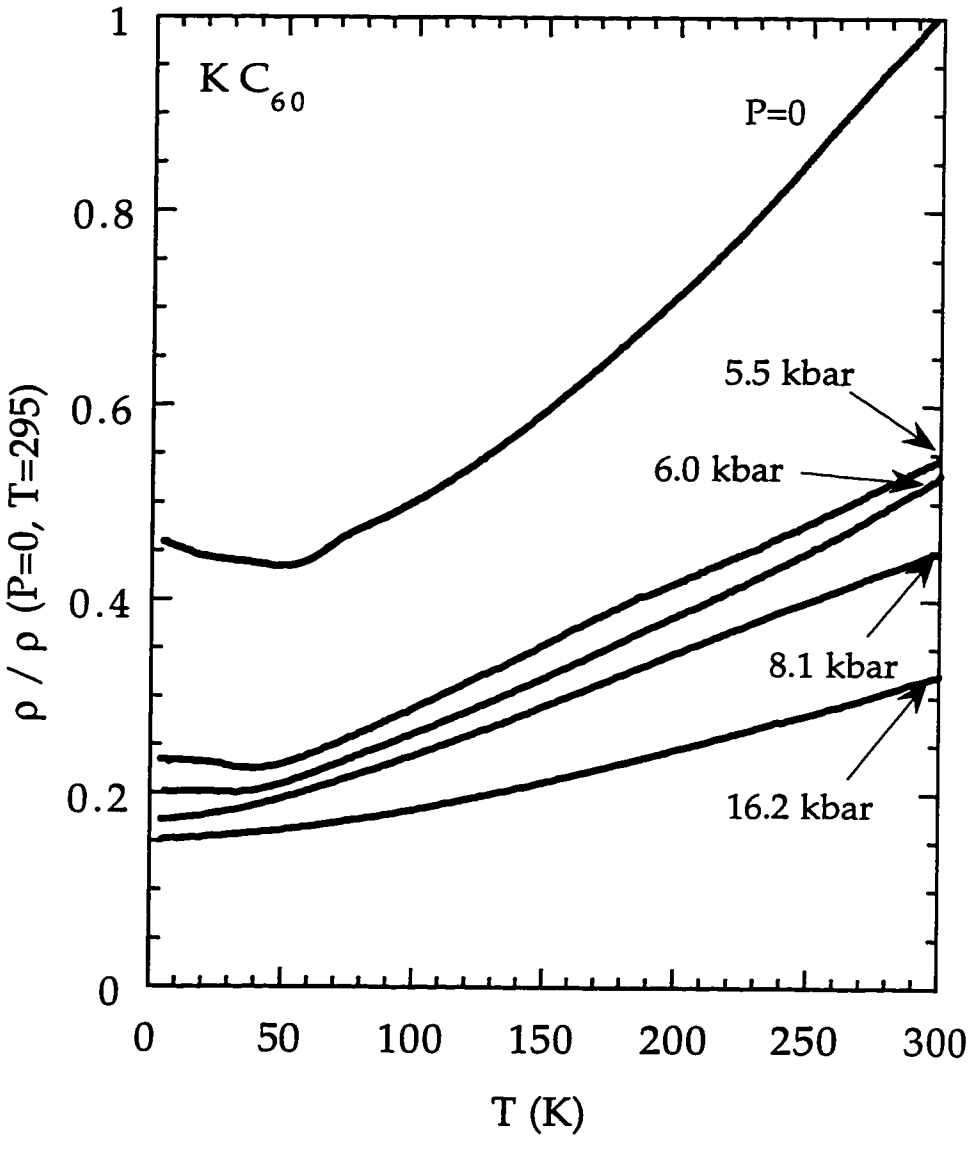

Figure 7.2. The normalized resistivity of KC_{60} as a function of temperature for four different room temperature clamping pressures.

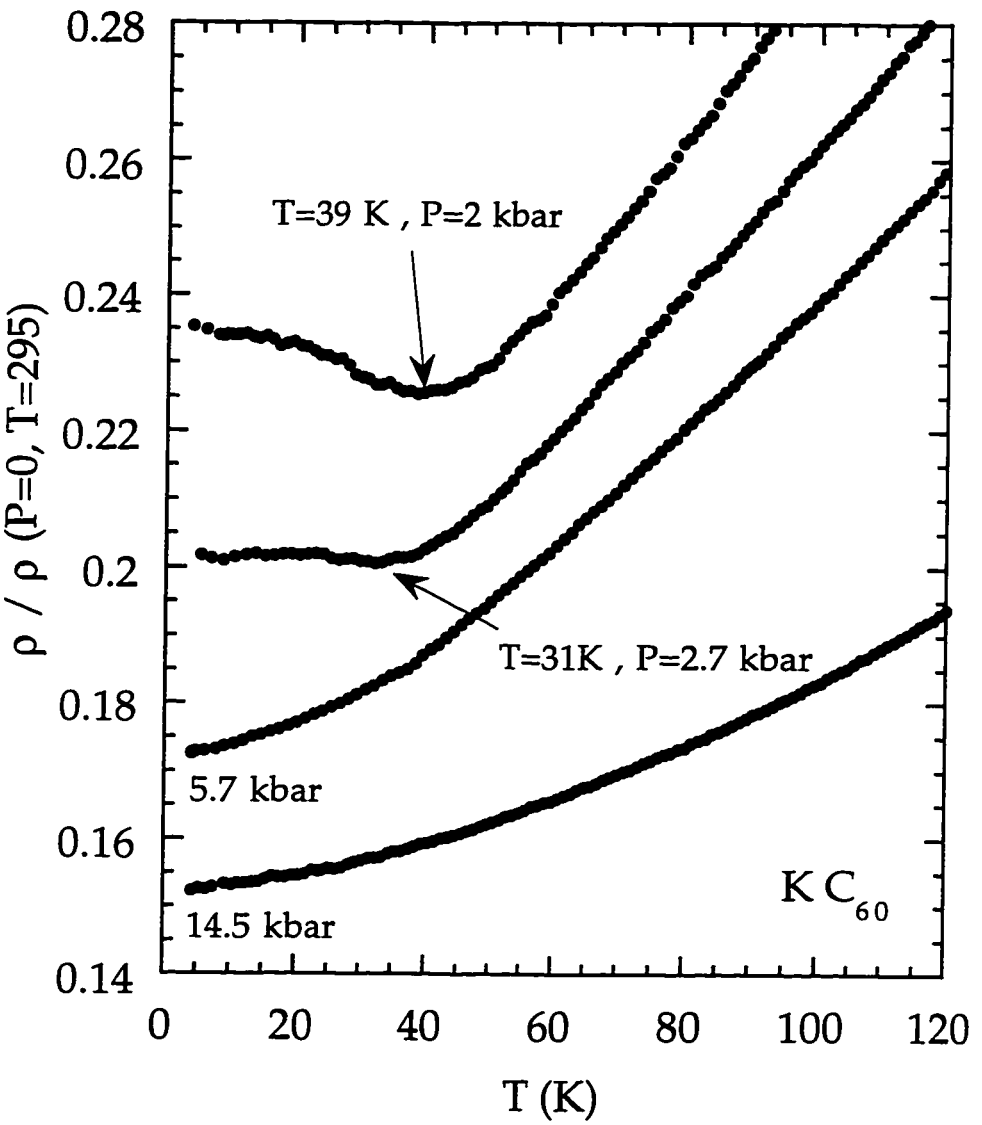

Figure 7.3. The low-temperature resistivity of KC_{60} as a function of temperature for four different room temperature clamping pressures. Notice the suppression of the resistive upturn under pressure.

resistivity, and suppresses the low-temperature transition, as is shown more clearly in the inset. The resistivity minimum shifts downward in temperature, and disappears for applied pressures above ~4 kbar. The suppression of the low-temperature resistive upturn with pressure is consistent with the picture of a transition to a state related to reduced dimensionality: applied pressure increases the dimensionality of the material and suppresses the transition.

7.2 ρ(T, P) of polymerized RbC_{60} at zero and high pressure

The procedure used to make resistivity measurements of RbC_{60} was the same as KC_{60}. Figure 7.4 shows the normalized resistivity of polymerized RbC_{60} as a function of temperature. In contrast to polymerized KC_{60}, this material has a semiconducting-like resistivity, and displays no apparent change in behavior at low temperatures. The upper left inset to Fig. 5 shows log ρ vs. 1/T. At high temperatures, the slope of this plot gives an activation energy of roughly 190 K, although clearly the behavior is not strictly semiconducting.

Once again the sample of RbC_{60} was transferred to a self clamping pressure cell. The pressurization procedure was exactly the same as for KC_{60}. The pressures of approximately 4, 5, 8, and 12 kbar were locked in at room temperature and the cell was cooled down to 4.2 K for resistivity measurements. Figure 7.5 shows the logarithmic resistivity of RbC_{60} as a function of temperature at four different clamping pressures along with the zero pressure data. As pressure is applied and the volume of the polymerized RbC_{60} unit cell is decreased, the mate-

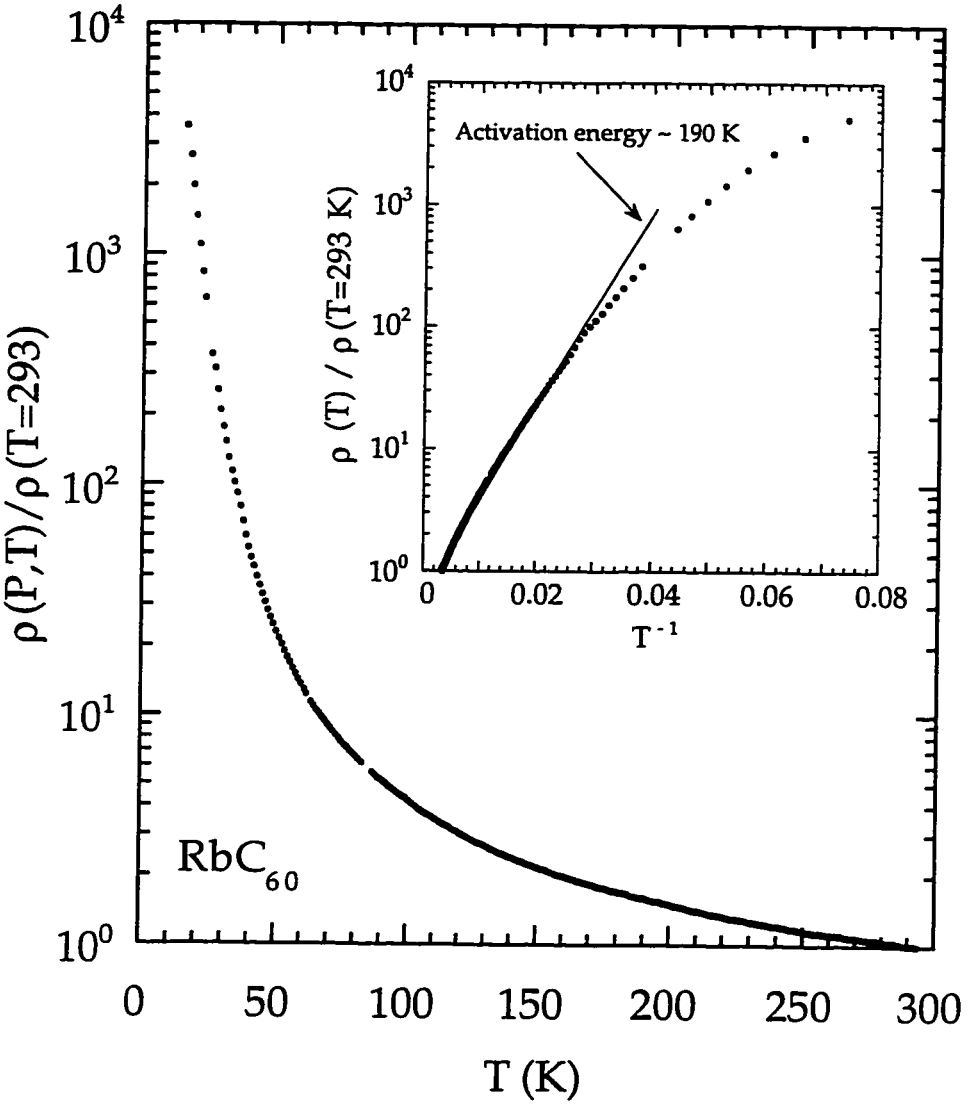

Figure 7.4. The resistivity of RbC_{60} as a function of temperature (measurements were performed by J. Hone). The inset shows the log of resistivity vs. 1/T.

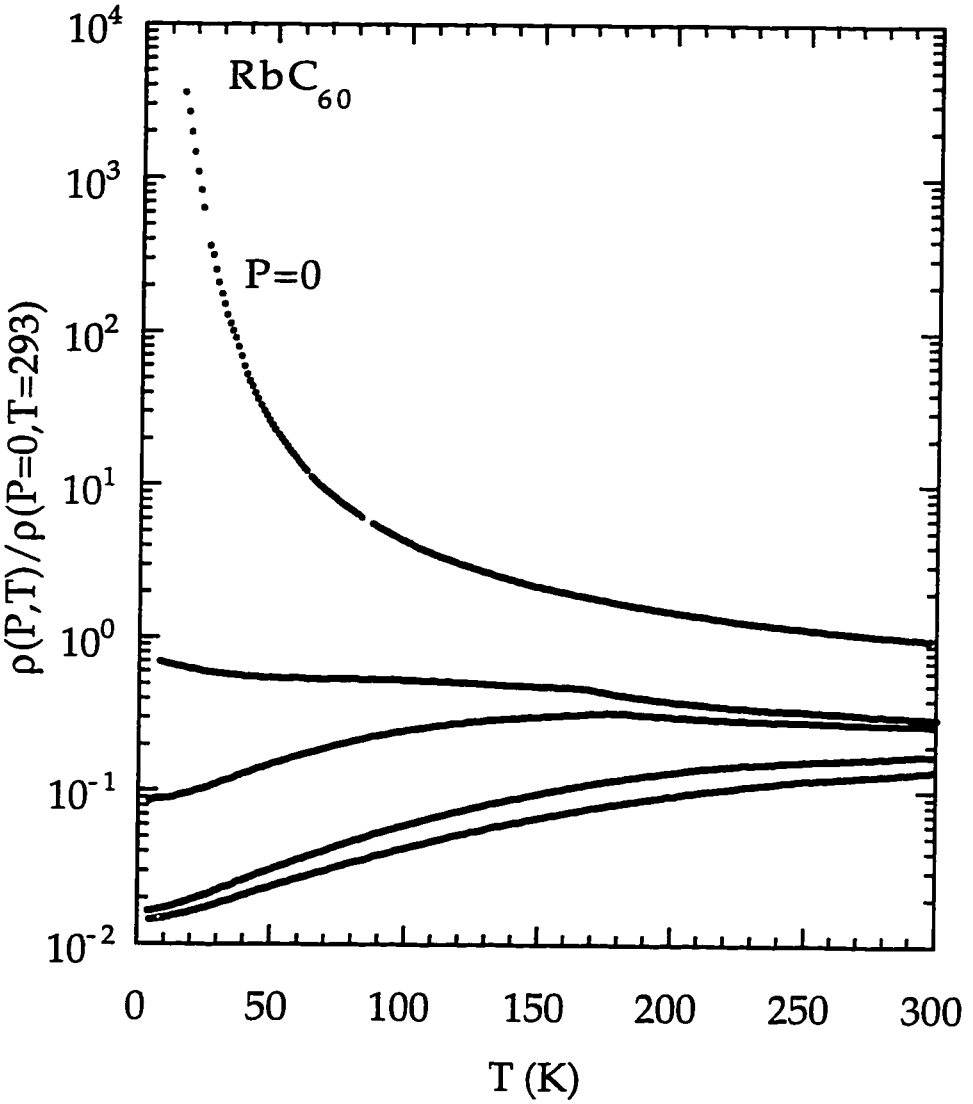

Figure 7.5. The logarithmic resistivity of RbC_{60} as a function of temperature for four different room-temperature clamping pressures of 4.5, 5.2, 8.4, and 10.6 kbar along with the zero pressure data.

rial becomes metallic, behaving similarly to polymerized KC_{60}. In fact, polymerized RbC_{60} is so close to the insulator-metal boundary that the application of 0.5 kbar at 4.2 K is sufficient to reduce the resistivity by over four orders of magnitude. Also significant is that polymerized RbC_{60} does not become metallic gradually, but instead undergoes a sharp transition to the metallic state. This can be seen clearly in figure 7.6. At higher pressures, the transition can be described as to a "better conducting" state since the resistivity is metallic even above the transition temperature. The transition occurs regardless of whether the high- or the low- temperature phase is metallic or semiconducting. It is perhaps the same transition seen at 35 K at zero pressure which has moved up in temperature under pressure, but it has not been observed by any other method.

Figure 7.7 shows this transition in polymerized RbC_{60} at 5 kbar upon cooling and warming. The hysteresis associated with the resistivity around the transition temperature T_{tr}, gives strong evidence that the transition is first-order. This could mean that the material is undergoing a structural phase transition and that one should be able to measure the involved latent heat by calorimetric measurements. Unfortunately, such experiments are difficult to perform since the sample is immersed in a pressure medium inside a large metallic cell. A rough estimate of the latent heat may be obtained from the plot of T_{tr} vs. P (see the inset to figure 7.7) using the Clapeyron equation, $(dP/dT) = \Delta S_{tr}/\Delta V_{tr}$. Assuming the change in volume going from one phase to another is about 1% of the total volume[104], we find L~1mJ/g. This rather small value of L seems reasonable since the high-pressure phase has a smaller volume than the starting phase; hence, the change in vol-

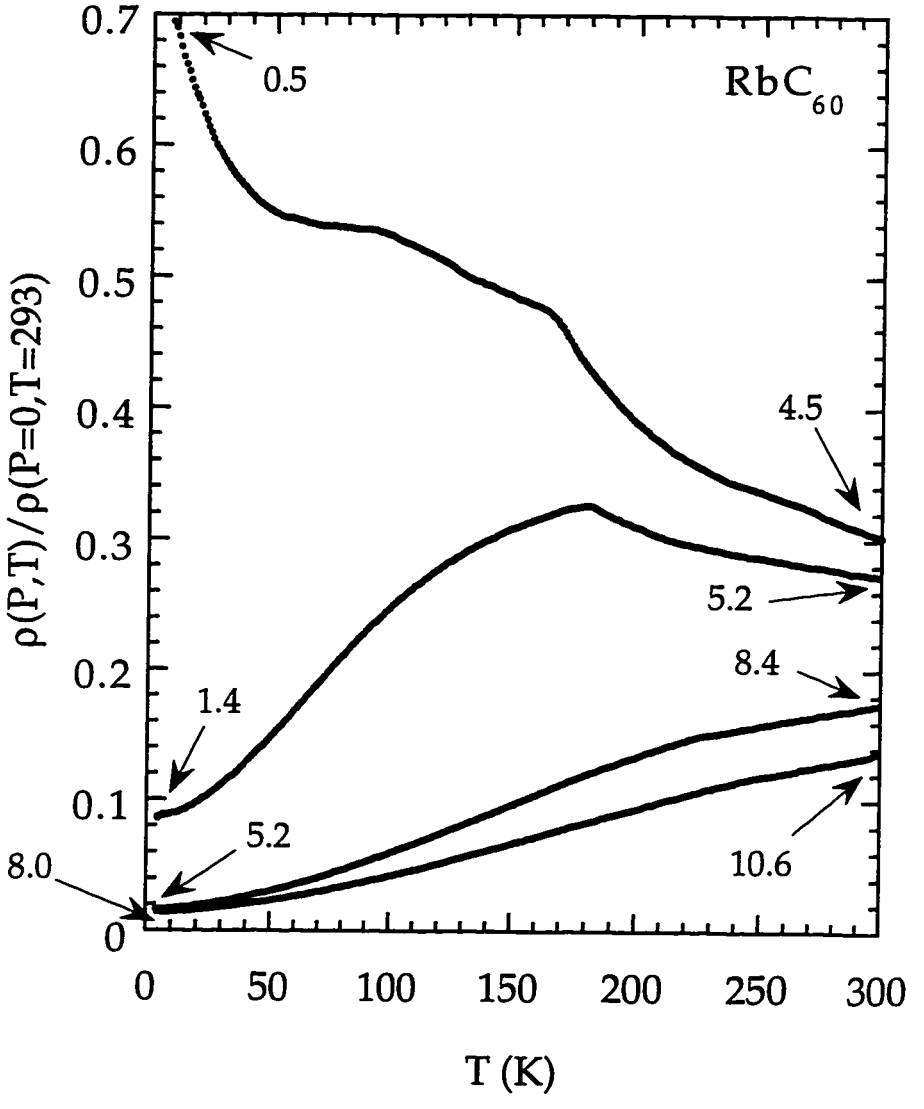

Figure 7.6. The linear scale resistivity of RbC_{60} under pressure as a function of temperature. Notice the sharp transition to the metallic phase. The numbers indicate the pressure in kbars.

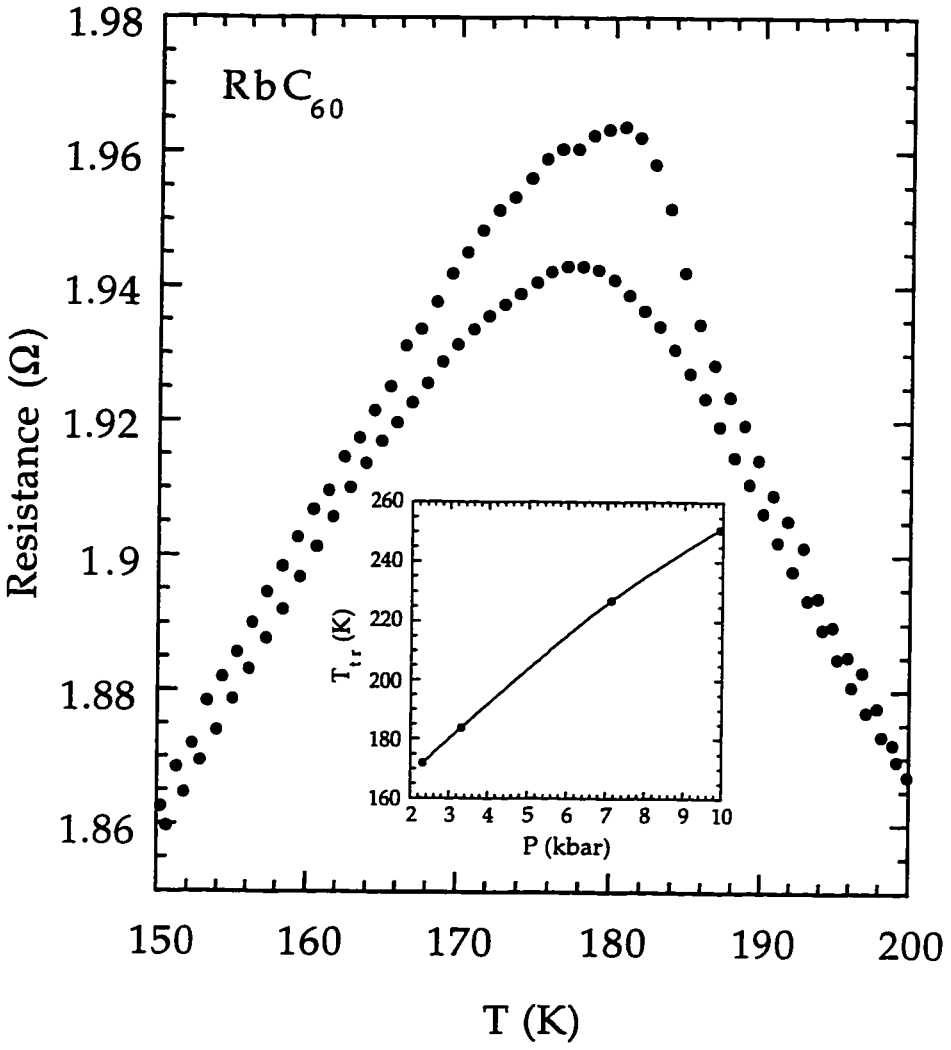

Figure 7.7. Hysteresis associated with the transition in polymerized RbC_{60} under 5.2 kbar of clamping pressure. The inset shows plot of T_{tr} vs. pressure.

ume across the transition dominates the change in entropy[105].

7.3 Universal behavior of resistivity in KC_{60} and RbC_{60}

The resistivity of conductive phases of alkali-doped fullerenes is in general extremely pressure-dependent[102]. As it was shown in section 7.2, the polymerized alkali doped fullerenes are no exception. Figure 7.8 shows the normalized resistivity of RbC_{60} as a function of pressure at different temperatures. It can be seen from this plot that the resistivity is extremely pressure sensitive even at room temperature. A very similar plot is also obtained for KC_{60}. This sensitivity to pressure motivates a correction to constant volume to account for both thermal expansion and the variation in pressure during the temperature sweeps.

In order to correct the measured resistivities for constant volume, the thermal expansion coefficient and the bulk modulus of both KC_{60} and RbC_{60} are needed. Fortunately, the bulk moduli of both materials have been measured: 400 kbar and 580 kbar for KC_{60} and RbC_{60} respectively[106]. The volume thermal expansion coefficient for KC_{60} has also been measured[107]: 3.1×10^{-5} $kbar^{-1}$. The volume thermal expansion of RbC_{60} has not been measured; therefore, in the following calculations, it has been assumed to be equal to that of KC_{60}. It has also been assumed that the bulk moduli of these materials are temperature and pressure independent. The thermal expansion coefficient is taken to be temperature independent down to 30 K, at which temperature it is matched to a T^3 form which smoothly goes down to zero at zero temperature.

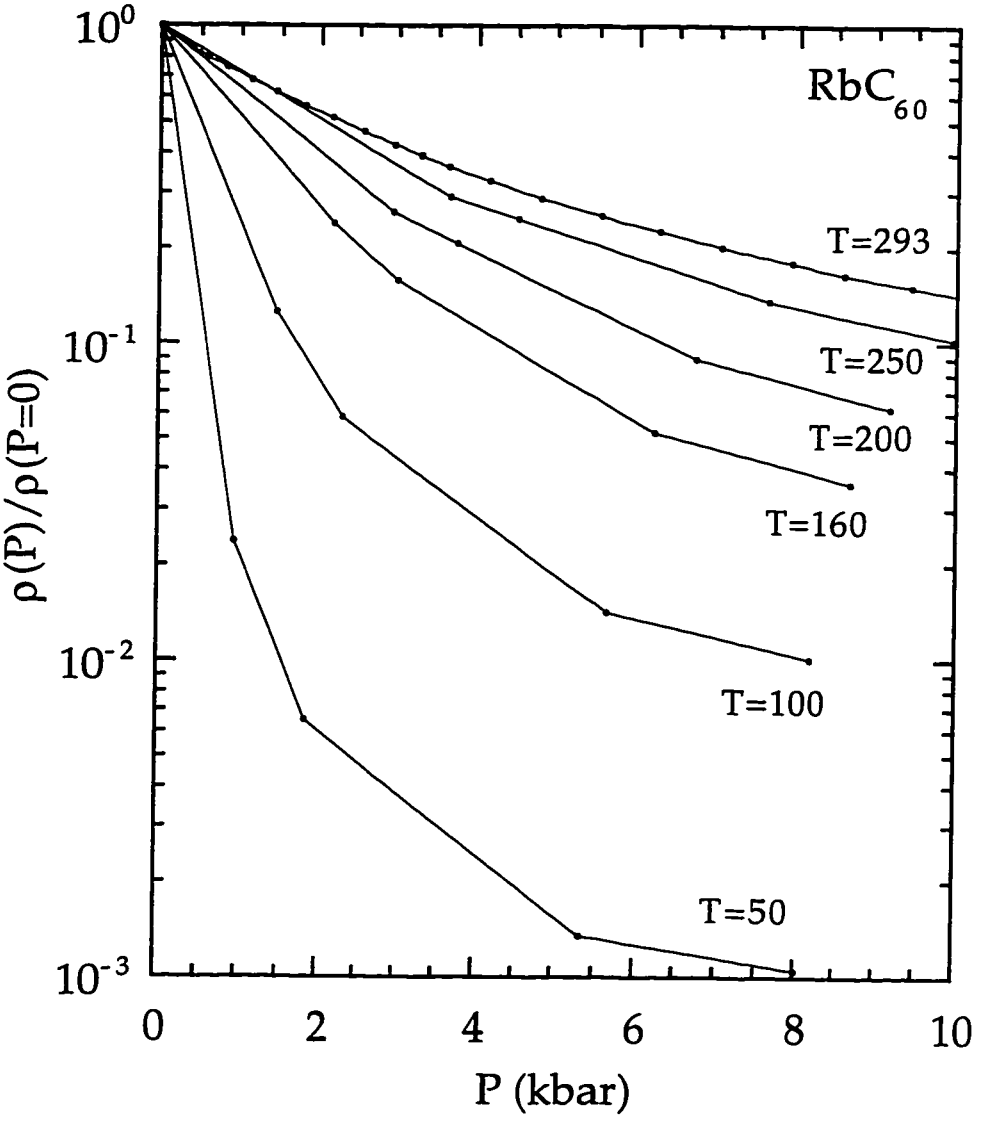

Figure 7.8. The isotherms of the normalized resistivity vs. pressure.

The correction to constant volume is as follows. Warming up the sample from the initial temperature T_i to a final temperature $T_i + \Delta T$ causes the volume to increase by $\Delta \ln V = 3\,\alpha\,\Delta T$, where $3\,\alpha$ is the volume thermal expansion coefficient. To keep the volume constant, a pressure equal to $\Delta P = P = B\,\ln V = 3\,\alpha\,B\,\Delta T$ must be applied, where B is the bulk modulus. The corresponding constant volume resistivity at $T_i + \Delta T$ can be found from the isotherm plots of ρ vs. P using the following equation

$$\rho = \rho((T = T_i + \Delta T), (P = 0))\left[\frac{\rho(P = 3\alpha B \Delta T)}{\rho(P = 0)}\right]_{T_i + \Delta T} \qquad \text{eq. 7.1}$$

where the quantity in the brackets is calculated from the isotherm plots. To calculate the quantity in the brackets from figure 7.8, the five measured points (R, P) were fit to a smoothly varying function which allows interpolation to the pressure required for the maintenance of a constant volume. Many alternative interpolation techniques were tested to insure that the results were not sensitive to any particular fitting functions. This procedure can be repeated for different initial T = 4.2 K volumes by following the same line of reasoning as above. All of the above calculations were programmed on a computer and performed by Dr. Vincent H. Crespi in Professor Marvin L. Cohen's group.

Figure 7.9 shows the results of the constant volume correction for KC_{60}. The correction to constant volume in KC_{60} accentuates the metallic to semimetallic transition. Even though the curves above the P = 0 data are an extrapolation outside the measured resistivities, the results indicate a more pronounced upturn occurring at higher temperatures upon lattice dilation.

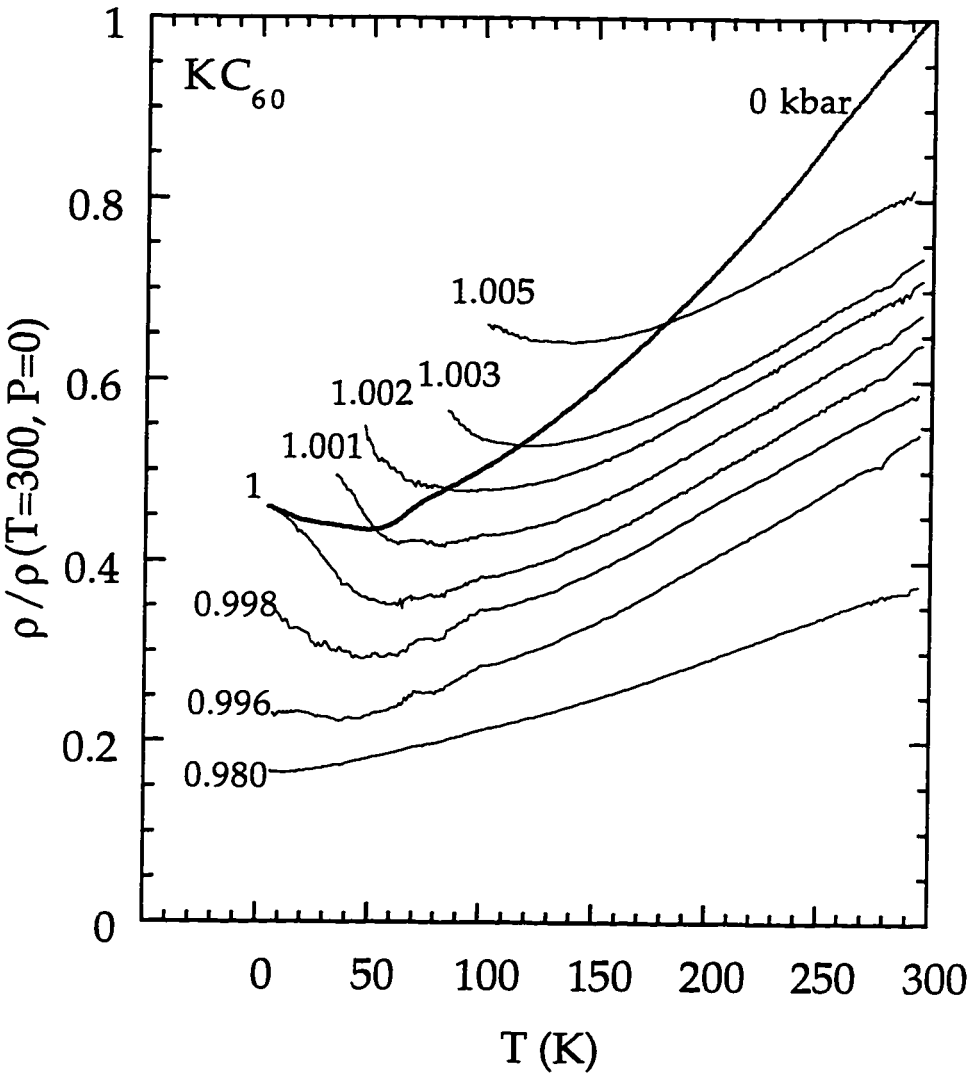

Figure 7.9. The constant volume resistivity of KC_{60} labelled by the fraction of the P = 0 and T = 4.2 K volume occupied at T = 4.2 K (Calculations were performed by Vincent H. Crespi).

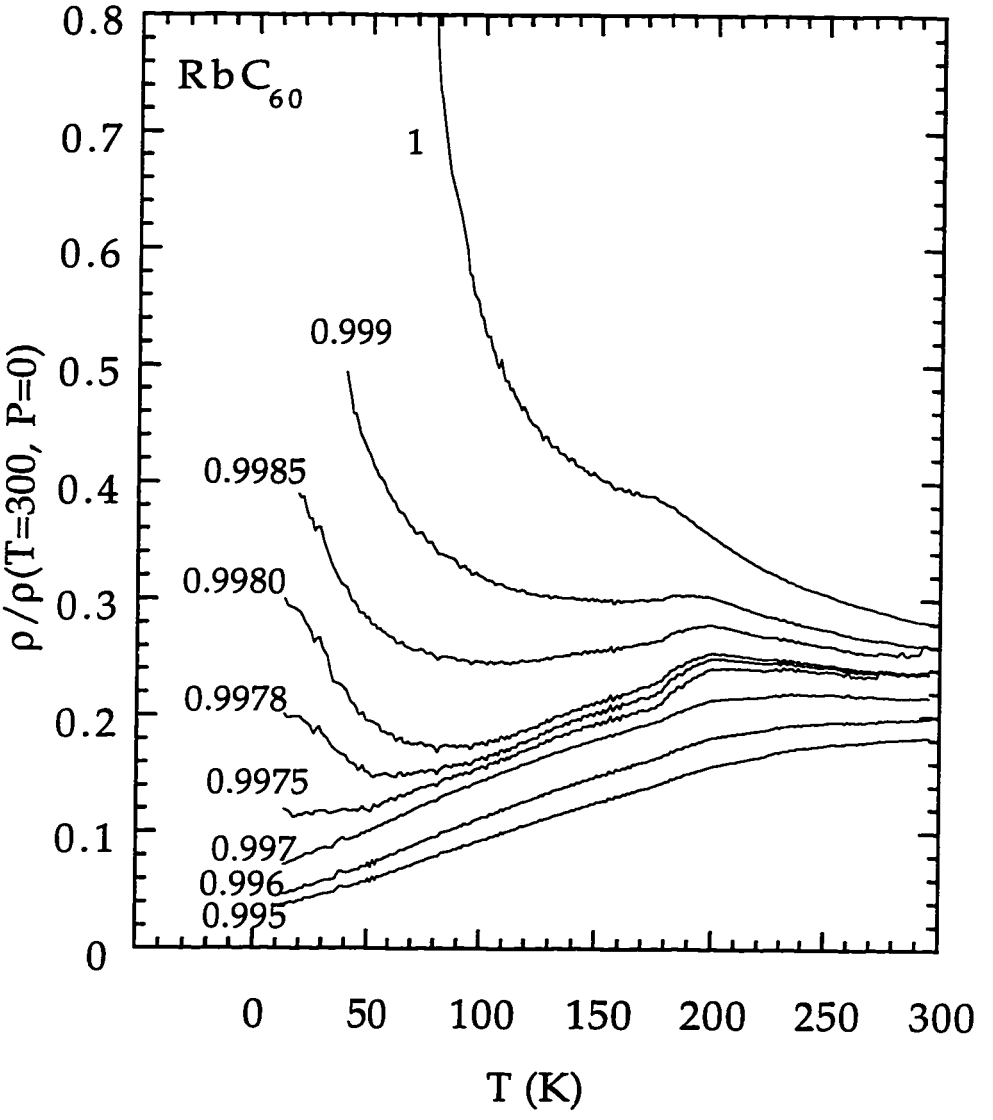

Figure 7.10. The corrected constant volume resistivities of RbC_{60}. The labels are the same as KC_{60} (Calculations were performed by Vincent H. Crespi).

Figure 7.10 shows the same calculation for the polymerized RbC_{60}. At large volumes the transition in RbC_{60} separates two semiconducting phases. Under compression the low-temperature phase becomes metallic until the material becomes completely metallic over the entire temperature range.

The behavior of the resistivity of polymerized RbC_{60} below the transition is very similar to that of polymerized KC_{60}. Figure 7.11 compares the low temperature resistivities of both compounds. At temperatures below ~ 200 K, both materials show metallic character. They both undergo a low temperature resistive upturn which moves up in temperature at larger volumes. The slight difference between the resistivities of the two materials comes from two major sources. First, the interpolation to constant volume introduces uncertainties on the level of the observed differences. Second, the thermal expansion coefficient used for RbC_{60} in these calculations is assumed to be the same as that of KC_{60}. Considering these sources of error, a remarkable "universality" is seen for the resistivities of the polymerized AC_{60} (A=K, Rb) below ~ 200 K.

A complete understanding of these complex materials is yet to be gained. The influence of the domain walls, the dimensionality of the electronic structure, and the character of the bond between the C_{60} molecules all appear to be important in interpreting the electronic transport in these materials. No magnetic transition has been observed in KC_{60} and the "magnetic" transition seen in RbC_{60} is only slightly suppressed under 4 kbar[108]. Therefore the low temperature resistive upturn appears not to be related with a magnetic transition.

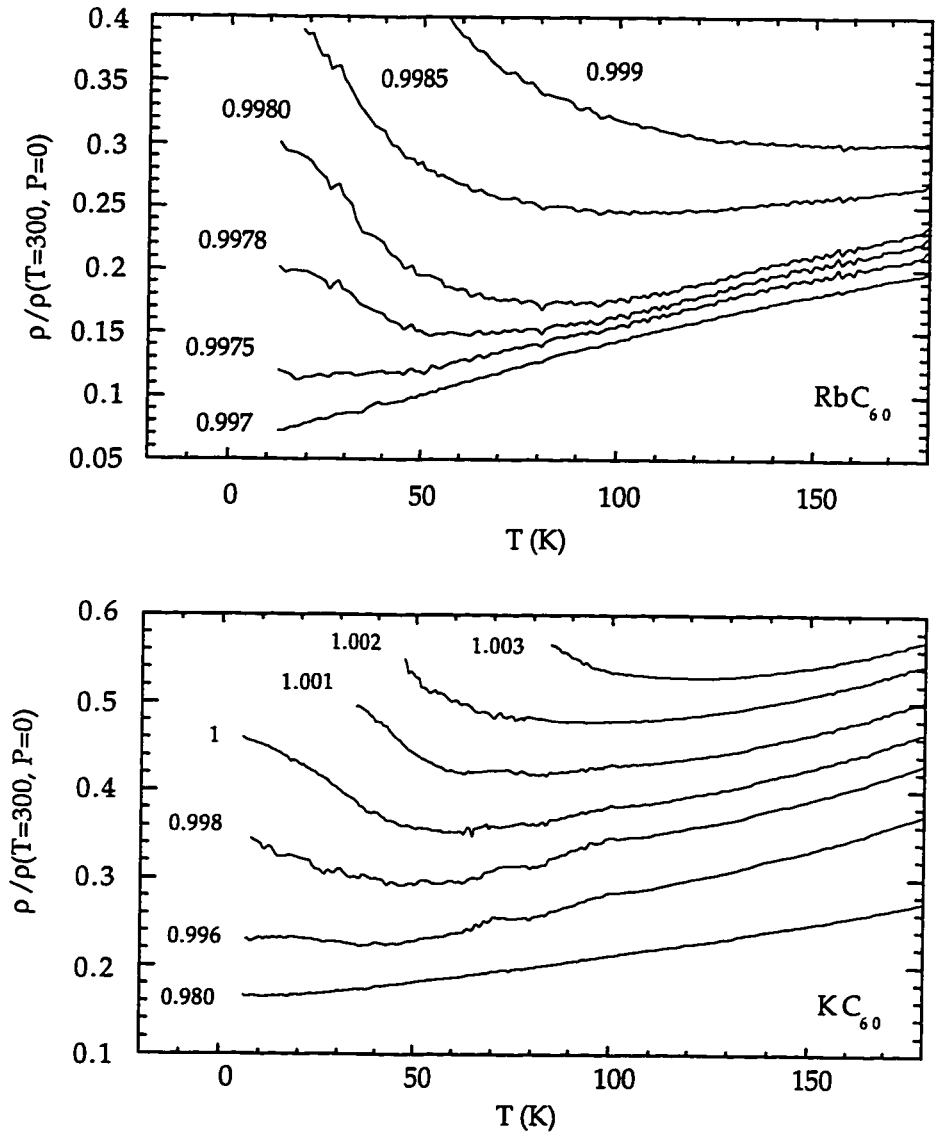

Figure 7.11. Comparison of the low-temperature constant volume resistivities of polymerized RbC_{60} and KC_{60}.

The similarities of the resistivities of polymerized KC_{60} and RbC_{60} below ~200 K suggest that maybe the differences between the character of the bonds connecting two neighboring C_{60} molecules in the two compounds is removed under pressure.

References

1. G. H. Jonker and J. H. Van Santen, Physica XVI, 337 (1950).
2. S. Jin, T. H. Tiefel, M. McCormack, R. A. Fastnacht, R, Ramesh, and L. H. Chen, Science, **264**, 413 (1994).
3. M. Verelst, N. Rangavittal, C. N. R. Rao, and A. Rousset, J. Solid State Chem. **104**, 74 (1993).
4. Y. Tokura, A. Urushibara, Y. Moritomo, T. Arima, A. Atamitsu, G. Kido and N. Furukawa, J. Phys. Soc. Japan, **63**, 3931 (1994).
5. A. Wold and R. J. Arnott, J. Phys. Chem. Solids, **9**, 176 (1959).
6. A. Asamitsu, et al., Nature, **373**, 407 (1995).
7. P. G. Radaelli, D. E. Cox, M. Marezio, S-W. Cheong, P. E. Schiffer, and A. P. Ramirez, Phys. Rev. Lett. **75**, 4488 (1995).
8. V. M. Goldschmidt, Geochemische Verteilungsgesetze der Elemente, VII, VIII, 1927-1928.
9. E. O. Wollan and W. C. Koehler, Phys. Rev. **100**, 545 (1955).
10. P. -G. deGennes, Phys. Rev. **118**, 141 (1960).
11. C. Zener, Phys. Rev. **82**, 403 (1951).
12. A. H. Morrish, B. J. Evans, J. A. Eaton, and L. K. Leung, Canadian Journal of Physics, **47**, 2691 (1969).
13. L. K. Leung, A. H. Morrish, and C. W. Searle, Canadian Journal of Physics, **47**, 2697 (1969).
14. C. W. Searle and S. T. Wang, Canadian Journal of Physics, **47**, 2703 (1969).

15. C. W. Searle and S. T. Wang, Canadian Journal of Physics, **48**, 2023 (1970).

16. M. J. Oretzki and P. Gaunt, Canadian Journal of Physics, **48**, 346 (1970).

17. R. M. Kusters, J. Singleton, D. A. Keen, R. McGreevy, and W. Hayes, Physica B, **155**, 362 (1989).

18. Ken-ichi Chahara, Toshiyuki Ohno, Masahiro Kasai, and Yuzzo Kozono, Appl. Phys. Lett. **63**, 1990 (1993).

19. Y. Morimoto, A. Asamitsu, H. Kuwahara, and Y. Tokura, Nature, **380**, 141 (1996).

20. R. Mahendiran, et al., Phys. Rev. B, **53**, 3348 (1996).

21. Y. X. Jia, Li Lu, K. Khazeni, V. H. Crespi, A. Zettl, and M. L. Cohen, Phys. Rev. B, **52**, 9147 (1995).

22. H. L. Ju, J. Gopalakrishnan, J. L. Peng, Q. Li, G. C. Xiong, T. Venkatesan, and R. L. Greene, Phys. Rev. B, **51**, 6143 (1995).

23. C. Kittel, *Introduction to Solid State Physics*, 6th ed., Wiley, 1986.

24. C. Domb, *Magnetism*, Vol. 2A, Academic Press, 1965.

25. P. Weiss, G. Foex, Arch. Sci. Natl. **31**, 89 (1911).

26. P. Weiss, R. Porrer, Ann. Phys. **5**, 153 (1926).

27. V. Chechersky, A. Nath, H. -L. Ju, and R. L. Greene, submitted to Phys. Rev. Lett.

28. J. J. Neumeier, A. L. Cornelius, and J. S. Schilling, Physica B, **198**, 324 (1994).

29. M. F. Hundley, et al., Appl. Phys. Lett. **67**, 860 (1995).

30. Y. X. Jia, Li Lu, K. Khazeni, D. Yen, C. S. Lee, and A. Zettl, Solid State Comm., **94**, 917 (1995).

31. K. Khazeni, Y. X. Jia, V. H. Crespi, A. Zettl, and M. L. Cohen, J. Phys.: Condens. Matter, **8**, 7723 (1996).

32. V. H. Crespi, Li Lu, Y. X. Jia, K. Khazeni, A. Zettl, and M. L. Cohen, Phys. Rev. B, **53**, 14303 (1996).

33. J. M. D. Coey, M. Viret, L. Ranno, and K. Ounadjela, Phys. Rev. Lett. **75**, 3910 (1995).

34. N. F. Mott and E. A. Davis, *Electronic Processes in Non-crystalline Materials* , Clarendon, Oxford, 1979.

35. P. Schiffer, A. P. Ramirez, W. Bao, and S. W. Cheong, Phys. Rev. Lett. **75**, 3336 (1995).

36. E. E. Fullerton, M. J. Conover, J. E. Mattson, C. H. Sowers, and S. D. Bader, Appl. Phys. Lett. **63**, 1699 (1993).

37. M. N. Baibich, J. M. Broto, A. Fert, F. Nguyen Van dau, and F. Petroff, Phys. Rev. Lett. **61**, 2472 (1988).

38. S. S. Parkin, N. More, and K. P. Roche, Phys. Rev. Lett. **64**, 2304 (1990).

39. G.C. Xiong, Q. Li, H. L. Ju, S. N. Mao, L. Senapati, X. X. Xi, R. L. Greene, and T. Venkatesen, Appl. Phys. Lett. **66**, 1427 (1995); J. M. De Teresa, et al., in preceedings of the CMR workshop, Los Alamos NM, 8-9 January, 1995; J. Zhang, et al. in ibid; J. Z. Liu, in ibid; R. von Helmolt, et al., Phys. Rev. Lett. **71**, 2331 (1995).

40. L. Orgel, *Introduction to transition metal chemistry*, 2nd ed., Wiley, 1966.

41. S. Satpathy, Zoran S. Popovic, and Filip R. Vukajiovic, Phys. Rev. Lett. **76**, 960 (1996).

42. J. Matsumoto, J. Phys. Soc. Japan, **29**, 615 (1970).

43. A. J. Millis, Boris I. Shraiman, and R. Mueller, Phys. Rev. Lett. **77**, 175 (1996).

44. Q. Williams and R. Jeanloz, Phys. Rev. Lett. **56**, 163 (1986).

45. David Erskine, Peter Y. Yu, K. J. Chang, and Marvin L. Cohen, Phys. Rev. Lett. **57**, 2741 (1986).

46. Q. Williams and R. Jeanloz, *Ultra-High-Pressure Experimental Techniques*, Molten Salt Techniques, Vol. 4 (1991).

47. L. Merrill and W. A. Bassett, Rev. Sci. Instrum. **45**, 290 (1974).

48. H. K. Mao and P. M. Bell, K. J. Dunn, R. M. Chrenko, and R. C. DeVries, Rev. Sci. Instrum. 50, 1002 (1979).

49. I. Parker, *Pressure cell manual* (Zettl group, 1990).

50. A. Jayaraman, A. R. Huston, J. H. McFee, A. S. Coriell and R. G. Maines, Rev. Sci. Instrum. **38**, 44 (1967).

51. J. D. Thompson, Rev. Sci. Instrum. **55**, 231 (1984).

52. D. R. P. Guy and R. H. Friend, J. Phys. E. **19**, 430 (1986).

53. A. Jayaraman, Rev. Mod. Phys., **55**, 65 (1983).

54. S. Jin, et al. Appl. Phys. Lett. **66**, 382 (1995).

55. A/B site vacancies can be associated with self-doping; S. S. Manoharan, et al., J. Solid State Chem. **117**, 420 (1995).

56. K. Khazeni, X. Y. Jia, Li Lu, V. H. Crespi, A. Zettl, and M. L. Cohen, Phys. Rev. Lett. **76**, 295 (1996).

57. Y. Morimoto, A. Asamitsu, Y. Tokura, Phys. Rev. B, **51**, 16491 (1995).

58. A. J. Millis, P. B. Littlewood, and B. I. Shraiman, Phys. Rev. Lett. **74**, 5144 (1995).

59. W. E. Pickett and D. J. Singh, Phys. Rev. B, **53**, 1146 (1996).

60. G. C. Xiong, et al., Appl. Phys. Lett. 66, 1427 (1995) figure 1, A. J. Millis, et al., Phys. Rev. Lett. 74, 5144 (1995) figure 1, H. Y. Hwang, et al., Phys. Rev. Lett. 75, 914 (1995) y=0.35 figure 1, Y. X. Jia, V. H. Crespi, K. Khazeni, L. Lu, and A. Zettl, (1995) unpublished, M. F. Hundley (19950 personal communication.

61. T. G. Dietz, M. A. Duncan, D. E. Powers, and R. E. Smalley, J. Chem. Phys. **74**, 6511 (1981).

62. H. W. Kroto, J. R. Heath, S. C. O'Brien, R. F. Curl, and R. E. Smalley, Nature **318**, 162 (1985).

63. Ph. Gerhardt, S. Loeffler, and K. Homann, Chem. Phys. Lett. **137**, 306 (1987).

64. W. Kratschmer, K. Fostiropoulos, D. R. Huffman, Chem. Phys. Lett. **170**, 167 (1990).

65. A. F. Hebard, M. J. Rosseinsky, R. C. Haddon, D. W. Murphy, S. H. Glarum, T. T. M. Palstra, A. P. Ramirez, and A. R. Kortan, Nature **350**, 600 (1991).

66. R. Tycko, G. Dabbagh, R. M. Fleming, R. C. Haddon, A. V. Makhija, and S. M. Zahurak, Phys. Rev. Lett. **67**, 1886 (1991).

67. W. I. F. David, R. M. Ibberson, J. C. Mathewman, K. Prassides, T. S. Dennis, J. P. Hare, H. W. Kroto, R. Taylor, and D. R. M. Walton, Nature, **353**, 147 (1991).

68. P. A. Heiney, G. B. M. Vaughan, J. E. Fischer, N. Coustel, D. E. Cox, J. R. D. Copley, D. A. Neumann, W. A. Kamitakahara, K. M. Kreegan, D. M. Cox, J. P. McCauley, and A. B. Smith III, Phys. Rev. B, **45**, 4544 (1992).

69. H. Kuzmany et al. *Electronic Proerties of Fullerenes*, **141** (1993).

70. W. I. F. David, R. M. Ibberson, T. J. S. Dennis, J. P. Hare, and K. Prassides, Euro-

phys. Lett. **18**, 219 (1992).

71. W. Edward Billups and Marco A. Ciufolini, *Buckminsterfullerenes*, VCH, p. 219, (1993).

72. W. Edward Billups and Marco A. Ciufolini, *Buckminsterfullerenes*, VCH, p. 233, (1993).

73. S. Pekker, A. Janossy, L. Mihaly, O. Chauvet, M. Carrard, and L. Forro, Science, **265**, 1077 (1994).

74. D. Koller, M. C. Martin, P. W. Stephens, L. Mihaly, S. Pekker, A. Janossy, O. Chauvet, and L. Forro, Applied Physics Letters, **66**, 1015 (1995).

75. N. G. Chopra, J. Hone, A. Zettl, Phys. Rev. B, **53**, 8155 (1996).

76. J. Winter and H. Kuzmany, Solid State Comm. **84**, 935 (1992).

77. O. Chauvet, et al., Phys. Rev. Lett. **72**, 2721 (1994).

78. P. W. Stephens, et al., Nature, **370**, 636 (1994).

79. H. Alloul, V. Brouet, E. Lafontaine, L. Malier, and L. Forro, Phys. Rev. Lett. **76**, 2922 (1996).

80. V. Brouet, Y. Yoshinari, H. Alloul, and L. Forro, Physica C, **235-240**, 2481 (1994).

81. V. Brouet, H. Alloul, Y. Yoshinari, and L. Forro, Phys. Rev. Lett. **76**, 3638 (1996).

82. C. Goze, F. Rachdi, M. Apostol, J. E. Fischer, and M. Mehring, *NMR studies of alkali fullerides:* Rb_1C_{60} *and* Cs_1C_{60} 1-115-17 (Strasbourg, France, 1995).

83. T. Kalber, G. Zimmer, and M. Mehring, Phys. Rev. B, **51**, 16471 (1995).

84. K. -F. Thier, G. Zimmer, M. Mehring, and F. Rachdi, Phys. Rev. B, **53**, R496 (1996).

85. J. Robert, P. Petit, and J. E. Fischer, *Phase instabilities in* KC_{60} 1-119-21 (Stras-

bourg, France, 1995).

86. J. Robert, P. Petit, J. -J. Andre, and J. E. Fischer, Solid State Comm. **96**, 143 (1995).

87. J. Robert, P. Petit, and J. E. Fischer, Physica C, **262**, 27 (1996).

88. Y. J. Uemura, et al., Phys. Rev. B, **52**, R6991 (1995).

89. W. A. MacFarlane, R. F. Kiefl, S. Dunsiger, J. E. Sonier, and J. E. Fischer, Phys. Rev. B, 52, R6995 (1995).

90. L. Cristofolini, et al., Journal of Physics: Condensed Matter 7, L567 (1995).

91. K. Kamaras, L. Granasay, D. B. Tanner, and L. Forro, Phys. Rev. B, **52**, 11488 (1995).

92. F. Bommeli, L. Degiorgi, P. Wachter, and L. Forro, *Optical Properties of the A_1C_{60} (A=K, Rb and Cs) Linear Polymer Fullerides* 1-111-14 (Strasbourg, France, 1995).

93. K. Kamaras, et al., *Optical Spectroscopy on Monomeric and Polymeric 1:1 Fulleride Salta* 1-621-2 (Coral Gables, FL, USA, 1995).

94. F. Bommeli, et al., Phys. Rev. B, **51**, 14794 (1995).

95. M. C. Martin, D. Koller, A. Rosenberg, C. Kendziro, and L. Mihaly, Phys. Rev. B, **51**, 3210 (1995).

96. M. C. Martin, D. Koller,X. Du, P. W. Stephens, and L. Mihaly, Phys. Rev. B, **49**, 10818 (1994).

97. J. Winter and H. Kuzmany, Journal of Raman Spectroscopy, **27**, 378 (1996).

98. J. Winter and H. Kuzmany, Phys. Rev. B, 52, 7115 (1995).

99. G. P. Lopinski, M. G. Mitch, J. R. Fort, and J. S. Lannin, Phys. Rev. B, **50**, 16098 (1994).

100.J. Hone, M. S. Fuhrer, K. Khazeni, and A. Zettl, Phys. Rev. B, **52**, R8700 (1995).

101.S. C. Erwin, G. V. Krishna, and E. J. Mele, Phys. Rev. B, **51**, 7345 (1995).

102.W. A. Vareka and A. Zettl, Phys. Rev. Lett. **72**, 4121 (1994).

103.P. M. Chaikin, G. Gruner, E. M. Engler, and R. L. Greene, Phys. Rev. Lett. **45**, 1874 (1980).

104.The 1 % change in volume is motivated by the fact that polymerized KC_{60} is metallic and polymerized RbC_{60} is semi-conducting at zero pressure, and that their unit-cell volumes differ by about 1 %.

105.R. Jeanloz, private communication.

106.J. Nguyen, J. Hone, R. Jeanloz, and A. Zettl, unpublished.

107.G. Oszlanyi, G. Bortel, G. Faigel, M. Tegze, P. W. Stephens, and L. Forro, *Physics and Chemistry of Fullerenes and Derivatives*, Proceedings of the International Winterschool on Electronic Properties of Novel Materials, eds. H. Kuzmany, Jorg Fink, Michael Mehring, and Siegmar Roth (World Scientific, 1995) 323.

108.L. Forro, et al., *Physics and Chemistry of Fullerenes and Derivatives*, Proceedings of the International Winterschool on Electronic Properties of Novel Materials, eds. H. Kuzmany, Jorg Fink, Michael Mehring, and Siegmar Roth (World Scientific, 1996) 102.